

The Space Weather of Ultracool Dwarfs

by

Anna Hughes

B.Sc., Rensselaer Polytechnic Institute, 2012

M.Sc., University of British Columbia, 2016

A THESIS SUBMITTED IN PARTIAL FULFILLMENT
OF THE REQUIREMENTS FOR THE DEGREE OF

Doctor of Philosophy

in

THE FACULTY OF GRADUATE AND POSTDOCTORAL STUDIES

(Astronomy)

The University of British Columbia

(Vancouver)

May 2021

© Anna Hughes, 2021

The following individuals certify that they have read, and recommend to the Faculty of Graduate and Postdoctoral Studies for acceptance, the dissertation entitled:

The Space Weather of Ultracool Dwarfs

submitted by Anna Hughes in partial fulfillment for the requirements for
the degree of Doctor of Philosophy
in Astronomy

Examining Committee:

Aaron Boley, Physics and Astronomy, UBC
Supervisor

Jeremy Heyl, Physics and Astronomy, UBC
Supervisory Committee Member

Jess McIver, Physics and Astronomy, UBC
University Examiner

Sun Kwok, Earth, Ocean and Atmospheric Sciences, UBC
University Examiner

Additional Supervisory Committee Members:

Paul Hickson, Physics and Astronomy, UBC
Supervisory Committee Member

Katherine Johnson, Earth, Ocean and Atmospheric Sciences, UBC
Supervisory Committee Member

Abstract

Empirical trends in stellar X-ray and radio luminosities suggest that very low mass stars and brown dwarfs should not produce significant radio emission. Defying these expectations, strong non-thermal emission has been observed in some UCDs in the 1–10 GHz range, often attributed to global aurorae. At higher radio frequencies, flux due to global aurorae becomes unphysical, and is instead attributed to gyrosynchrotron radiation. In my Ph.D. work I used observations in this frequency range (30–100 GHz) to infer the presence of gyrosynchrotron radiation from ultracool dwarfs in three stars, and to place upper limits on the radio flux on three other stars that were not detected. Prior to this work, only one ultracool dwarf had been detected at such high radio frequencies. My results suggest that gyrosynchrotron radiation from radio-loud ultracool dwarfs might be more common than previously assumed. Another key component of my thesis has been an extensive radio study of the ultracool dwarf TRAPPIST-1. The TRAPPIST-1 system is notable for its seven terrestrial planets, at least three of which orbit within the habitable zone. I put upper limits on the quiescent radio emission from the star at 44 and 97.5 GHz using the VLA and ALMA, and monitored the long-term 2 GHz emission from the star over 50 hours to search for variability. I used these results to constrain the possible gyrosynchrotron radiation from the star, as well as the resulting space weather impacts on surrounding planets. My results from the TRAPPIST-1 studies suggest that the TRAPPIST-1 planets are not regularly exposed to high populations of energetic particles due to stellar activity, supporting the case for planetary habitability.

Lay Summary

The smallest stars and sub-stellar objects are referred to as ultracool dwarfs (UCDs). UCDs are relatively common, but are difficult to detect at radio frequencies. Observational trends and their internal structure suggest UCDs should have low magnetic activity and no detectable radio emission. However, radio observations reveal that $\sim 10\%$ are radio-loud, with brighter emission than expected. There are two primary explanations for the radio brightness: aurorae similar to those seen on Solar System planets, or eruptive magnetic events. These two explanations can be distinguished by observations at high radio frequencies, for which only emission from magnetic events is detectable. Prior to my work, only one UCD had been detected at these high frequencies. I have quadrupled that number, as well as placed limits on the magnetic activity possible from radio quiet UCDs. I then investigated the potential impacts of radio-emitting magnetic events on the stability of planetary atmospheres.

Preface

Chapters 1. Figures 1.1, 1.3, 1.10, 1.12, are used with permission from applicable sources.

Chapter 3 is based on an *Astrophysical Journal* publication (Hughes et al., 2021). It uses ALMA and VLA observations of five ultracool dwarfs to measure the strength of radio emission or place upper limits in the case of a non-detection. Co-authors on this paper include Aaron Boley, Rachel Osten, Jacob White, and Marley Leacock. Jacob White aided in the data reduction and analysis, and Rachel Osten aided in the scientific interpretation of the results. All co-authors assisted in providing feedback on the manuscript.

Chapter 4 is based on a *Monthly Notices of the Royal Astronomical Society* publication (Hughes et al., 2019). It uses ALMA and VLA observations of TRAPPIST-1 to measure the strength of radio emission or place upper limits in the case of a non-detection. Co-authors on this paper include Aaron Boley, Rachel Osten, and Jacob White. Jacob White aided in the data reduction and analysis, and Rachel Osten aided in the scientific interpretation. All co-authors assisted in providing feedback on the manuscript. Chapter 4 also makes use of VLA observations of TRAPPIST-1 to monitor the star for evidence of variability, currently in prep. for publication.

Chapters 5. Figure 5.2 is used with permission from the applicable source.

This body of work was identified, designed, and carried out by Anna Hughes.

Table of Contents

Abstract	iii
Lay Summary	iv
Preface	v
Table of Contents	vi
List of Tables	ix
List of Figures	xi
List of Symbols	xx
List of Abbreviations	xxi
Dedication	xxiii
1 Introduction to Ultracool Dwarfs	1
1.1 M Dwarfs	1
1.2 Brown Dwarfs	6
1.3 Magnetic Dynamos	9
1.3.1 The $\alpha\Omega$ Dynamo	9
1.3.2 Mean-Field Magnetohydrodynamics	13
1.3.3 The α^2 Dynamo	14
1.4 Radio Observations of UCDs	17

1.5	Radio Emission from Stars	21
1.5.1	Definitions, Units, and Radiative Transfer	22
1.5.2	Bremsstrahlung Emission	26
1.5.3	Plasma Emission	27
1.5.4	The Electron Cyclotron Maser Instability	30
1.5.5	Synchrotron Radiation	36
1.5.6	Gyrosynchrotron Radiation	38
2	Radio Astronomy	43
2.1	Radio Telescopes	43
2.2	Interferometry	45
2.2.1	The Karl G. Jansky Very Large Array	49
2.2.2	The Atacama Large Millimetre Array	51
2.2.3	The Fourier Transform	51
2.2.4	Imaging in Interferometry	54
3	Ultracool Dwarf Radio Emission	57
3.1	Introduction	57
3.2	Observations and Results	59
3.2.1	LP 349-25	60
3.2.2	LSR J1835+3259	62
3.2.3	NLTT 33370	63
3.2.4	LP 415-20AB	65
3.3	Discussion	67
3.4	Summary	73
4	TRAPPIST-1	74
4.1	Background	74
4.2	Introduction	76
4.3	Observations	77
4.3.1	ALMA Observations	78
4.3.2	VLA Observations	79
4.3.3	Null detections of TRAPPIST-1	80
4.4	TRAPPIST-1 in the Context of UCD Radio Emission	80

4.5	Monitoring Campaign of TRAPPIST-1	85
4.5.1	Observations	86
4.6	Summary	88
5	Ultracool Dwarf Magnetism and Habitability	91
5.1	The Habitable Zone	92
5.2	Particle Flux in Context	94
5.3	Estimating the Particle Flux	98
5.3.1	Scaling the Proton Flux	98
5.3.2	Proton Flux from Solar Particle Events	99
5.3.3	Proton Flux from Solar Radio Bursts	101
5.4	Implications for Planets in Radio Loud UCD Systems	105
5.5	Summary	106
6	Summary and Future Work	107
6.1	Summary	108
6.2	Future Work	110
6.2.1	TRAPPIST-1 Monitoring Campaign	111
6.2.2	Upcoming VLA Surveys	112
6.2.3	Archival Data	112
6.2.4	Investigating the impact on planetary habitability	113
6.2.5	Correlating Observations Across Wavelengths	113
	Bibliography	117

List of Tables

Table 1.1	Properties of M dwarfs by spectral sub-class.	7
Table 1.2	Properties of brown dwarfs by spectral type.	8
Table 3.1	Properties of ultracool dwarfs presented in this work, including combined spectral type, total mass (M_{tot}), stellar distance, stellar age, effective temperature (T_{eff}), and $v \sin i$, frequency of the observations ν (GHz), and observed flux (μJy). References: (1) Gizis et al. (2000) (2) Konopacky et al. (2010) (3) Schmidt et al. (2007) (4) Konopacky et al. (2012) (5) Reid et al. (2003) (6) Berdyugina et al. (2017) (7) Lépine et al. (2009) (8) Schlieder et al. (2014) (9) McLean et al. (2011) (10) Siegler et al. (2003) (11) Reiners and Basri (2010) (12) Cruz et al. (2003).	60
Table 4.1	Stellar Parameters of TRAPPIST-1 taken from the literature. . .	75
Table 4.2	3σ upper flux and radio luminosity limits on TRAPPIST-1. The 6 GHz observations are from Pineda and Hallinan (2018). . . .	78
Table 5.1	Properties of UCDs included in the survey, all presented in Chapter 3, that are used in the energetic particle flux estimates.	93
Table 5.2	The locations of the habitable zone as determined from the equilibrium temperature around each UCD presented in Chapter 2. The average values, bolded in column 2, are used for the primary particle flux estimates. The inner a_{in} and outer a_{out} ends of the habitable zone are used to calculate the extremes of particle flux values.	95

Table 5.3	Estimates of proton fluxes received at UCD-orbiting planets if quasi-quiet UCD emission is equivalent to energetic protons released during Solar particle events.	100
Table 5.4	The 5, 9 and 15 GHz emission measured by the Radio Solar Telescope Network along with the maximum energetic (> 10 MeV) particle flux measured by the GOES satellite from the SPEs that accompanied all 6 of the observed flares. [1] Joshi et al. (2013) [2] Belov et al. (2015) [3] Neal et al. (2013) [4] Paasilta et al. (2017).	102
Table 5.5	Radio luminosities, proton luminosities, and ratios of the two for all Solar flares in this section. The radio luminosities of the events detailed in Table 5.4 were found by averaging all maximum flux values for each event. Note that the units of L_R and L_{p^+} are not the same, so the ratio in the last column is not unitless.	103
Table 5.6	Proton fluxes received at the inner and outer edges of the habitable zone for the detected UCDs and at TRAPPIST-1e and g following Equation 5.11. The distances and fluxes of each UCD are rounded to the nearest integer for these calculations. These estimates include values for both the quiescent and flaring flux of NLTT 33370 and the VLA and ALMA limits on TRAPPIST-1, as well as values found by assuming TRAPPIST-1 has radio flux consistent with the GBR.	104

List of Figures

Figure 1.1	The Hertzsprung-Russel diagram, developed in the early 1900s by Ejnar Hertzsprung and Henry Norris Russell. It shows the temperature and luminosity - or corresponding colour - of main sequence stars. The luminosity is typically normalised to the Solar luminosity, L_{\odot} . This image from the European Southern Observatory (ESO) is used with permission under the Creative Commons Attribution 4.0 International Licence.	3
Figure 1.2	Diagram of the internal structure of the Sun (left) and of a fully convective UCD (right). The tachocline, or dividing region between the Solar radiative and convective zones is thought to play a critical role in the production of the Solar magnetic field through the $\alpha\Omega$ dynamo.	10
Figure 1.3	Demonstration of the $\alpha\Omega$ effect. The Ω effect operates through differential rotation to convert poloidal magnetic field lines into toroidal magnetic field lines. The α effect then forms magnetic loops around the turbulent toroidal field lines, which in turn converts them into new poloidal field lines. Figure recreated from the Solar and STellar Activity Research Team at the Konkoly Observatory.	12

Figure 1.4	Schematic of the α^2 magnetic dynamo. Image (a) shows an initial toroidal magnetic field line. Image (b) shows small helical turbulence that generates poloidal eddies, which in turn generate poloidal electromotive forces in large-scale poloidal magnetic field loops seen in image (c). Image recreated from Blackman and Hubbard (2014).	15
Figure 1.5	The Güdel-Benz relation shows a tight correlation between the X-ray and radio luminosity of magnetically active stars, but is strongly violated by a population of UCDs (e.g. Williams et al., 2014). The plot above shows the Güdel-Benz relation of magnetically active F-through-M stars (Güdel, 1992; Güdel and Benz, 1993; Drake et al., 1992) and Solar flares (Benz and Güdel, 1994) on a logarithmic scale, where the uncertainties are of order 10% the measured luminosity.	18
Figure 1.6	The role of inclination i in spectroscopic measurements, which measure the projected $v \sin i$ rather than the true equatorial rotation rate, v	20
Figure 1.7	An emitting source oriented at angle θ relative to a detector, where the incoming flux at frequency ν is measured.	23
Figure 1.8	The steps involved in plasma emission, resulting in radiation at the fundamental and second harmonic of the plasma frequency. Reproduced from Melrose (1991).	28
Figure 1.9	The bump-in-the-tail distribution of electron velocities, where there is a greater number of higher velocity electrons (red shaded region) than lower velocity electrons (blue shaded region).	29

Figure 1.10	Distribution of electron velocities by parallel component $v_{ }$ (x-axis) and perpendicular component v_{\perp} (y-axis). The “inverted V” represents a region of population inversion in v_{\perp} , where a greater number of electrons have higher perpendicular velocity than have lower perpendicular velocity. “Beam” refers to the precipitating electron beam incident on the UCD atmosphere, while v_b refers to the initial beam velocity. The triangular conical shape represents the loss cone, where electrons with velocities approximately parallel to the magnetic field are lost to the stellar atmospheres. Used with permission from Treumann (2006).	32
Figure 1.11	The gyrosynchrotron relations from Dulk and Marsh (1982), reproduced here with permission. Each curve shows δ values of 3, 5, & 7, with solid lines showing viewing angles of 80° and dashed lines showing viewing angles of 40° . The six plots represent (a) the emission coefficient, (b) absorption coefficient, (c) effective temperature, (d) degree of circular polarisation.	41
Figure 1.12	During magnetic reconnection events, accelerated particles are released from the upper loop, whereas a population of mildly relativistic electrons is trapped within the lower loop - releasing radio emission through gyrosynchrotron radiation. This radio emission is one of the only ways to trace the energetic particles during these events. Artist’s conception, commissioned and used here with permission from Alexandra Lash.	42
Figure 2.1	Diagram of a simple two-element interferometer, with antennas 1 and 2 separated by baseline B . Incoming light will produce voltages V_1 and V_2 from each element, separated by a geometric time delay $\tau = B \sin \theta v/c$	46

Figure 2.2	Dirty beam produced by an interferometric measurement of one point on the u, v plane, in ambiguous sky coordinates, or the Fourier transform of the sampling function. They are produced by two antennas (left), four antennas (middle), and five antennas (right). The position of the antennas and baseline between them determines the distribution of sine waves in the pattern. Adding additional antennas is useful for filling in the u, v plane.	48
Figure 2.3	The radiation pattern produced by a radio telescope. The main lobe is where the majority of the signal is received, and is oriented toward the observing target. The side lobes, produced by the diffraction pattern of the beam, usually pick up radiation from outside the intended field of view.	49
Figure 2.4	3 GHz observations centred on TRAPPIST-1. The image is corrupted by significant artefacts caused by a bright quasar seen in the wide-field image on the right.	50
Figure 2.5	The cleaning process for the radio bright UCD LP 349-25, presented in the following Chapter. The “dirty” image constructed from the sampling of points on the $u - v$ plane. The following “clean” image has been processed using the CLEAN algorithm in the CASA software, which removes some of the structure of the dirty beam resulting from artefacts of an incompletely-sampled Fourier space.	53

Figure 2.6	The structure of VLA observations, as set up with their Observing Tool. The startup overhead has a fixed time of approximately seven minutes to slew from a previous observing target to the locations of the gain calibrator - usually a quasar with known flux - as well as account for delays due to wire wrapping in the antennas. The following set of calibrations, including pointing, flux, bandpass, and requant are usually done on the gain calibrator, but the phase calibrator can be used as well. If the observations are long enough, an additional flux calibration may be needed to break up observing scan loops as atmospheric conditions may change.	55
Figure 3.1	All detected UCDs. The visibilities are phase-shifted to account for the proper motion. LP 349-25 has peak flux of 70 μ Jy with RMS of 9 μ Jy, LSR J1835+3259 has a peak flux of 114 μ Jy with RMS 18 μ Jy, and NLTT 33370 has a peak quiescent flux of 604 μ Jy with RMS 7.3 μ Jy. The synthesized beam is denoted by the black ellipse in the bottom left of each image.	61
Figure 3.2	Time series of all NLTT 33370 observations presented in this work, including time on June 10th and June 12th, 2015. The data set was split into 30 s bins, and the peak flux and RMS were taken using the CASA task <i>uvmodelfit</i> . The two panels show the light curves of each day, while the overlaid plot shows the June 12 flare that reached a peak flux of 4880 ± 360 μ Jy. Due to the gaps in the data, it is unclear whether this flare repeats with the stellar rotation.	65

- Figure 3.3 Radio emission profiles of all three detected UCDs are shown. The kilometric radiation profiles of Jupiter and Saturn adapted from Zarka (1998) are plotted in blue and green, scaled to the peak flux and frequency of NLTT 33370, whereas the dotted lines correspond to fitted gyrosynchrotron models. The spectral indices of LP 349-25 and LSR J1835-46546 were determined by connecting the two existing data points for each UCD, and were $\alpha = -0.52$ and $\alpha = -0.76$, respectively. 69
- Figure 3.4 The size of the emitting region for a given magnetic field strength for all detected UCDs. The solid curves show the size of the emitting region given ~ 8.5 GHz flux density of each UCD, assuming this is in the transition region where $\tau = 1$. The dotted line at the bottom denotes the minimum size of the emitting region set by assuming the 97.5 GHz observations are in the optically thick regime where $T_b = T_{\text{eff}}$. The size of the emitting region is given in Jupiter radii R_J , characteristic of UCD sizes, while the magnetic field range is chosen to be representative of Solar to typical UCD values. Note that all y-scales are plotted logarithmically and the y-scale for NLTT 33370 extends to larger values than the other UCDs, potentially at least partially owing to contributions from both stars in this binary system or to enhanced magnetospheres due to a companion. 72

- Figure 4.1 Continuum images showing the $60'' \times 60''$ region around the positions of TRAPPIST-1 for my 97.5 GHz ALMA (left) and 44 GHz VLA (right) observations. The crosses at the centres of both images indicate the position of TRAPPIST-1. The synthesized beam is indicated by the black ellipses in the lower left of each image. TRAPPIST-1 was not detected, with RMS sensitivities of $5.34 \mu\text{Jy}$ and $3.52 \mu\text{Jy}$ in my VLA and ALMA observations, respectively. The brighter of the two unresolved bright spots in the ALMA image located to the NE of TRAPPIST-1 is likely a background object, whereas the other can be attributed to Gaussian noise. 78
- Figure 4.2 The Güdel-Benz relation between X-ray and $\sim 5 - 9$ GHz radio luminosity. Blue diamond data points represent Solar flares from Benz and Güdel (1994), green ‘x’ and blue circles represent magnetically active F, G, & K stars (Güdel, 1992; Drake et al., 1992). Dark green squares represent mid- to late-M dwarfs in line with the GBR (Güdel et al., 1993), whereas the orange stars show a population of ultracool dwarfs in violation of the GBR. Grey arrows show upper-limits on X-ray and/or radio luminosities of UCDs. TRAPPIST-1 is shown along the GBR with a red arrow. The upper limit in this plot uses the 6 GHz VLA observations by Pineda and Hallinan (2018) and the X-ray luminosity measured by Wheatley et al. (2017). Uncertainties are not plotted but are typically within 10%. Two of the detected UCDs presented in the previous chapter, NLTT 33370 and LSR J1835, with previously measured X-ray luminosity are shown as well (Berger et al., 2008a; Williams et al., 2015). 82

Figure 4.3	Constraints on the size of the emitting region and magnetic field strength for an assumed electron energy index δ in the optically thick gyrosynchrotron regime following Equation 3.1. In the case of optically thin emission, the emitting region can be enhanced by up to 10 for an optical depth $\tau(\nu) = 0.01$. The upper blue curves are set by the 6 GHz VLA observations presented in Pineda and Hallinan (2018), while the red and black curves are set by the 44 GHz VLA and 97.5 GHz ALMA observations presented in this work. The vertical black dotted line shows the magnetic field strength determined by Reiners and Basri (2010).	84
Figure 4.4	Continuum image showing the $12'' \times 12''$ region centred on the sky position of TRAPPIST-1 for my 3 GHz VLA observations. The crosses at the centre of the image indicate the position of TRAPPIST-1. The synthesized beam is indicated by the black ellipse in the lower left of the image. TRAPPIST-1 was not detected, with RMS sensitivity of $170 \mu\text{Jy}$. The streaking structure that resembles telescope tracking is due to artefacts introduced by the quasar.	87
Figure 4.5	Wide-field continuum image showing the $240'' \times 240''$ region centred around the sky position of TRAPPIST-1 for my 3 GHz VLA observations. The crosses at the centre of the image indicate the position of TRAPPIST-1. The synthesized beam is indicated by the black ellipse in the lower left of the image. This image is significantly zoomed out in order to show the bright quasar, seen in the top right, that introduced significant noise-like artefacts into the observations and raised the RMS.	89
Figure 5.1	Diagram comparing the orbits of the inner Solar System planets, with semi-major axes ranging from 0.38 – 0.72 au to the TRAPPIST-1 planetary system, with semi-major axes ranging from 0.01 – 0.06 au.	92

Figure 5.2	The plot from Tilley et al. (2017) on the left (a) shows the effects of an electromagnetic radiation only single flare on the ozone column on an Earth-like atmosphere, while the plot on the right (b) shows the effects of the same flare with the addition of energetic proton fluxes ranging from $\sim 3 \times 10^5$ pfu for the $10^{30.5}$ erg flare to $\sim 6 \times 10^8$ pfu for a 10^{34} erg flare. Note the split legend. Used with permissions under the Creative Commons CC-BY-NC license.	95
Figure 5.3	Schematic of the propagation of helio longitudinal flux tubes from the Sun, where outgoing particles extend along interplanetary magnetic field lines.	99

List of Symbols

$''$	arcsecond
α	spectral index
δ	electron energy index
au	astronomical unit
Jy	Jansky
L_{\odot}	Solar Luminosity
M_{\odot}	Solar Mass
M_{*}	Stellar Mass
M_J	Jupiter Mass
pc	parsec
R_{\odot}	Solar Radius
R_{*}	Stellar Radius
R_J	Jupiter Radius

List of Abbreviations

ALMA	Atacama Large Millimeter Array
CASA	Common Astronomy Software Applications
CME	coronal mass ejection
EB	execution block
ECMI	electron cyclotron maser instability
EMF	electromotive force
ESO	European Southern Observatory
FAST	Five hundred metre Aperture Spherical Telescope
GBR	Güdel-Benz relation
IR	infrared
ISM	interstellar medium
JWST	James Webb Space Telescope
LOFAR	Low-Frequency Array
LSA	Large Southern Array
MFM	mean-field magnetohydrodynamics
MMA	Millimetre Array
NAOJ	National Astronomical Observatory of Japan
NASA	National Aeronautic and Space Agency
NOAA	National Oceanic and Atmospheric Association
NSF	National Science Foundation
NRAO	National Radio Astronomy Observatory
pfu	particle flux units
PI	principle investigator
PWV	precipitable water vapour

RA	right ascension
RMS	root-mean-squared
SB	scheduling block
SEP	Solar energetic particle
SNR	signal to noise ratio
SPE	Solar particle event
SPW	spectral window
TESS	Transiting Exoplanet Survey Satellite
TRAPPIST	Transiting Planets and Planetesimals Small Telescope
UCD	ultracool dwarf
UV	ultraviolet
VLA	Very Large Array
WVR	water vapour radiometer

Dedication

This one's for me.

Chapter 1

Introduction to Ultracool Dwarfs

Low-mass stars and brown dwarfs are among the most common objects in the Milky Way, yet their low brightness makes them difficult to study. They were long expected to be so dim at radio frequencies that they would be undetectable by even the most sensitive radio telescopes. However, a surprising 10% of them are very bright at radio frequencies with emission exceeding predicted values by up to four orders of magnitude (Antonova et al., 2013; Route and Wolszczan, 2016; Lynch et al., 2016; Berger, 2006). The explanations for this radio brightness are still under investigation. In this thesis, I explore gyrosynchrotron radiation, especially at frequencies in the range of 30 – 100 GHz as a possible component of UCD radio brightness. The detected gyrosynchrotron radiation could originate from magnetic reconnection events that, if similar to Solar activity, can also cause a space weather environment that is inhospitable to surrounding Earth-like planetary atmospheres. The possible impacts of gyrosynchrotron-emitting UCDs on any surrounding planets are explored.

1.1 M Dwarfs

Stars are broadly categorized by their spectra under the Harvard spectral classification into the types O, B, A, F, G, K, and M, ranging from the bluest stars (spectral type O) to the reddest stars (spectral type M). Along the main sequence the spectra

also correspond to mass and temperature, where O type stars are the hottest and most massive, whereas M type stars are the coolest and lowest mass. Each spectral type is further subdivided by temperature along a decimal scale from 0 (hottest) to 9 (coolest). The hottest stars along this sub-sequence are often referred to as *early-type*, whereas the coolest stars are referred to as *late-type*. These colloquial terms originate from the outdated idea that stellar evolution follows the sequence of spectral types, with stars beginning their lives as bright, hot O-type stars and slowly burning through their fuel and expelling mass to become cool, dim M-type stars (MacPherson, 1920). While this theory has since been abandoned following the discovery of red giants and stellar nuclear fusion, giving rise to modern stellar evolution theory (Beccari and Carraro, 2015), these terms are still used as a proxy for temperature in sub-classes. The distribution of spectral types is generally represented by the Hertzsprung-Russel diagram, a log-log plot showing the luminosity, typically normalised to that of the Sun, L_{\odot} , and effective temperature of stars (Fig. 1.1). The continuous band of stars is known as the Main Sequence. Stars on this sequence are powered by the fusion of hydrogen into helium.

Large stellar surveys throughout the 20th century and into the 21st century have shown that stars in the Solar neighbourhood are not evenly distributed across spectral type. An estimated 75% of all stars in the Milky Way fall into spectral type M, defined by the photosphere temperature range 2300 – 3800 K and the mass range $0.075 - 0.6 M_{\odot}$ (Henry et al., 2006). However, despite their abundance, no M stars - or “M dwarfs” in reference to their small size when along the main sequence - are visible to the unaided eye. Even the brightest M0 star, Lacaille 8760, has less than 10% the Sun’s luminosity and has an apparent luminosity, or brightness as seen from Earth, just below the physical limits of the human eye. The low luminosities of M dwarfs have long impeded their discovery and characterisation. The closest neighbouring star to the Sun, M5.5 dwarf Proxima Centauri, was not discovered until the early 1900s despite being just 4.2 light-years away.

Around masses of $0.35 M_{\odot}$ and less, M dwarfs become fully convective (discussed in detail in Section 1.3.1). While more massive, Sun-like stars are only able to access 10% of their hydrogen for fusion, fully convective M dwarfs can burn through much larger reserves, nearly all of their fuel. Additionally, their low masses mean that M dwarfs burn through their fuel at much slower rates than larger stars

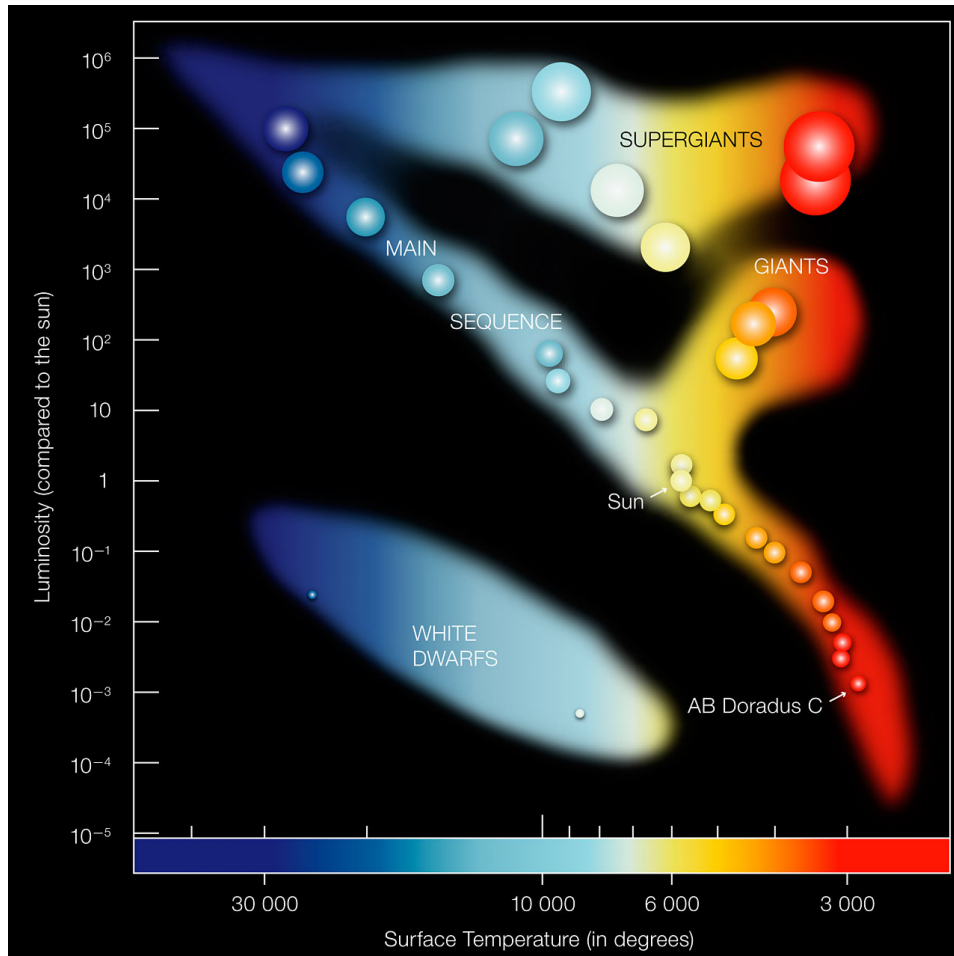


Figure 1.1: The Hertzsprung-Russell diagram, developed in the early 1900s by Ejnar Hertzsprung and Henry Norris Russell. It shows the temperature and luminosity - or corresponding colour - of main sequence stars. The luminosity is typically normalised to the Solar luminosity, L_{\odot} . This image from the European Southern Observatory (ESO) is used with permission under the Creative Commons Attribution 4.0 International Licence.

due to lower gravitational pressure (Iben, 1967). These two factors enable M dwarfs to have exceptionally long lifetimes compared to their more massive counterparts, with the lowest-mass M dwarfs predicted to have hydrogen burning timescales of $\tau_H \sim 10^{13}$ yr (Laughlin et al., 1997), longer than the age of the universe. Because of their exceptionally long lifetimes and formation timescales, every M dwarf that has ever formed is still in the hydrogen burning stage, and still resides on the main sequence unless it has been disrupted by an external force.

The differences in stellar evolution between M dwarfs and larger stars extends beyond lifetimes. Stellar rotation can be used as a proxy to measure age, where F, G, and K stars older than 500 Myr have stellar rotation rates, ω , that decrease with age, t , roughly as $\omega \propto t^{-1/2}$ (Skumanich, 1972). M dwarfs spin down as they age due to the interaction between their magnetic field and stellar wind, which transfers angular momentum from the star to the wind. However, unlike F, G, K, and early-M stars, mid-to-late M dwarfs appear to have brief but very rapid spindown periods. Fully convective M dwarfs can maintain rapid rotation rates (Period < 10 day) for $\lesssim 2$ Gyr on the main sequence, followed by a sudden decrease to rotation periods of 100 days by an age of 5 Gyr. Newton et al. (2016) determined this by measuring the photometric rotation rates and galactic kinematics of mid-to-late M dwarfs to find a correlation with age, and rapid spin-down is suggested by the lack of intermediate rotation rates in mid-to-late M dwarfs.

Substantial magnetic activity is observed in younger M dwarfs, but is seen to decrease with age. While the precise ages of large M dwarf populations are difficult to determine directly, the position of the stars along the galactic plane can be used to infer age (Bensby et al., 2003; Fuhrmann, 1998). The ‘thin’ disc extends to scale heights of around 120 pc, and from ongoing star formation and element abundances is determined to be young, whereas the ‘thick’ disc extends to 300 pc, and determined to be older from its composition and the lack of dust and gas (Kilic et al., 2017; Girard and Soubiran, 2006). Surveys of M dwarfs show a stark decrease in magnetic activity with increasing vertical distance along the galactic plane (West et al., 2006), indicating that the more active M dwarfs reside in the young, thin disc, while the older M dwarfs reside in the older, thick disc. Other signatures of magnetic activity in M dwarfs are seen to decrease at ages of around 5-7 Gyr; H α and sometimes corresponding X-ray emission are observed in younger M dwarfs

(Newton et al., 2017; Stelzer et al., 2013; Reid et al., 1995), as well as higher starspot coverage (O’Neal et al., 2004). Heightened levels of magnetic activity are common for younger stars, but M dwarfs have prolonged lifetimes leading to extended levels of high activity and a steep decrease in magnetic activity at the transition from younger to older phases, which is not observed in other spectral types.

When M dwarfs do eventually age off and leave the main sequence, the behaviour of low-mass M dwarfs is expected to diverge from that of Sun-like stars. Early to mid-M dwarfs are expected to follow the familiar evolution into a red giant. Increases in temperature are small due to high opacity, therefore the increases in luminosity lead to increases in radii following $L=4\pi R^2\sigma T^4$. Curiously, simulations suggest that this will not occur for M dwarfs with masses less than $0.25 M_{\odot}$. Instead, these very low-mass M dwarfs will have roughly constant radius but increase in temperature (Adams et al., 2005). The star then becomes a hypothetical “blue dwarf”, having the same size as a red dwarf, but higher temperatures. Blue dwarfs remain hypothetical objects because the main sequence lifetimes of M dwarfs exceed one Hubble time, or roughly the age of the universe.

Between their extensive lifetimes and their ubiquity, M dwarfs are frequent hosts of terrestrial planets. Dressing and Charbonneau (2015) estimate from the Kepler sample that M dwarfs have a higher frequency of planets orbiting in the habitable zone where an Earth-like planet could support liquid water, after correcting for observational biases. They estimate an average of about 0.43 potentially habitable planets per star for orbital periods shorter than 50 days; or as high as one planet per star if desert worlds, or hot close-orbiting terrestrial planets with low water content, are considered (Zsom et al., 2013). In general, M dwarfs host significantly more terrestrial planets and fewer giant planets than Sun-like stars, likely resulting from a difference in the planet formation process associated with lower-mass stars (Alibert and Benz, 2017; Miguel et al., 2020). Not only are close-orbiting terrestrial planets more readily formed around M dwarfs, they are also easier to characterise using the transit method. The low luminosities of M dwarfs mean that Earth-sized planets make deeper transits as they cross the stellar disc, and the proximity to their host star means short orbital periods, which are additionally easier to confirm in transit surveys. The ubiquity of such planets around M dwarfs puts the stars themselves into the centre of the habitability discussion. However, one of the

important consequences of M dwarf magnetic activity is the potentially damaging effects it might have on surrounding planets.

The habitable zones of cool stars are located at smaller stellocentric distances compared to the Earth-Sun separation (discussed in detail in Chapter 5). Their proximity to the host star makes such planets particularly vulnerable to stellar magnetic activity. Unfortunately, M dwarfs show high levels of magnetic variability, including flares that are a thousand times stronger than the strongest Solar event and starspots that can cover half of the stellar surface (Lloyd et al., 2018; Jackson and Jeffries, 2013). Close-orbiting planets are often assumed to be tidally locked, having orbits synchronous with their rotation (Heller et al., 2011; Barnes, 2017; Yang et al., 2013; Kasting et al., 1993), potentially complicating the process of planetary magnetic field generation given magnetic dynamo scaling laws. Grießmeier et al. (2004a,b) find this to be the case for hot Jupiters, with the expectation that this will also affect terrestrial planets in the habitable zone of low-mass stars (Khodachenko et al., 2009), possibly leaving the planets with little defence against stellar magnetic activity. However, it is the subject of ongoing research whether synchronous rotation is indeed prohibitive of magnetic field generation in planets (Driscoll and Barnes, 2015), or whether close-orbiting planets must be tidally locked at all (Leconte et al., 2015; Delisle et al., 2017). Mercury and the Moon are strong counter-examples to the notion that tidal locking prohibits magnetic field generation, with Mercury hosting a global magnetic field of 0.07 Gauss equatorial strength and the Moon having likely previously hosted a magnetic field of up to 1 Gauss (Connerney and Ness, 1988; Green et al., 2020).

1.2 Brown Dwarfs

Brown dwarfs are a sub-stellar class of objects occupying the mass range between planets and stars. The precise definition of a brown dwarf is still the subject of debate, but can be defined in two ways: either by their formation mechanism or by their mass (Basri, 2000). The formation definition states that brown dwarfs are objects that form via core-collapse like stars but have masses below the hydrogen-burning mass limit, and are left with a protoplanetary disc of their own (Chabrier et al., 2000).

Table 1.1: Properties of M dwarfs by spectral sub-class.

Class	T_{eff} (K)	Mass (M_{\odot})	Radius (R_{\odot})
M0	3800	0.60	0.62
M1	3600	0.49	0.49
M2	3400	0.44	0.44
M3	3250	0.36	0.39
M4	3100	0.20	0.26
M5	2800	0.14	0.20
M6	2600	0.10	0.15
M7	2500	0.09	0.12
M8	2400	0.08	0.11
M9	2300	0.075	0.08

The mass definition states that brown dwarfs are defined by their mass only; a brown dwarf is an object massive enough to ignite deuterium burning ($M > 13 M_{\text{Jupiter}}$), but not massive enough to fuse hydrogen into helium ($M < 80 M_{\text{Jupiter}}$). It is interesting to note that in the formation definition brown dwarfs do not need to have sufficient mass to ignite deuterium burning, so in principle they could be planetary mass but differ only by their formation mechanism. Such objects are sometimes referred to as sub-brown dwarfs or planetary mass brown dwarfs. For the purposes of this thesis I use the mass definition, as my work is concerned with the emission processes and not the formation mechanism.

Brown dwarfs were initially theorized in 1963 by Shiv Kumar, who used the term “black dwarf” to describe stars of mass $< 0.05 M_{\odot}$ (Kumar, 1962). Kumar numerically determined that there was a limiting mass, below which contracting stars would not be able to reach sufficient core temperatures and pressures to ignite hydrogen fusion, and would instead contract until they were fully supported by electron degeneracy pressure. The terminology was subsequently changed to “brown dwarf” by Jill Tarter because black dwarf was already in usage for white dwarf remnants and brown was expected to be their approximate visible colour, which we now know to be closer to purple by human eye standards (Tarter, 2014). Despite these initial advances in brown dwarf theory, the first brown dwarf was not observed until over 30 years later, when Teide 1 was discovered in the Pleiades cluster (Rebolo et al., 1995).

Table 1.2: Properties of brown dwarfs by spectral type.

Class	T_{eff} (K)	Mass (M_{Jupiter})
L	1500 - 3000	50 - 79
T	500 - 1500	20 - 50
Y	250 - 500	5 - 30

Keck spectroscopic observations showed that Teide 1 still had the abundance of lithium consistent with its initial values, confirming that Teide 1 was unable to deplete lithium during thermonuclear fusion (Rebolo et al., 1996). This “lithium test” is one of the few ways that high-mass brown dwarfs can be distinguished from low-mass stars. Low-mass stars burn through their initial lithium supply within ~ 100 Myr, but brown dwarfs do not reach temperatures sufficient to deplete their lithium (Basri, 1998). It is possible for larger stars like the Sun to retain a significant portion of lithium in their convective layers which do not reach the conditions needed for lithium fusion, but these stars can be easily distinguished by their mass and luminosity.

Despite their mass range, brown dwarfs are all roughly the same radius as Jupiter. Brown dwarfs are compact because, like white dwarfs, they are primarily being supported by electron degeneracy pressure, where brown dwarf radius R is inversely proportional to the cube root of the mass. However, the small contribution of internal thermal pressure to fully balance the object’s self-gravity makes the highest mass brown dwarfs slightly ‘bloated’ relative to the case of a fully degenerate object, something that does not occur for the lowest mass brown dwarfs. Because of this, all brown dwarfs are roughly the same radius (Chabrier et al., 2009).

Some brown dwarfs are technically classified as spectral type M, despite not having sufficient temperature to ignite hydrogen fusion. Lower mass (cooler) brown dwarfs are subdivided into L, T, and Y dwarfs. The properties of brown dwarf spectral types are shown below in Table 1.2.

1.3 Magnetic Dynamos

The twentieth century saw large advances in stellar cataloguing, with surveys such as Hipparcos (HIP) and Smithsonian Astrophysical Observatory Star Catalog (SAO) recording the position and proper motion of hundreds of thousands of stars (Perryman et al., 1997; Whipple, 1966). Despite the high number of targets, many surveys were not sensitive to late-type M dwarfs, leaving a gap in our knowledge about stellar populations at the bottom of the main sequence. Early efforts to take census of the lowest-mass M dwarfs were not able to distinguish them from high-mass brown dwarfs, leading to the umbrella term “ultracool dwarf” that encompasses both objects (Kirkpatrick et al., 1997). This turned out to be a helpful categorisation, as the internal structure and behaviour of both low-mass stars and brown dwarfs are very similar, and both depart significantly from that of Solar-type stars.

1.3.1 The $\alpha\Omega$ Dynamo

The Solar interior is divided into three regions - a core extending out to 0.25 Solar radii, an inner radiative zone surrounding the core out to 0.7 Solar radii, and an outer convective zone. Energy released during fusion in the core is carried outward through electromagnetic radiation and particle collisions. In the convective zone, however, plasma current cells carry heat out from the radiative zone. The dividing region between the inner radiative and outer convective zone is called the tachocline, and is thought to play a fundamental role in magnetic field generation for Solar-like stars.

Whether a region is radiative or convective is dependent on the local value of the opacity, which is related to the temperature and density by Kramer’s Law,

$$\kappa \propto \rho T^{-3.5}, \quad (1.1)$$

where κ is the opacity, ρ is the stellar density, and T is the stellar temperature. Part of the star becomes unstable to convection when the opacity is high. A large value of κ increases the magnitude of the temperature gradient $|dT/dr|$ such that the temperature of an adiabatically displaced parcel of gas does not drop as much as the ambient medium, thus becoming buoyant. Convection in turn transports heat,

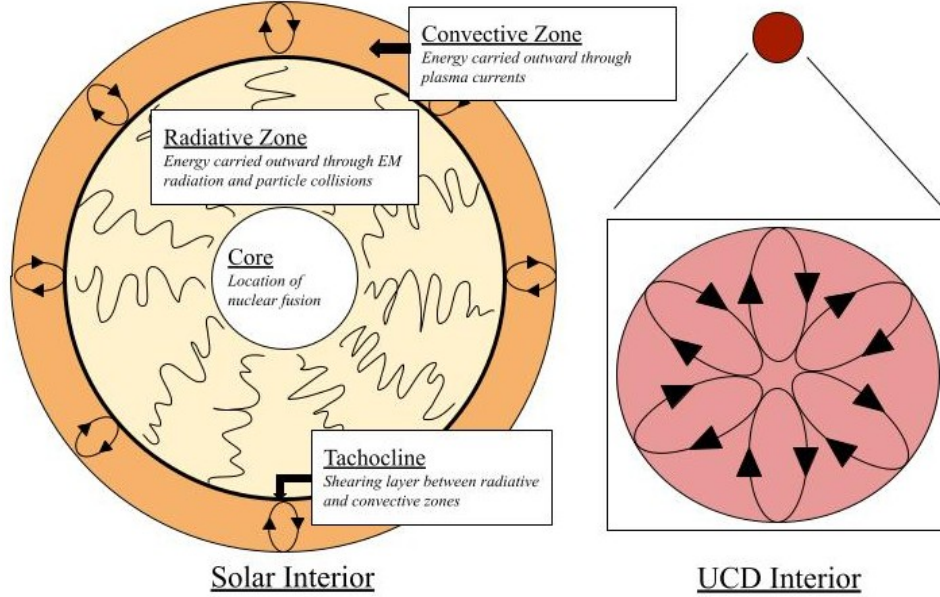


Figure 1.2: Diagram of the internal structure of the Sun (left) and of a fully convective UCD (right). The tachocline, or dividing region between the Solar radiative and convective zones is thought to play a critical role in the production of the Solar magnetic field through the $\alpha\Omega$ dynamo.

and rearranges the structure of the interior. The precise conditions necessary for convection are given by the Schwarzschild criterion for instability,

$$\left| \frac{dT}{dr} \right| > \left| \frac{dT}{dr} \right|_{\text{ad}}, \quad (1.2)$$

where $|dT/dr|$ is the temperature gradient in the stellar interior and $|dT/dr|_{\text{ad}}$ is the adiabatic gradient. High opacity regions in stars satisfy this criterion, leading to convection. In the Sun, the radiative region is stable against convection, but as the temperature decreases further from the core, the opacity becomes high and the Schwarzschild criterion for instability is met. In more massive and hotter stars, the radiative zones extend further outward and convective zones are thinner. Low-mass stars have deep convective shells and smaller radiative zones. At sufficiently low masses, the temperature is never high enough and opacity never low enough to ensure convective stability, and the stars lack a radiative zone (Limber, 1953).

Stellar evolution models show that the onset of a fully convective envelope, where the convective region extends down to the core, is at around $0.3 M_{\odot}$, or spectral type of M3.5 (Chabrier et al., 2000).

The lack of a radiative zone in low-mass stars and brown dwarfs has important consequences for magnetic field generation. In the Sun, the radiative and convective zones are separated by the aforementioned tachocline, a thin (0.04 Solar radii) transition region. The tachocline is the site of the strongest shearing due to the interface between the rigidly rotating radiative layer and convective zone (Spiegel and Zahn, 1992). In Sun-like stars, magnetic field generation through a dynamo is thought to depend critically on the tachocline. When the star is fully convective, however, the tachocline vanishes and the same dynamo models no longer apply. If fully convective stars and brown dwarfs do generate and sustain strong magnetic fields, they must do so by a different dynamo mechanism altogether (e.g., Gilman, 2005; Kao, 2017; Chabrier and Küker, 2006), discussed in detail in the following section.

The large-scale Solar magnetic field is most likely produced by a hydrodynamic dynamo, wherein conductive fluid or plasma moving through a magnetic field induces a current, which produces stronger magnetic field lines. The dynamo action is successful if more magnetic energy is amplified than is drained through magnetic diffusion. The Solar dynamo is thought to be sustained by the complementary actions of poloidal and toroidal components of the magnetic field resulting from the differential rotation in the Solar interior both latitudinally and radially. Differential velocities of conducting plasma regions can stretch a poloidal field, which in turn produces a toroidal field in a process called the Ω effect. The poloidal field is then amplified through a complex process called the α effect, where the three-dimensional fluid motions within the convective region twist toroidal magnetic field lines, converting them into small-scale poloidal fields. The combined effect of these small-scale poloidal fields produces a large-scale global poloidal field, completing the $\alpha\Omega$ dynamo effect (Figure 1.3).

While the α effect requires stratified rotation of plasma in the convection zone, the Ω effect relies on the differential rotation about the tachocline in order to sufficiently amplify the magnetic field. The convection zone is turbulent and buoyantly unstable, making it difficult for magnetic flux to reach the observed

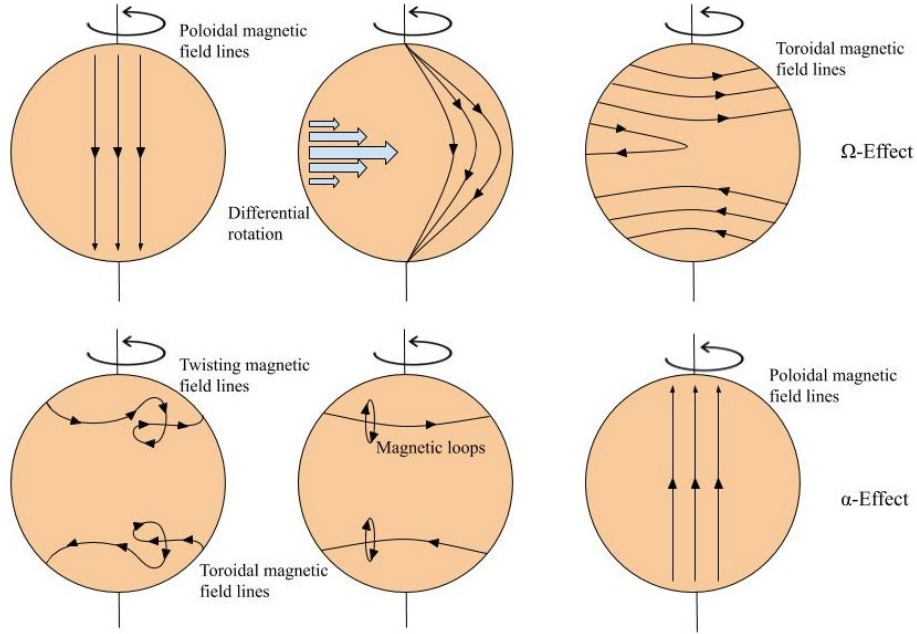


Figure 1.3: Demonstration of the $\alpha\Omega$ effect. The Ω effect operates through differential rotation to convert poloidal magnetic field lines into toroidal magnetic field lines. The α effect then forms magnetic loops around the turbulent toroidal field lines, which in turn converts them into new poloidal field lines. Figure recreated from the Solar and STellar Activity Research Team at the Konkoly Observatory.

strengths before being expelled. The tachocline, however, is able to store magnetic flux long enough to develop into strong magnetic fields. In this interface dynamo model, seed magnetic fields are transported to the tachocline, where the strong shear causes poloidal field lines to stretch and twist, forming a toroidal field. This brings toroidal structures back up into the convection zone, where the turbulent magnetic fields enable the α effect to amplify the poloidal field (Parker, 1993). The combined action of these two effects is enough to sustain a strong magnetic field in stars with a tachocline (Miesch et al., 2009).

1.3.2 Mean-Field Magnetohydrodynamics

The complicated three-dimensional dynamo processes can be conveniently simplified with the use of mean-field magnetohydrodynamics, a mathematical formalism designed to show the effect of small-scale processes in generating global stellar magnetic fields (Steenbeck and Krause, 1969). In mean-field magnetohydrodynamics (MFM), the magnetic and velocity field are separated into mean components \vec{B}_0 and \vec{v}_0 that vary over a length scale L , and fluctuating components \vec{b} and \vec{v} that vary over a smaller length-scale l , where $l \ll L$. The magnetic and velocity fields can be expressed as the total of these components,

$$\begin{aligned}\vec{B} &= \vec{B}_0 + \vec{b} \\ \vec{V} &= \vec{v}_0 + \vec{v},\end{aligned}\tag{1.3}$$

where the averages taken over an intermediate length scale between l and L are $\langle \vec{b} \rangle = \langle \vec{v} \rangle = 0$, $\langle \vec{B} \rangle = \vec{B}_0$, and $\langle \vec{V} \rangle = \vec{v}_0$. The starting point for MFM is the equation of magnetic inductance, which is derived from Ohm's law for moving conductors in a stationary magnetic field,

$$\vec{J} = \sigma(\vec{E} + \vec{V} \times \vec{B}),\tag{1.4}$$

where \vec{J} is the electric current, \vec{E} is the electric field, \vec{V} is the velocity field, \vec{B} is the magnetic field, and σ is the electrical conductivity of the material. The resulting equation of magnetic inductance thus has the form,

$$\frac{\partial \vec{B}}{\partial t} = \eta \nabla^2 \vec{B} + \nabla \times (\vec{V} \times \vec{B}),\tag{1.5}$$

where $\eta = \frac{1}{\mu\sigma}$ is the magnetic diffusivity, and μ is the permeability of free space. The induction equation for an averaged magnetic field $\langle \vec{B} \rangle$ is,

$$\frac{\partial \vec{B}_0}{\partial t} = \eta \nabla^2 \vec{B}_0 + \nabla \times \vec{\mathcal{E}} + \nabla \times (\vec{v}_0 \times \vec{B}_0),\tag{1.6}$$

where $\vec{\mathcal{E}} = \langle \vec{v} \times \vec{b} \rangle$ is the mean turbulent electromotive force (EMF) caused by interactions between the small-scale velocity and magnetic fields. The EMF $\vec{\mathcal{E}}$ can

be rewritten in terms of the mean field and its derivatives in order to obtain a final expression. Subtracting Equation 1.6 from the inductance Equation 1.5 gives,

$$\frac{\partial \vec{b}}{\partial t} = \nabla \times (\vec{v}_0 \times \vec{b}) + \nabla \times (\vec{v} \times \vec{B}_0) + \nabla \times (\vec{v} \times \vec{b} - \varepsilon) + \eta \nabla^2 \vec{b}. \quad (1.7)$$

In Equation 1.7, \vec{b} is driven by the term $\nabla \times (\vec{v} \times \vec{B}_0)$, where the small-scale turbulent motion of \vec{v} acts on the mean field \vec{B}_0 . Thus, the EMF will be related to the mean magnetic field, and can then be expanded in a Taylor series, $\vec{\varepsilon}_i = \alpha_{ij} \vec{B}_{0j} + \beta_{ijk} \partial \vec{B}_{0j} / \partial x_k + \dots$, where α_{ij} and β_{ijk} are tensors dependent on \vec{v}_0 and \vec{v} . In the approximation of isotropic turbulence, they can be rewritten as $\alpha_{ij} = \alpha \delta_{ij}$ and $\beta_{ijk} = \beta \epsilon_{ijk}$. Plugging this new expression for the EMF into Equation 1.6, to leading order,

$$\frac{\partial \vec{B}_0}{\partial t} = (\eta + \beta) \nabla^2 \vec{B}_0 + \nabla \times (\alpha \vec{B}_0) + \nabla \times (\vec{v}_0 \times \vec{B}_0). \quad (1.8)$$

The new terms α and β are now scalars. The α effect, given by the $\nabla \times \alpha \vec{B}_0$ term in Equation 1.8, shows the amplification of the magnetic field due to helical turbulence. The Ω effect arises from the $\nabla \times (\vec{v}_0 \times \vec{B}_0)$ term in Equation 1.8, where differential rotation can lead to the generation of a toroidal magnetic field from a seed poloidal field. Magnetic diffusivity is accounted for by the remaining term in Equation 1.8 given by $(\eta + \beta) \nabla^2 \vec{B}_0$. While the Ω effect accounts for the curl of the vector perpendicular to the magnetic field, the α effect is due to the curl of the vector acting parallel to the mean magnetic field.

1.3.3 The α^2 Dynamo

The α effect is of critical importance in both the $\alpha\Omega$ and the α^2 dynamo model, discussed below. It was originally described by Parker (1955) as the sum of “cyclonic events” in a stellar interior. A single cyclonic event involves twisting of magnetic field lines as fluid rises in the convective region of stars. These short-lived events generate a component parallel or antiparallel to the seed magnetic field depending on the angle of rotation. The sum of all events is a twisting of toroidal lines into additional poloidal field lines as long as there is an asymmetry in the

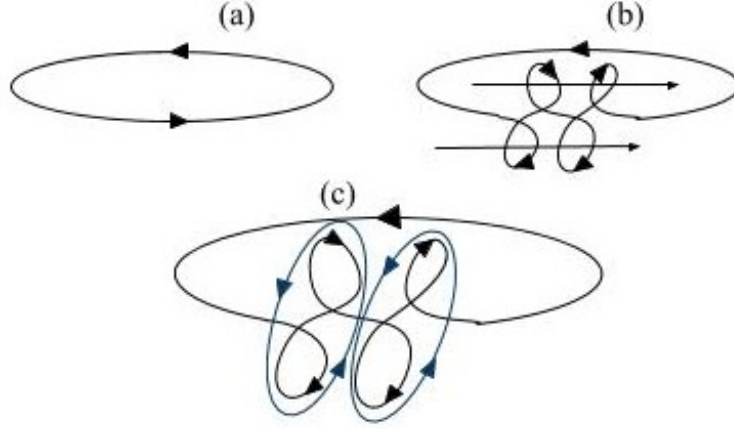


Figure 1.4: Schematic of the α^2 magnetic dynamo. Image (a) shows an initial toroidal magnetic field line. Image (b) shows small helical turbulence that generates poloidal eddies, which in turn generate poloidal electromotive forces in large-scale poloidal magnetic field loops seen in image (c). Image recreated from Blackman and Hubbard (2014).

velocity field and the positive and negative contributions to the α effect do not sum to zero. In the $\alpha\Omega$ dynamo it is the combined result of the α and Ω effects that generates a large-scale magnetic field.

In the absence of a shear caused by differential rotation about a tachocline, UCDs are not expected to generate magnetic fields via the $\alpha\Omega$ mechanism. Magnetic dynamo models for UCDs instead rely on Coriolis forces acting on three-dimensionally turbulent and stratified plasma. In this model, initial toroidal magnetic field lines are twisted through small helical eddies that create poloidal field loops. These loops generate a poloidal electromotive force in the same direction, resulting in large-scale poloidal magnetic field loops. In this Solar $\alpha\Omega$ dynamo model, the Ω shear is more effective in amplifying the magnetic field than the α effect, but this need not be the case for alternative dynamo models. In a fully convective dynamo, stratification and rotation in the magnetic field are crucial to amplify the magnetic field via the α effect alone, leading to the so-called α^2 dynamo (see Figure 1.4).

In the case of non-isotropic turbulence, expected in the convective zones of rapidly rotating UCDs, α_{ij} can be re-expressed as a tensor. Following Küker and Rüdiger (1999), the α effect due to density (ρ) stratification is given by,

$$\alpha_{ij}^\rho = -\delta_{ij}(\vec{\Omega}\vec{G})\alpha_1^\rho - (\Omega_j G_i + \Omega_i G_j)\alpha_2^\rho - (\Omega_j G_i - \Omega_i G_j)\alpha_3^\rho - \frac{\Omega_i \Omega_j}{\Omega^2}(\vec{\Omega}\vec{G})\alpha_4^\rho, \quad (1.9)$$

where Ω is the angular velocity of the star and the vector $\vec{G} = \nabla \log \rho = G\hat{r}$, α_1 , α_2 , α_3 , and α_4 are the mean-field coefficients that depend on the global rotation (Ruediger, 1978), and \hat{r} points in the radial direction. In polar coordinates, the α tensor can be written,

$$\alpha^\rho = c_\alpha \Omega^* G \tau_{\text{corr}} v_t^2 \begin{pmatrix} A_1 \cos \theta & 0 & A_2 \cos \theta \\ 0 & A_1 \cos \theta & 0 \\ A_2 \cos \theta & 0 & A_3 \cos \theta \end{pmatrix}, \quad (1.10)$$

where c_α is a dimensionless parameter ranging between 0 and 1, θ is the colatitude, $\Omega^* = 2\tau_{\text{corr}}\Omega$ is the Coriolis number, τ_{corr} is the turnover time for stellar convection, Ω is the angular frequency of rotation, and v_t is the intensity of the fluctuating velocity, $v_t = \sqrt{\langle \vec{v} \rangle^2}$. The prefactors A_1 , A_2 , and A_3 are given by,

$$A_1 = \frac{1}{\Omega^{*4}} \left[6 + \Omega^{*2} - \frac{6 + 3\Omega^{*2} - \Omega^{*4}}{\Omega^*} \arctan \Omega^* \right] \quad (1.11)$$

$$A_2 = \frac{6}{\Omega^{*4}} \left[3 - \frac{3 + \Omega^{*2}}{\Omega^*} \arctan \Omega^* \right] \quad (1.12)$$

$$A_3 = \frac{2}{\Omega^{*4}} \left[\frac{6 + 7\Omega^*}{1 + \Omega^{*2}} - 3 \frac{\Omega^{*2} + 2}{\Omega^*} \arctan \Omega^* \right]. \quad (1.13)$$

Note that A_3 approaches negative infinity as the Coriolis number Ω^* approaches 0, limiting the validity of this approach to situations where the object has nonzero rotation and convective turnover. In the case of rapid rotation where $\Omega^* \gg 1$, the Coriolis number in the prefactor is cancelled by the Ω^* dependence in Equations 1.11 through 1.13, and the strength of the α effect is no longer dependent on rotation. Thus in the α^2 dynamo the efficacy of the α effect is directly related to the value of Ω^* up to a saturation point, after which it becomes independent of rotation. Diffusion in the α^2 dynamo is due to turbulence, and decreases with increasing Ω^* .

This leads to the overall outcome that the α^2 dynamo generates magnetic fields with strength dependent on the rotation rate.

Like the $\alpha\Omega$ dynamo, this α^2 dynamo is related to the stellar rotation, but unlike the $\alpha\Omega$ dynamo, there is no dependence on differential rotation. Rotation in the α^2 dynamo is important for generating turbulence and kinetic energy to create magnetic helicity. Using the above equations, simulations of the α^2 dynamo show that for fully convective stars and brown dwarfs, it can generate magnetic fields of up to kiloGauss strength, and that rapid rotation can generate even stronger fields due to decreased diffusion (Chabrier and Küker, 2006). If ultracool dwarfs do generate magnetic fields via the α^2 dynamo, one might expect a correlation between rotation rate and magnetic field strength.

1.4 Radio Observations of UCDs

The need for a fully convective magnetic dynamo in stars is relatively recent. It was long assumed that without differential rotation about a tachocline, UCDs would not be able to generate significant magnetic fields or magnetic activity at all, although planetary-mass objects hint that this assumption may not be correct. Nevertheless, taking this view, since magnetic activity can be traced by emission at radio frequencies, it was likewise assumed that UCDs would be radio quiet. This assumption that UCDs would be radio quiet is strongly bolstered by observations of other magnetically active stars.

The X-ray and radio luminosities of most magnetically active F through mid-M stars are tightly correlated in what is known as the Güdel-Benz relation (Güdel and Benz, 1993). The Güdel-Benz relation (GBR) is well described by a single power law that extends through 10 orders of magnitude (Fig. 1.5), suggesting a common emission mechanism. The prevailing model is that radio-emitting nonthermal electrons are accelerated in magnetic events, which then heat the coronal plasma, prompting the release of soft X-rays. Extrapolating from the GBR, the expected radio emission of UCDs would be less than 0.1 μJy , undetectable by any existing radio telescope.

Initial indications that UCDs may actually be magnetically active came in the form of flares seen in very low-mass M dwarfs at optical, UV, and X-ray wavelengths

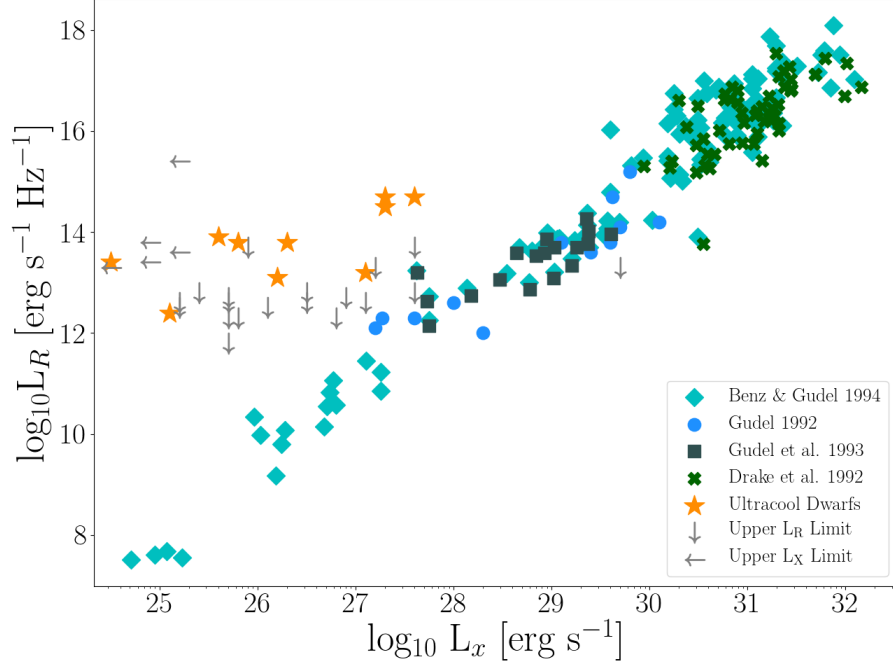


Figure 1.5: The Güdel-Benz relation shows a tight correlation between the X-ray and radio luminosity of magnetically active stars, but is strongly violated by a population of UCDs (e.g. Williams et al., 2014). The plot above shows the Güdel-Benz relation of magnetically active F-through-M stars (Güdel, 1992; Güdel and Benz, 1993; Drake et al., 1992) and Solar flares (Benz and Güdel, 1994) on a logarithmic scale, where the uncertainties are of order 10% the measured luminosity.

(Herbig, 1956; Linsky et al., 1995; Reid et al., 1999; Fleming et al., 2000). These observed flares showed that UCDs were capable of generating at least transient magnetic fields. At the time the α^2 dynamo had not been suggested for fully convective stars, leaving little explanation for the observed activity. There was speculation that temporally heated corona could be responsible for at least the X-ray flares (Reid et al., 1999), but no model was proposed to explain the magnetic activity.

The first detection of both flaring and quiescent radio emission from a brown dwarf quelled any doubt that UCDs are capable of generating and sustaining mag-

netic fields. In December of 1999, an X-ray flare was detected from the M9 brown dwarf LP 944-20 (Rutledge et al., 2000). This was followed by a July 2000 VLA detection of radio emission that exceeded the GBR by four orders of magnitude (Berger et al., 2001). The presence of both a quiescent and a flaring component showed that UCDs are capable of producing brief magnetic outbursts as well as sustaining strong magnetic fields. This groundbreaking discovery made by a team of summer students ignited a larger investigation into the radio activity of UCDs.

Subsequent radio surveys of UCDs were conducted in the 1–10 GHz frequency range, where emission is expected to peak for the inferred magnetic field strengths of UCDs (see section 1.5.6 for discussion). Between VLA and ATCA observations of hundreds of these objects conducted in the years since the initial detection of LP 944-20, roughly 10% of them have been detected with bright radio emission, while the non-detections have been given upper flux limits (Antonova et al., 2013; Route and Wolszczan, 2016; Lynch et al., 2016; Berger, 2006). This low, but non-zero, detection rate turned the paradigm of UCDs on its head; while these mysterious objects are capable of producing sustained magnetic activity, such activity (or at least the detection of it) is relatively rare. When the detected UCDs are plotted along the GBR, they form a separate branch, showing a departure from the relation that holds well for other stars and suggesting different magnetic behaviour at the bottom of the main sequence.

Despite the low numbers of radio-detected UCDs (fewer than forty to date), a few key trends in radio emission have emerged. The overall radio detection rate of 10% increases to nearly 50% for objects with $v \sin i > 20 \text{ km s}^{-1}$ (McLean et al., 2012), where v is the intrinsic stellar rotation speed and i is the inclination. This might suggest a correlation between the rotation period and likelihood of radio brightness, where the more rapid rotators are more likely to be radio emitting, especially because rapid rotators can have low $v \sin i$ but slow rotators cannot have high $v \sin i$. Photometry can give a precise measure of the rotation rate, but in the absence of such measurements $v \sin i$ can be determined spectroscopically, although there is a dependence on inclination i (Shajn and Struve, 1929), shown in Figure 1.6. This could indicate that the stellar inclination, rather than the rotation rate, is the relevant parameter. Whether the rotation rate or inclination plays a more pivotal role in the likelihood of UCD radio emission is an open question, and an

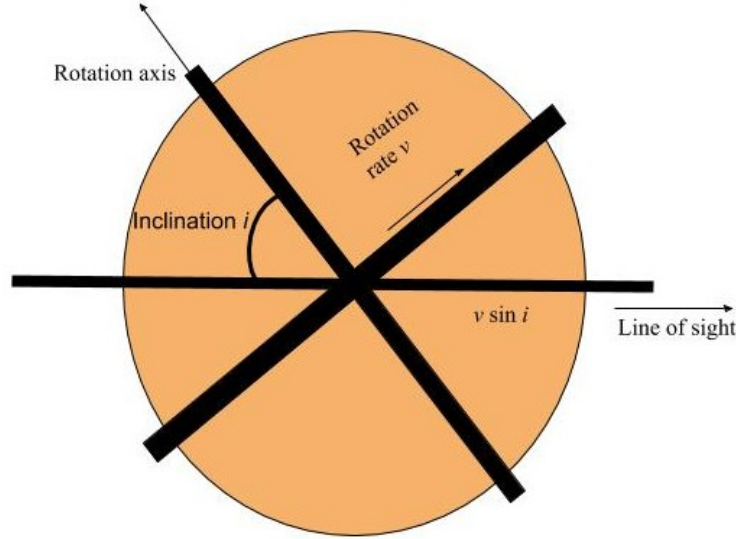


Figure 1.6: The role of inclination i in spectroscopic measurements, which measure the projected $v \sin i$ rather than the true equatorial rotation rate, v .

important part of building magnetic models of UCDs.

Another trend in the radio emission of UCDs is an anti-correlation between the X-ray luminosity normalised to the bolometric luminosity and the likelihood of radio brightness. UCDs with bright X-ray emission relative to their total luminosity across the electromagnetic spectrum tend to be radio quiet, while UCDs with dim X-ray emission tend to be radio bright (Williams et al., 2014; Cook et al., 2014). This reversal from the GBR could be due to coronal stripping from centrifugal forces (Jardine and Unruh, 1999), or it could be a product of UCD magnetic fields that are fundamentally different from the Sun’s magnetic field.

Emission at low radio frequencies (1 – 10 GHz) is generally attributed to the electron cyclotron maser instability, although gyrosynchrotron radiation was also raised as an explanation for quiescent radio emission (see section 1.5.6). Although there are a few ways to disentangle emission due to these two mechanisms from low radio frequency observations alone, observations at high radio frequencies at which emission due to the electron cyclotron maser instability becomes unphysical can

discriminate between the two mechanisms. In the $\sim 50 - 100$ GHz range, optically thin gyrosynchrotron radiation is expected to dominate for typical UCD magnetic field strengths.

Prior to this work, only one UCD had been detected within that frequency range. The M9.5 star TVLM 513-46546 was found with emission throughout the 1–100 GHz range, and a spectral index consistent with optically thin gyrosynchrotron radiation (Williams et al., 2015). The detection of this star at such high frequencies confirmed the presence of gyrosynchrotron radiation from UCDs, and challenged existing magnetic models of UCDs developed to account for the electron cyclotron maser instability.

1.5 Radio Emission from Stars

Attempts to measure the radio emission of astronomical objects began in the late 1800s with observations of the Sun (Haddock, 1984). Physicist Oliver Lodge hypothesised that the Sun must be active at radio frequencies, but due to the technological limitations of the instruments available to him at the time, was unable to make a detection. Lodge’s attempted Solar radio observations are described in Débarbat et al. (2007),

I [hoped] to try for long-wave radiation from the Sun, filtering out the ordinary well-known waves by a blackboard or other sufficiently opaque substance. I did not succeed in this, for a sensitive coherer in an outside shed unprotected by the thick walls of a substantial building cannot be kept quiet for long. I found its spot of light liable to frequent weak and occasionally violent excursions, and I could not trace any of these to the influence of the Sun. There were evidently too many terrestrial sources of disturbance in a city like Liverpool to make the experiment feasible. I don’t know that it might not possibly be successful in some isolated country place; but clearly the arrangement must be highly sensitive in order to succeed.

The first detection of radio emission from space was made nearly 40 years later by Karl G. Jansky at Bell Laboratories. While working on transatlantic voice

transmissions with a movable antenna, Jansky found that the antenna consistently picked up a directional signal that repeated on roughly 24-hour intervals. This initially made Jansky think the emission was coming from the Sun, but subsequent observations determined that its period was actually 23 hours and 56 minutes - the length of a sidereal day. Jansky determined the radio emission instead came from the Sagittarius constellation. He attributed the signal to interstellar gas and dust, and erroneously concluded that the Sun and stars could not produce significant radio emission. In subsequent years, Sagittarius A, one of the brightest radio sources in the sky, has been determined to be a supermassive black hole by 2020 Nobel Prize winners Reinhard Genzel and Andrea Ghez. Karl Jansky's legacy as the father of radio astronomy lives on in the naming of the Karl G. Jansky Very Large Array and the Jansky unit of radio flux density ($10^{-26} \text{ W m}^{-2} \text{ Hz}^{-1}$).

Radio emission from stars was not discovered until the following decade by physicist John Hey and engineer George Southworth. Hey determined that radar interference was coming from the Sun, and the presence of many sunspots on its surface indicated that the interference was associated with Solar activity. Southworth subsequently measured the centimetre wavelength emission of the Sun, which was published at the end of World War II (Southworth, 1982; Hey, 1946). These early discoveries showed that radio emission could come from both strong galactic sources as well as from the Sun and stars, launching the field of radio astronomy.

1.5.1 Definitions, Units, and Radiative Transfer

Before providing an overview of the relevant emission mechanisms for UCDs, it is helpful to briefly define common terms used in radio astronomy and summarize relevant areas of radiative transfer. The below description follows Chapter 2 of Condon and Ransom (2016) and the introduction provided in Dulk (1985).

Light traveling from distant sources to observatories on Earth is subject to various absorption, emission, and scattering processes. Additionally, the distance and observing angle impact the amount of emitted radiation actually arriving at the observer.

The intrinsic brightness, or intensity, is defined as the outgoing radiation from the source itself, independent of observation. In radio astronomy it is common

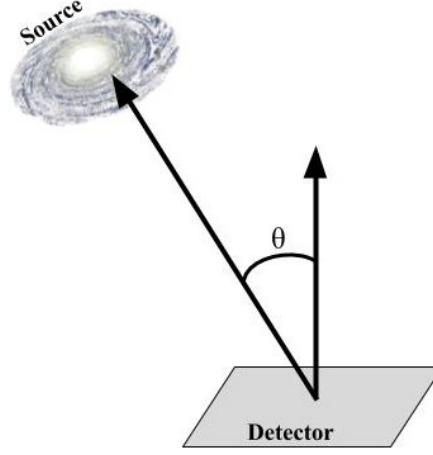


Figure 1.7: An emitting source oriented at angle θ relative to a detector, where the incoming flux at frequency ν is measured.

to use the specific intensity I_ν , or intensity per unit frequency to measure the brightness. The specific intensity reveals how bright a source is at the frequency of observation in the range ν to $\nu + d\nu$.

An amount of outgoing energy dE between frequencies ν and $\nu + d\nu$ arriving in time interval dt is given by the specific intensity I_ν of a source of solid angle $d\Omega$ and projected area $\cos \theta d\sigma$ (Figure 1.7), where σ is the area of the source, is,

$$dE = I_\nu \cos \theta d\sigma d\Omega dt d\nu. \quad (1.14)$$

The power emitted between frequencies ν and $\nu + d\nu$, $dP = dE/dt$ can then be used with Equation 1.14 to define the specific intensity,

$$I_\nu \equiv \frac{dP}{(\cos \theta d\sigma) d\nu d\Omega}, \quad (1.15)$$

which has MKS units of $\text{W m}^{-2} \text{Hz}^{-1} \text{sr}^{-1}$ and CGS units of $\text{erg cm}^{-2} \text{s}^{-1} \text{Hz}^{-1} \text{sr}^{-1}$. The total intensity I can be found by integrating over all frequencies and is defined as $I \equiv \int_0^\infty I_\nu(\nu) d\nu$.

The amount of outgoing radiation from the source arriving at the detector at

observing frequency ν is defined as the flux density S_ν . Flux density can be found by integrating the specific intensity over the solid angle Ω subtended by the source,

$$S_\nu \equiv \int I_\nu(\theta, \phi) \cos \theta d\Omega. \quad (1.16)$$

In this work, all observed targets are “point sources”, meaning that their physical extent is negligible compared to the telescope resolution, and thus can be treated as if they are emitting from a single localised point. In this case, $\cos \theta \approx 1$, and the flux density is reduced to $S_\nu \approx \int I_\nu(\theta, \phi) d\Omega$.

Flux density is usually expressed in units of Janskies (abbreviated Jy), as MKS and CGS units are both too large for typical flux density values. The conversion of Janskies to other units is $1 \text{ Jy} = 10^{-23} \text{ erg s}^{-1} \text{ cm}^{-2} \text{ Hz}^{-1} = 10^{-26} \text{ W m}^{-2} \text{ Hz}^{-1}$.

Radiation is subject to both absorption and emission effects as it travels from a source to the detector where it is measured as a flux value. Some photons will be absorbed in the interstellar medium (ISM), while additional photons emitted by the ISM will join the incoming radiation. These effects are expressed in terms of the absorption and emission coefficients, κ_a and j_ν , respectively. A fraction dI_ν of the total specific intensity I_ν will be absorbed over a small length ds ,

$$\frac{dI_\nu}{I_\nu} = -\kappa_a ds, \quad (1.17)$$

while the amount of radiation emitted at frequency ν along distance ds is,

$$j_\nu \equiv \frac{dI_\nu}{ds}. \quad (1.18)$$

An equation of radiative transfer can now be expressed by combining the effects of both the absorption and emission along the line of sight,

$$\frac{dI_\nu}{ds} = -\kappa_a I_\nu + j_\nu. \quad (1.19)$$

In the case of blackbody radiation $B_\nu(T)$ for a perfect absorber in local thermal equilibrium, $I_\nu = B_\nu(T)$, and $j_\nu/\kappa_a = B_\nu(T)$ - an expression known as Kirchhoff's Law.

Following the Rayleigh-Jeans Law, applicable at low frequencies determined

by $h\nu \ll k_B T$ where k_B is the Boltzmann constant,

$$B_\nu(T) \approx \frac{2\nu^2 k_B T}{c^2}. \quad (1.20)$$

This relation enables astronomers to define the brightness temperature, T_b . This is the temperature a source with specific intensity I_ν would have if it emitted as a blackbody. Re-arranging Equation 1.20, the brightness temperature can be expressed,

$$T_b \equiv \frac{I_\nu c^2}{2k_B \nu^2}. \quad (1.21)$$

It is important to note that the brightness temperature is often different from the effective temperature. This temperature, T_{eff} , is representative of the kinetic temperature of the emitting electrons. The two are equivalent in the case of perfect thermal emission only or in the case of an optically thick source (optical thickness discussed in Section 1.5.5). The brightness temperature is therefore very useful in radio astronomy for distinguishing between the kind of emission mechanism involved.

Radio emission has now been detected from stars of all spectral types, including ultracool dwarfs, and can be broadly categorized as thermal or nonthermal. A star's thermal emission is directly related to the temperature of the emitting region. Stars that emit thermal radio emission are radio bright, but have comparatively low total energy emitted in radio. Large emitting regions are required to produce detectable radio thermal emission. Thermal emission follows Planck's Law and produces a blackbody spectrum when optically thick.

Conversely, nonthermal emission mechanisms such as most synchrotron and gyrosynchrotron radiation do not necessarily depend on the local temperature, and nonthermal sources can have brightness temperatures in excess of 10^{12} K. Nonthermal processes involve highly energetic particles, and do not require the same large emitting region as thermal processes. Thus, high brightness temperatures can be used as a diagnostic for whether the underlying emission process is thermal or nonthermal.

Both thermal and nonthermal mechanisms can produce stellar radio emission, including bremsstrahlung (free-free emission), plasma emission, the electron cy-

clotron maser, gyrosynchrotron, and synchrotron radiation. In this section I provide an overview of each of these mechanisms, and a description of the expected radiation from each one.

1.5.2 Bremsstrahlung Emission

The term “bremsstrahlung” derives from the German word for “braking radiation”, developed to describe the phenomenon of electrons “braking” when incident on a metal target. The phenomenon itself occurs when a free electron’s trajectory is curved by the electric field as it passes by a charged particle, losing part or all of its kinetic energy in the form of a photon in the process. The most common incidence of bremsstrahlung radiation in astrophysical contexts is emission from compact regions with large quantities of ionised hydrogen, but bremsstrahlung radiation is also produced in stellar atmospheres (Culhane, 1969). Because bremsstrahlung radiation is produced by free electrons with a range of starting energies, it emits continuously across the electromagnetic spectrum, at frequencies determined by the amount of kinetic energy lost during the interaction between the electron and the ion.

Following Condon and Ransom (2016), the power emitted by an electron of charge q and acceleration \dot{v} is given by the non-relativistic Larmor formula for the instantaneous power of an accelerated charge,

$$P = \frac{2q^2\dot{v}^2}{3c^3} \text{ (cgs units).} \quad (1.22)$$

The relativistic Larmor formula includes an additional factor, relevant for relativistically moving electrons, but not used here. The total energy emitted by a single electron during this interaction is,

$$P_{\text{tot}} = \frac{\pi Z^2 e^6}{4c^3 m_e^2} \frac{1}{b^3 v}, \quad (1.23)$$

where Z is the atomic number, e is the elementary charge, and b is the impact parameter.

Most astronomical sources of bremsstrahlung radiation are thermal, and thus

the radiating electrons follow a Maxwellian velocity distribution,

$$f(v) = 4\pi v^2 \left(\frac{m}{2kT} \right)^{3/2} e^{-\frac{1}{2}m_e v^2/kT}, \quad (1.24)$$

where particles have velocity $v \ll c$, m_e is the electron mass, k is the Boltzmann constant, and T is the temperature. For a distribution of electrons passing by charged particles, the impact parameter b can range between b_{\min} and b_{\max} , the total frequency-dependent emissivity, or energy per unit volume at frequency ν , is,

$$j_\nu = \frac{\pi^2 Z^2 e^6 N_e N_i}{4c^3 m_e^3} \sqrt{\frac{2m_e}{\pi kT}} \ln\left(\frac{b_{\max}}{b_{\min}}\right), \quad (1.25)$$

where N_e and N_i are the number densities of electrons and ions, respectively.

The total emissivity is this value integrated over the electron velocities. Since b_{\min} and b_{\max} are only included in a logarithm, they can be estimated approximately by considering momentum transfer and electromagnetic effects. The value of $\ln(b_{\max}/b_{\min})$ works out to approximately 10. The total emissivity is then,

$$j(\nu, T) = \frac{2^5 \pi e^6}{3m_e c^3} \sqrt{\frac{2\pi}{3km_e}} T^{-1/2} e^{-h\nu/kT} N_e N_i Z^2 g_{ff}(\nu, T) \quad (1.26)$$

in units of $\text{erg s}^{-1} \text{ cm}^{-3} \text{ Hz}^{-1}$, where g_{ff} is the gaunt factor, $\frac{\sqrt{3}}{\pi} \ln(b_{\max}/b_{\min})$.

Thermal bremsstrahlung accounts for much of the radio emission from astrophysical objects including star-forming HII regions and galaxies (Duric et al., 1988). While bremsstrahlung radiation from UCDs does emit at radio frequencies, the contribution is far below the detection limit of radio telescopes, on the order of nanoJanskies. Radio emission from UCDs implies brightness temperatures of order 10^{12} K using Equation 1.21, ruling out any thermal process as the source. Non-thermal, relativistic bremsstrahlung is also present in UCDs, however, producing detectable X-ray emission (Berger et al., 2008a).

1.5.3 Plasma Emission

Unlike bremsstrahlung radiation, where electrons act independently of one another to produce radiation across the electromagnetic spectrum, electrons in coherent

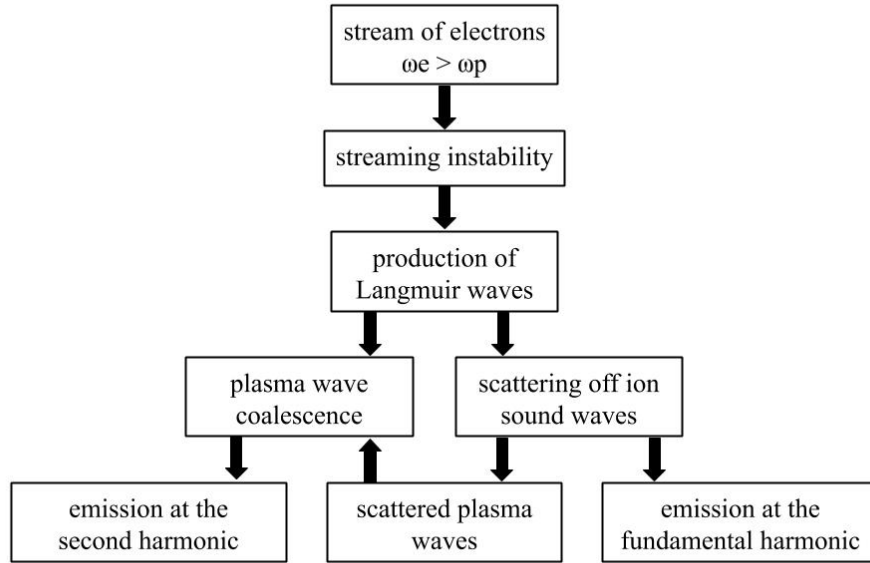


Figure 1.8: The steps involved in plasma emission, resulting in radiation at the fundamental and second harmonic of the plasma frequency. Reproduced from Melrose (1991).

processes such as plasma emission act together, producing emission in narrow frequency bands. The strength of emission is not directly related to the temperature of the emitting source, indicating nonthermal emission. Plasma emission occurs when a stream of electrons stimulate oscillations in the stellar plasma, releasing radio emission corresponding to the frequency of oscillations. The conditions for plasma emission are met when perturbing electrons are oscillating in a magnetic field with frequency greater than the plasma frequency, the timescale for plasma to return to a charge neutral state after a displacement in the charge. This occurs through a process first described by Ginzburg and Zhelezniakov (1958).

An initial beam of electrons spiraling along a magnetic field line with angular frequency ω_e reaches a streaming instability, where higher velocity electrons at the front of the beam outpace the slower electrons in the back, leading to an uneven

velocity distribution with a positive gradient. It is produced by electrons reaching >10 keV ($T > 10^8$ K) energies forming a “bump” of higher velocity electrons at the “tail” end of the velocity distribution (Figure 1.9). This velocity bump is formed by electrons streamed along magnetic field lines or by depletion of slow-moving electrons through collisions in the plasma. If the fast-moving electrons have an angular velocity greater than the natural frequency of the plasma, $\omega_e > \omega_p$, then there is a net positive transfer of free energy from the electrons to the plasma (Drummond et al., 1970). This leads to exponential amplification of energy transfer and the production of plasma oscillations known as Langmuir waves. There are a few paths by which the plasma waves can release energy through radio emission, including wave-ion and wave-wave interactions. A Langmuir wave of frequency ω_L can scatter off ion sound waves of frequency ω_i , producing emission at the fundamental plasma frequency with $\omega_p = \omega_i + \omega_L$, or additional scattered Langmuir waves of ω_L . Two plasma waves can collide and coalesce to produce emission at the second harmonic of the plasma frequency, $\omega_L + \omega_L = 2\omega_p$. This process is shown in Figure 1.8.

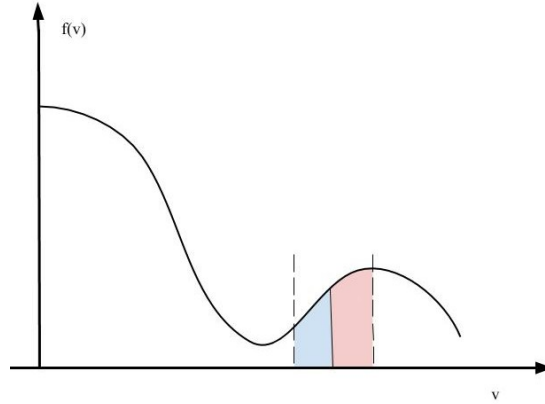


Figure 1.9: The bump-in-the-tail distribution of electron velocities, where there is a greater number of higher velocity electrons (red shaded region) than lower velocity electrons (blue shaded region).

Plasma emission for astrophysical application was initially developed to describe the observed properties of Solar radio bursts (Ginzburg and Zhelezniakov, 1958). The plasma frequency in the active Solar region is ~ 300 MHz, although damping can cause the escaping radiation to be reduced to lower frequencies. It is often seen in Type II and III radio bursts, which are characterised by drifting radio emission at the fundamental and second harmonic of the plasma frequency, often associated with Solar flares (Zlotnik et al., 1998; Reid and Ratcliffe, 2014). Observations of Type III bursts show an angular dependence on the outgoing radiation, consistent with the radiation patterns expected for plasma emission (Thejappa and MacDowall, 2015).

Although plasma emission is commonplace in Solar radio bursts, its effectivity is limited. As in the Sun, plasma emission from UCDs is likely constrained to ~ 100 MHz frequencies because of the dependence on high electron densities and because emission at higher radio frequencies gets damped by free-free absorption. High thermal coronal temperatures in UCD atmospheres may be able to circumvent this to a degree, as suggested by Burgasser and Putman (2005), possibly enabling GHz frequency plasma emission in very active stars such as AD Leo. However, this speculation is not supported by X-ray observations of such active UCDs; for example, a Chandra non-detection of the radio bright UCD LSR J1835 shows that the stellar corona did not reach the necessary temperatures to produce plasma emission in the GHz range (Hallinan et al., 2008; Berger et al., 2008b). While bursting, coherent emission is seen at GHz frequencies from some UCDs (discussed later), the more likely explanation for that emission is the electron cyclotron maser instability.

1.5.4 The Electron Cyclotron Maser Instability

The electron cyclotron maser instability is a nonthermal process by which energetic electrons in a low-density plasma cannot release energy via plasma radiation, so instead lose energy through direct emission. Like plasma emission, it is a coherent process; meaning that electrons release emission in a narrow frequency band. The earliest theories of the electron cyclotron maser instability were developed in the late 1950's (Twiss, 1958; Ginzburg and Zhelezniakov, 1958; Schneider, 1959),

and showed that interactions between energetic electrons and plasma waves at the cyclotron frequencies and its lower resonant frequencies could amplify the electromagnetic plasma waves, leading to negative absorption at the cyclotron frequency. The phenomenon itself is perhaps unfortunately named - maser is an acronym for *microwave amplification by stimulated emission of radiation*, essentially a radio wavelength laser. However, the electron cyclotron maser does not involve quantum effects or the stimulated jumping of electrons to lower energy levels. Instead, energy is released in the form of radio emission if thermal release through heating or particle acceleration fail. In the presence of a strong magnetic field, this occurs when the plasma frequencies are all significantly below the cyclotron frequency $\omega_c = qB/2\pi m_e$, or angular frequency of a charged particle such as an electron moving in a magnetic field. Additionally, the term “cyclotron” implies that the electrons involved are non-relativistic, but in practice the electrons in ECMI can be weakly relativistic, with $\gamma \approx 1.02$ (Chu, 2004).

The electron cyclotron maser instability (ECMI) produces emission near the cyclotron frequency ω_c and its harmonics $s\omega_c$, although the strength of emission rapidly decreases with increasing values of s . For typical UCD magnetic field strengths, strong ECMI emission is in the 1 – 10 GHz frequency range, but for Solar System planets where the phenomenon is observed, weaker magnetic fields bring emission down to ~ 100 kHz. There are two primary models of ECMI emission from stars and planets: a loss-cone driven model and a horseshoe model, both describing the distribution of precipitating electrons on the plasma. In both models ECMI is expected to produce coherent, highly circularly polarised, pulsed emission.

The loss-cone instability model relies on a population of electrons with the distribution,

$$f(p_{\perp}, p_{\parallel}) = A(p_{\perp})^{2j} e^{-p^2/(\Delta p)^2}, \quad (1.27)$$

where p is the momentum, and the subscripts \perp and \parallel denote the components perpendicular and parallel to the magnetic field, respectively, A is a constant, j is the loss-cone index describing the distribution of angles at which the precipitating electrons are absorbed into the stellar or planetary atmosphere, and Δp is the momentum dispersion (Treumann, 2006). The defining feature of the loss-cone distribution is the absence of electrons at low pitch angles, or angle between the

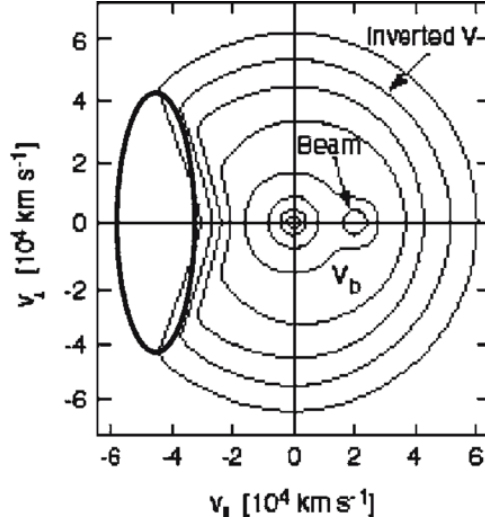


Figure 1.10: Distribution of electron velocities by parallel component $v_{||}$ (x-axis) and perpendicular component v_{\perp} (y-axis). The “inverted V” represents a region of population inversion in v_{\perp} , where a greater number of electrons have higher perpendicular velocity than have lower perpendicular velocity. “Beam” refers to the precipitating electron beam incident on the UCD atmosphere, while v_b refers to the initial beam velocity. The triangular conical shape represents the loss cone, where electrons with velocities approximately parallel to the magnetic field are lost to the stellar atmospheres. Used with permission from Treumann (2006).

particle’s velocity vector and the magnetic field. It requires high temperatures for emission to dominate absorption and cyclotron frequencies related to the plasma frequency by $\omega_c \approx 1.25-5 \omega_p$. This loss-cone anisotropy can be produced in certain situations where a propagating beam of electrons of velocities v_b are incident on a stellar or planetary atmosphere, where electrons with low pitch angles are absorbed by the atmosphere under the condition that $\alpha^* > \arcsin \sqrt{B_t/B_f}$, where α^* is defined as the critical pitch angle, B_t and B_f are the magnetic field strength at the top and the footpoints of the precipitating electron flux tube, respectively. Electrons with pitch angle α greater than α^* are reflected upward into the converging magnetic field due to the magnetic mirror effect. The magnetic mirror effect occurs when charged particles, in this case electrons, become trapped and reflected when traveling from

regions of low to high magnetic field strengths. An idealised loss-cone velocity distribution is shown in Figure 1.10. Emission from a loss-cone distribution occurs when energetic electrons are moved to a point of lower energy by a wave, and the electrons impart energy to the wave. This occurs when a resonance is met between the electromagnetic waves and electrons spiraling with angular cyclotron frequency ω_c in a magnetic field ($\omega - s\omega_c/\gamma - k_{||}v_{||} = 0$), where ω is the angular frequency of wave, $k_{||}$ is the parallel component of the wavenumber and $v_{||}$ is the parallel component of the resonant electron velocity. By depleting electrons at low pitch angles, the loss-cone distribution creates an anisotropy where there are more energetic electrons than ground-state electrons, enabling the electrons to transfer energy to the wave under the resonant condition. Conversely, the condition for absorption is met when the energy of the wave is greater than that of the electrons, and electrons will absorb some energy from the wave. The resonant condition forms an ellipse when plotted in $p_{\perp}p_{||}$ -space, where the line integral around the ellipse is the absorption coefficient.

For mildly relativistic electrons ($E < 500$ keV), the growth rate of electromagnetic modes for a given electron momentum distribution $f(\vec{p})$ is determined by numerically integrating $\partial f / \partial p$ over the ellipse defined by the resonance condition,

$$\Gamma_s^\sigma(\vec{k}) = \int A_s^\theta(\vec{p}, \vec{k}) \delta(\omega - s\Omega_c/\gamma - k_{||}v_{||}) \left(\frac{s\Omega_c}{\gamma v_{\perp}} \frac{\partial}{\partial p_{\perp}} + k_{||} \frac{\partial}{\partial p_{||}} \right) f(\vec{p}) d^3\vec{p}, \quad (1.28)$$

where k is the wavenumber, ω is the wave frequency, \vec{p} is the electron momentum, Ω_c is the cyclotron frequency, s denotes the harmonic, $f(\vec{p})$ is the electron distribution, and δ is the Kronecker delta function (Melrose et al., 1980). The prefactor $A_s^\theta(\vec{p}, \vec{k})$ comes from approximated Bessel functions and takes the form,

$$A_s^\theta(\vec{p}, \vec{k}) \approx \frac{4\pi^2 e^2 c^2 \beta^2 \sin^2 \theta}{(1 + T_\sigma)^2} \frac{s^{2s}}{2^{2s} (s!)^2} (\beta \sin \theta)^{2s-2} (1 + |\cos \theta| T_\sigma)^2, \quad (1.29)$$

where σ is the mode, T_σ is the axial ratio of polarisation for mode σ , $\beta = v/c$ (Melrose et al., 1980; Dulk, 1985), and θ is the observing angle. The wave mode σ can take on values of $\sigma = 1$ for the ordinary (O) mode or $\sigma = -1$ for the extraordinary (X) mode, describing the direction of polarisation with respect to the magnetic field. Emission occurs when the net positive contribution to the

wave growth is greater than the net negative contribution. Since $k_{||} \ll \omega/c$ and $\omega \approx s\Omega_c$ in the semirelativistic approximation, the $\partial f(\vec{p})/\partial p_{\perp}$ term in Equation 1.28 is larger than the $\partial f(\vec{p})/\partial p_{||}$ term. Growth of the wave then requires that $\partial f(\vec{p})/\partial p_{\perp} > 0$, which is satisfied by the loss-cone distribution as electrons with low v_{\perp} are absorbed into the atmosphere.

The largest contributor to wave growth is the derivative term in Eqn. 1.28; amplification primarily occurs due to electrons escaping from within the loss cone, at frequencies $\approx s\omega_c$. Most emission will be at the $s = 1$ harmonic, as at higher harmonics emission is throttled both by strong absorption and lower growth rates.

The earliest models of ECMI relied on the loss-cone distribution to power the instability. However, even accounting for effects such as relativistic corrections (Wu and Lee, 1979), the loss-cone model still suffered from low growth rates and broader emission, inconsistent with the intense, very narrow emission features that were observed from the Earth's auroral kilometric radiation (Gurnett and Anderson, 1981). Particle simulations based on the loss-cone distribution found it both inefficient and incapable of producing the in situ measured strengths of auroral kilometric radiation (Pritchett, 1986). These issues were resolved by considering a ring-shell (horseshoe) distribution of electrons.

The horseshoe model focuses on the large drifting motions of electrons themselves in the global stellar magnetic field, combining a shell distribution with the loss-cone distribution. Following Treumann (2006) the horseshoe distribution, produced by electrons in a dipolar magnetic field that are accelerated by a parallel electric field, is

$$f(p_{\perp}, p_{||}) = \frac{1}{2\pi p_{\perp}} \delta(p_{\perp}^2 + p_{||}^2 - p_s^2), \quad (1.30)$$

where p_s is the three-dimensional shell momentum. This shell distribution is less stable than the loss-cone distribution, leading to a higher intensity and growth rate that match observations of Solar System auroral emission (Ergun et al., 2000). In the case of planets and UCDs, a horseshoe shape arises from the influence of a global magnetic field. A strong dipolar magnetic field that is weakest at the equator of the star and strongest at the poles will cause electrons to bounce back and forth between the strongest points around either pole. Electrons are accelerated by the parallel component of the electric field at the poles - generated by the electric potential

gradient between magnetosphere and upper atmosphere, $\mathcal{E}_{||}$, increasing the parallel component of the electron's velocity $v_{||}$ as they move towards areas of increasing magnetic field strength. Conservation of magnetic moment $\mu = m_e v_{\perp}^2 / 2B$ enables some of the energy gained by the electrons in the acceleration to be transferred from the parallel component $v_{||}$ to the perpendicular component of the velocity v_{\perp} . The horseshoe distribution emerges when magnetic mirroring causes some electrons to get deflected or absorbed into the atmosphere while others are reflected upward, where the upward directed electrons are confined to a narrow range of speeds. In this model, the acceleration of electrons by the parallel component of the electric field is what stimulates emission (Melrose and Wheatland, 2016).

While the electron cyclotron maser was initially conceived in astrophysical contexts to explain the auroral radiation observed in Solar System planets, some radio detections of UCDs have all the hallmarks of ECMI. The viewing angle dependence in the growth rate prefactor, Equation 1.29, shows that emission is highly beamed at angles nearly perpendicular to the magnetic field (Treumann, 2006; Dulk, 1985), causing ECMI to be rotationally modulated with the same periodicity as the star. The growth rate is also strongly dependent on the wave mode σ , with emission being largest in the X-mode, resulting in strongly circularised emission. Thus, pulsed, highly circularly polarised emission from UCDs near the cyclotron frequency of the relevant electron population, 1-10 GHz for typical UCD magnetic field strengths, is generally attributed to the ECMI (Hallinan et al., 2008). The theoretical basis for UCD ECMI emission relies on the generation of an axisymmetric dipolar magnetic field that is co-aligned with the UCD spin axis, and a weakly ionised atmosphere. A mostly dipolar field configuration is thought to be necessary for coupling between the ionosphere and magnetosphere, generating the “engine” for auroral ECMI (Pineda et al., 2017). Auroral electron precipitation provides a population of mildly relativistic electrons that increase the intensity of auroral currents (Rycroft et al., 2008). The ECMI emission is strongly beamed (i.e., Zarka, 2004), and radio emission from ECMI will peak as the beam rotates into view, producing pulsed emission coincident with the stellar rotation. Since it is produced near the poles, ECMI emission from UCDs is expected to depend on the inclination as well, with higher inclinations meaning more beamed emission is visible (Nichols et al., 2012).

1.5.5 Synchrotron Radiation

The most common source of nonthermal emission in astrophysical applications is synchrotron radiation, accounting for most of the radio emission from active galactic nuclei and star-forming regions as well as optical emission from nebulae and quasars (e.g., La Mura et al., 2017; Wills et al., 1992; Klein et al., 2018; Burbidge, 1957). Synchrotron radiation is electromagnetic emission released by high-energy particles accelerated along a curved path; in astrophysical contexts, this is ultrarelativistic electrons, with energies $\gg m_e c^2$, spiraling in a magnetic field.

Following Longair (2011), the loss rate of energy dE/dt in the rest frame of a single electron gyrating in a magnetic field is given by,

$$\frac{dE}{dt} = -\frac{\gamma^4 q^2}{6\pi\epsilon_0 c^3} \dot{v}^2, \quad (1.31)$$

where the acceleration of the electron \dot{v} is always perpendicular to the velocity of the particle and the magnetic field. The acceleration of an electron is found using the force on the electron in the presence of a magnetic field \vec{B} and an electric field \vec{E} , $\vec{F} = q(\vec{E} + \vec{v} \times \vec{B}) = q\vec{E}$ in the rest frame of the electron, where $\vec{E} = \vec{v} \gamma B \sin \theta$, giving acceleration $\vec{v} = q\gamma v \vec{B} \sin \theta / m_e$. Combining this and the Thompson cross-section σ_T ,

$$-\frac{dE}{dt} = 2\sigma_T c \gamma^2 U_{\text{mag}} \left(\frac{v}{c}\right)^2 \sin^2 \theta, \quad (1.32)$$

where $\sigma_T = (8\pi/3)(q^2/(4\pi\epsilon_0 m_e c^2))^2$, the energy density of the magnetic field $U_{\text{mag}} = B^2/2\mu_0$, and θ is the pitch angle. Transforming from the electron's rest frame to the lab frame, considering the ultra-relativistic limit $v \rightarrow c$, and averaging over solid angle gives the simplified expression,

$$-\frac{dE}{dt} = \frac{4}{3} \sigma_T c \gamma^2 U_{\text{mag}}. \quad (1.33)$$

Unlike plasma and ECMI emission, most synchrotron radiation is incoherent, although pulsars do emit coherent synchrotron radiation (e.g., Contopoulos, 2009). Synchrotron emission reaches a maximum at frequency of $\nu_{\text{max}} = 0.29\nu_c$, where ν_c is the cyclotron frequency. The emission frequency of an individual electron is approximated by $\nu = \gamma^2 \nu_c$, where $\gamma = E/m_e c^2$.

In the case of a power-law distribution of electrons, where the number distribution of electrons is $N(E) \propto E^{-\delta}$, the spectral emissivity - or total emission per solid angle - in the range E to $E + dE$ radiated in the frequency range ν to $\nu + d\nu$ is given by,

$$j_\nu = -\frac{dE}{dt} N(E) dE. \quad (1.34)$$

Using the relations $E = \gamma m_e c^2 = \sqrt{\nu/\nu_c} m_e c^2$, $dE = m_e c^2 / (2\sqrt{\nu_c \nu}) d\nu$, and $-dE/dt = 4/3 \sigma_T c [EB/(m_e c^2) \sqrt{2\mu_0}]^2$, the specific intensity I_ν due to synchrotron radiation from a source of volume V and magnetic field strength B is,

$$I_\nu = 1.7 \times 10^{-21} \frac{2\sigma_T c}{3\mu_0(m_e c^2)^{\delta-1}} \left(\frac{q}{2\pi m_e} \right)^{(\delta+1)/2} \frac{VB^{(\delta+1)/2}}{\text{Gauss}} \times \left(\frac{6.26 \times 10^{18}}{\nu} \right)^{(\delta-1)/2} \text{erg s}^{-1} \text{Hz}^{-1} \text{cm}^{-2} \text{sr}^{-1}. \quad (1.35)$$

The electron energy index δ is thus related to the spectral index of the synchrotron emission α by $\alpha = (\delta - 1)/2$.

The spectrum is subdivided into optically thick and thin portions according to the wavelength of light; the optical thickness determines the ability of radiation to escape from a medium without being absorbed. Optical depth is defined as,

$$\tau(\nu) = \int_0^s \kappa(\nu) \rho ds, \quad (1.36)$$

where $\kappa(\nu)$ is the opacity of the medium at frequency ν - in this case, the stellar atmosphere - ρ is the density, and ds is an incremental distance along the line of sight for a total distance s . Note that $\kappa(\nu)$ is related to the absorption coefficient κ by The opacity inhibits the outgoing specific intensity by,

$$I_\nu = I'_\nu e^{-\tau(\nu)}, \quad (1.37)$$

where I'_ν is the stellar intensity unimpeded by propagation through an absorbing medium.

Emission at frequencies below the cyclotron frequency is in the optically thick

portion of the spectrum, where $\tau(\nu) > 1$, and synchrotron self-absorption occurs for all electron energy distributions. When optically thick, the specific intensity is rising with a spectral index of $\alpha = 5/2$. In contrast, in the optically thin portion of the spectrum the characteristic synchrotron electron energy indices of $2 \leq \delta \leq 5$, the corresponding spectral index range is $-0.5 \geq \alpha \geq -2$.

Although stars are not commonly discussed as sources of synchrotron radiation, it has been observed in some stellar emission, including from the Sun (Kruse et al., 1956). The terms synchrotron and gyrosynchrotron - the latter referring to a mildly relativistic version of synchrotron radiation - are sometimes used interchangeably in the literature on UCD radio emission (e.g., MacGregor et al., 2020; Williams et al., 2015), but gyrosynchrotron emission (discussed in the following section) is the more likely mechanism for quasi-quietescent radio emission from UCDs. There are a few reasons for this; peak emission frequencies point towards only mildly relativistic electron energies, the high linear polarisation characteristic of synchrotron is not seen in observations, inferred spectral indices are more consistent with gyrosynchrotron values, and synchrotron radiation is often highly beamed and rotationally modulated (Berger, 2002; Osten et al., 2009). Additionally, Ramaty (1969) argues that the magnetic field and dense plasma conditions make it unlikely for electrons to reach ultrarelativistic energies in stellar environments. Nonetheless, synchrotron radiation may be a possible source of some radio emission from ultracool dwarfs, possibly originating in chaotic stellar winds where plasma density is significantly lower (White, 1985) or radiation belts as in the case of Jupiter (Girard et al., 2016; Hallinan et al., 2006).

1.5.6 Gyrosynchrotron Radiation

Gyrosynchrotron radiation can be seen as a special case of synchrotron radiation involving only mildly relativistic electrons, and is likely responsible for much of the radio emission during Solar flares, weak magnetic brightening, and coronal mass ejections (e.g., White and Kundu, 1992; Kundu et al., 2001; Gary and Hurford, 1987; Nindos, 2020). In the astrophysical contexts discussed in this work it is incoherent, nonthermal emission produced by mildly relativistic electrons spiraling along magnetic field lines. Thermal gyrosynchrotron, or gyroresonance, emission

is possible, but not considered in this work due to its low brightness temperatures, inconsistent with observations of UCDs. Unlike synchrotron radiation that requires ultrarelativistic electrons where $\gamma \gg 1$, gyrosynchrotron radiation is produced by electron populations that are only mildly relativistic, with $\gamma \sim 2$ -6. Both ECMI and gyrosynchrotron radiation peak near the cyclotron frequency, leading to some possible confusion between the two mechanisms in UCDs.

The theoretical framework for gyrosynchrotron radiation was developed in 1912 (Schott, 1912), but it was not until numerical calculations (Ramaty, 1969; Wild and Hill, 1971; Dulk and Marsh, 1982) and observations (Takakura and Scalise, 1970) performed in the second half of the century that full equations for gyrosynchrotron emission were developed. The expressions themselves are determined numerically and are not universally applicable, but hold well over the range of characteristic gyrosynchrotron electron energy indices $2 \leq \delta \leq 7$, viewing angles $\theta \geq 20^\circ$, and $\nu/\nu_c \geq 10$ (Dulk and Marsh, 1982).

Following the work of Dulk (1985), the number distribution of electrons per energy interval dE is given by,

$$n(E) = (\delta - 1)E_0^{\delta-1}NE^{-\delta}, \quad (1.38)$$

where δ is the electron energy index, E_0 is the low-energy cutoff (set at a low value of 10 keV for mildly relativistic electrons, although electrons below 100 keV contribute very little to the total energy), and N is the number of electrons per cm^3 . The electron energy index δ can be related to the spectral index α by $\alpha = 0.9\delta - 1.22$ (Dulk and Marsh, 1982), differing slightly from the relation for synchrotron radiation. For electron energy indices $2 \leq \delta \leq 7$, the corresponding spectral index range is $-0.58 \geq \alpha \geq -5.1$ in the optically thin portion relevant to this work.

Numerically evaluating the formulae presented in Takakura and Scalise (1970), Dulk and Marsh (1982) determined the following gyrosynchrotron relations,

$$\frac{\eta_\nu}{BN} \approx 3.3 \times 10^{-24} 10^{-0.52\delta} (\sin \theta)^{-0.43+0.065\delta} \left(\frac{\nu}{\nu_c} \right)^{1.22-0.90\delta}, \quad (1.39)$$

$$\frac{\kappa(\nu)B}{N} \approx 1.4 \times 10^{-9} 10^{-0.22\delta} (\sin \theta)^{-0.09+0.72\delta} \left(\frac{\nu}{\nu_c} \right)^{-1.30-0.98\delta}, \quad (1.40)$$

$$T_{\text{eff}} \approx 2.2 \times 10^9 10^{-0.31\delta} (\sin \theta)^{-0.36-0.06\delta} \left(\frac{\nu}{\nu_c} \right)^{0.50+0.085\delta}, \quad (1.41)$$

$$r_c \approx 1.26 \times 10^{0.036\delta} 10^{-0.071 \cos \theta} \left(\frac{\nu}{\nu_c} \right)^{-0.782+0.545 \cos \theta}, \quad (1.42)$$

$$\nu_{\text{peak}} \approx 2.72 \times 10^3 10^{0.27\delta} (\sin \theta)^{0.41+0.03\delta} (N L)^{0.32-0.03\delta} \times B^{0.68+0.03\delta}. \quad (1.43)$$

In the above relations, η_ν is measured in units of $\text{ergs cm}^{-3} \text{ s}^{-1} \text{ Hz}^{-1} \text{ sr}^{-1}$ and $\kappa(\nu)$ in units of cm^{-1} are the absorption and emission coefficients, respectively. T_{eff} is the nonthermal effective temperature or effective temperature of the radiating electrons measured in K, r_c is the degree of circular polarisation, ν_{peak} is the peak emission frequency measured in Hz, θ is the viewing angle between the magnetic field and the line of sight, B is the magnetic field in units of Gauss, and L is the effective path length, related to the optical depth $\tau(\nu)$ and $\kappa(\nu)$ by $\tau(\nu) = \kappa(\nu) L$. The gyrosynchrotron relations are represented graphically in Figure 1.11, for three values of the electron energy index $\delta = 3, 5, 7$.

While time variable pulsed and highly circularized emission from ultracool dwarfs is usually attributed to ECMI, many UCDs also show an incoherent quasi-quietescent radio component more characteristic of gyrosynchrotron radiation (Güdel, 2002; Osten et al., 2015). The strength of gyrosynchrotron radio emission from UCDs is dependent on the strength of the UCD magnetic field, the electron energy index δ , and the size of the emitting region. This is discussed in further detail in Chapters 3 and 4.

As detailed by Williams et al. (2014), gyrosynchrotron radiation could originate in frequent small-scale magnetic reconnection events. These events accelerate a population of downward-directed electrons confined to the magnetic field lines to near-relativistic energies, producing detectable radio emission, while also injecting highly energetic protons into the stellar environment (Figure 1.12). While the outgoing energetic particles cannot be detected directly, the gyrosynchrotron emission caused by the mildly relativistic electrons can be used as a tracer for such events (Hughes et al., 2019; Osten et al., 2016; Bastian et al., 1998). The

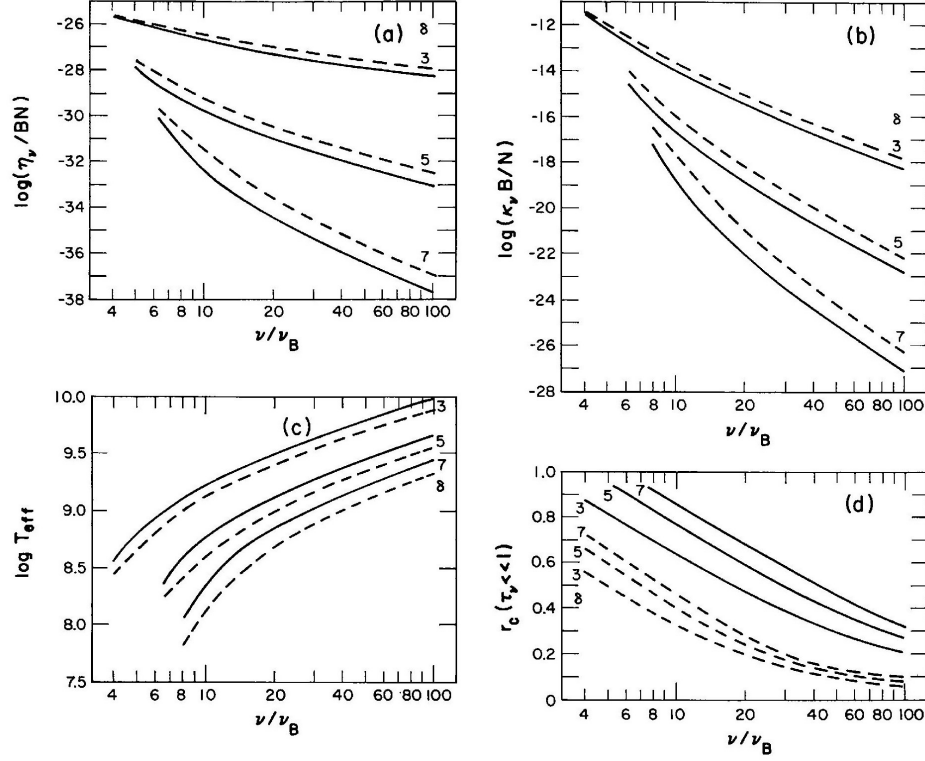


Figure 1.11: The gyrosynchrotron relations from Dulk and Marsh (1982), reproduced here with permission. Each curve shows δ values of 3, 5, & 7, with solid lines showing viewing angles of 80° and dashed lines showing viewing angles of 40° . The six plots represent (a) the emission coefficient, (b) absorption coefficient, (c) effective temperature, (d) degree of circular polarisation.

presence of energetic protons is particularly important when considering the impacts on surrounding planets. Several studies have shown that stellar UV emission alone may not be catastrophic for planets and could even be beneficial (Ranjan and Sassellov, 2016), but simulations ran by Segura et al. (2010) and Tilley et al. (2017) suggest that it is energetic particles, not UV emission alone, that is the most damaging to planetary atmospheres. The implications of gyrosynchrotron radiation on surrounding planets is discussed in detail in Chapter 5.

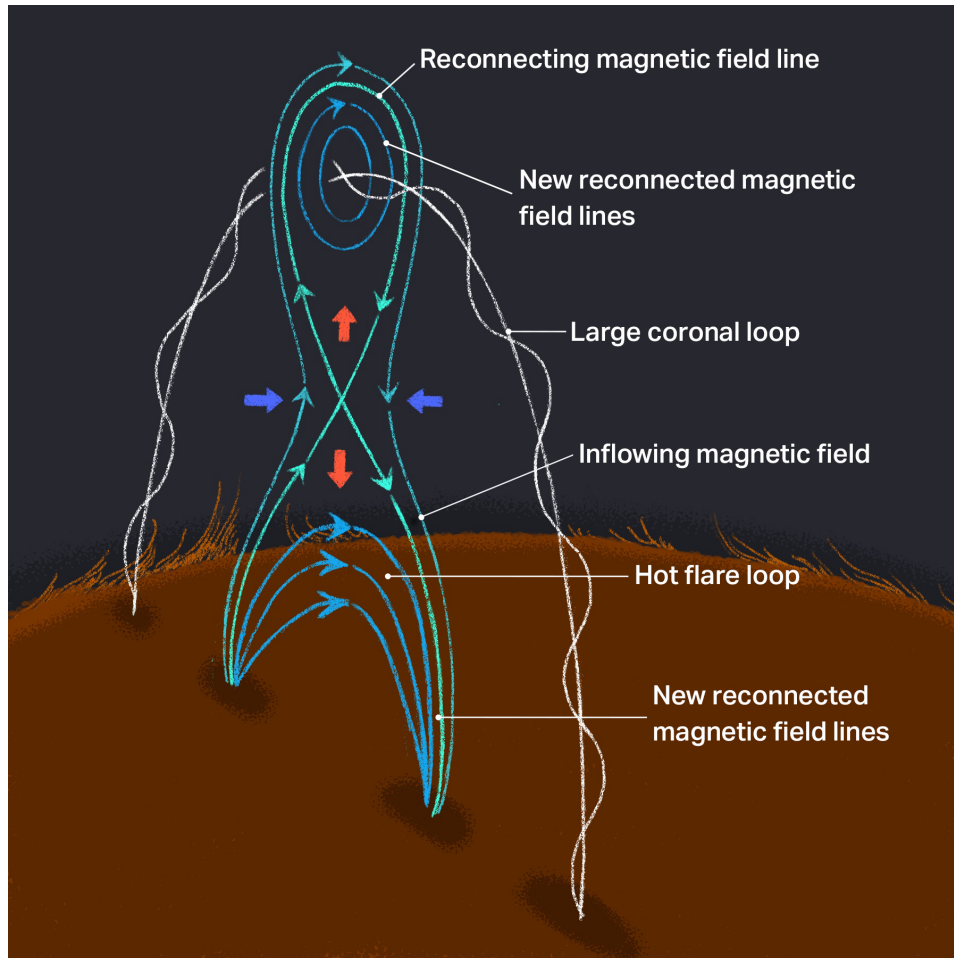


Figure 1.12: During magnetic reconnection events, accelerated particles are released from the upper loop, whereas a population of mildly relativistic electrons is trapped within the lower loop - releasing radio emission through gyrosynchrotron radiation. This radio emission is one of the only ways to trace the energetic particles during these events. Artist's conception, commissioned and used here with permission from Alexandra Lash.

Chapter 2

Radio Astronomy

Earth's atmosphere is opaque to most wavelengths of light across the electromagnetic spectrum, although a few wavelength ranges are able to transmit through the atmosphere with little disturbance. Atmospheric ozone absorbs UV emission, and almost all of the incoming X-rays and gamma rays are absorbed by oxygen and nitrogen in the upper atmosphere, while infrared emission is absorbed by carbon dioxide and water vapour (Rees, 1989). Although the relatively narrow frequency range of visible light is largely transmitted through the atmosphere, it is subject to distortion by air turbulence - leading to the demand for space-based optical telescopes. Incoming radio-wavelength light spanning frequencies of 20 kHz to 300 GHz (or 1 mm to >1000 km) is transmitted with little atmospheric distortion down to frequencies of < 10 MHz, below which it is then reflected by Earth's ionosphere. This gives radio astronomers a unique advantage to observing with ground-based telescopes. They are located in dry sites to minimise the effects of water vapour, which can absorb incoming radio emission. However, observing at such long wavelengths introduces some challenges to constructing a sufficiently sensitive telescope.

2.1 Radio Telescopes

The broad frequency range spanned by radio emission means that nearly every astronomical object is active in at least some radio bands. However, the range is

too wide for a single telescope to effectively cover the full spectrum, leading to a variety of designs used to convert radio emission in a limited range of frequencies to electric currents. This can take a number of diverse forms, ranging from dipole and horn antennas to parabolic antennas or arrays. A single dipole antenna design, such as that used by Low-Frequency Array (LOFAR), consists of co-linear conductors that receive current related to the frequency of incoming radiation. Horn antennas receive incoming radiation through a large, directional opening that is tapered down to a single dipole antenna and converted into a current that measures intensity. The most famous example of a horn antenna is the Bell Labs Holmdel antenna, which enabled Arno Penzias and Robert Wilson to make the accidental discovery of the cosmic microwave background radiation (Penzias and Wilson, 1965). Parabolic antennas collect incoming radio emission in a large reflecting dish that focuses onto a small feed antenna, where they are reflected back onto a feed horn in the paraboloid that amplifies and converts the signal. All of the data used in this thesis were collected by arrays of parabolic antennas called interferometers, discussed in further detail below.

A single dish parabolic antenna needs to have a much larger collecting area than optical telescopes in order to achieve a comparable resolution because of the long wavelengths involved. Angular resolution is typically defined by the Rayleigh Criterion, or the minimum angular resolution needed to resolve two distinct sources. This definition is based on the Airy diffraction patterns generated by two point sources separated by an angular distance θ . The two sources are considered unresolved when their maxima overlap, and the Rayleigh Criterion is met when maxima of the two sources overlap but are distinguishable. This is given by,

$$\theta \approx 1.22 \frac{\lambda}{D}, \quad (2.1)$$

where θ is the angular resolution in radians, λ is the wavelength of measured radiation, and D is the diameter of the aperture (Rayleigh, 1880). In radio astronomy, it is conventional to approximate the resolution as $\theta \approx \lambda/D$, where the requirement for resolveability is set by the overlap in the full-width-half-maximum of the source maxima. It is clear from this relation that larger values of λ require correspondingly large values of D to maintain a constant angular resolution θ . Following the

Rayleigh Criterion, optical telescopes can achieve a 1'' resolution with less than a 1 m diameter aperture. In contrast, at radio frequencies where λ is large, telescopes with diameters ranging from 200 m to 1000 km are necessary to achieve the same resolution if using a single collecting area. The two largest single dish radio telescopes, Five-Hundred-Meter Aperture Spherical radio Telescope (FAST) and the late Arecibo Observatory, have angular resolutions of 3'' and 4'', respectively - still significantly less than the 1'' angular resolution met even by small optical telescopes such as the Transiting Planets and Planetesimals Small Telescope.

It is not structurally feasible to construct single radio dishes with the excessively large diameters necessary for $\sim 1''$ resolution, but it can instead be done through the combination and synthesis of signals from multiple antennas separated by distances larger than the dishes themselves. The method of doing this is called interferometry, and the telescope arrays used to synthesize one coherent signal are known as interferometers. A review of interferometers is included below, followed by a brief discussion of the historical context.

2.2 Interferometry

The observations presented in this work make use of the VLA and ALMA interferometers, two of the few radio telescopes in the world with the sensitivity necessary to detect the dim radio emission of ultracool dwarfs. Both arrays use parabolic antennas, which consist of a primary mirror that reflects incoming radio waves onto a focus, a steerable antenna that can track sources in two dimensions, a secondary mirror that focuses incoming radio waves to a receiver located behind the primary mirror, and a receiver waveguide that finally collects the incoming radiation and transmits it to a cryogenically cooled amplifier. Note that radio mirrors do not need to be smoothed to the same degree as optical mirrors, and are made from metal with a surface too rough to act as a mirror to optical light.

Radio interferometers use aperture synthesis, or the process of combining the signals of many individual dishes, to operate with the angular resolution of a single very large antenna the size of the full collection area. Each individual telescope measures the amplitude and phase of the incoming radiation, which are then combined pairwise through cross-correlation. In aperture synthesis it is the

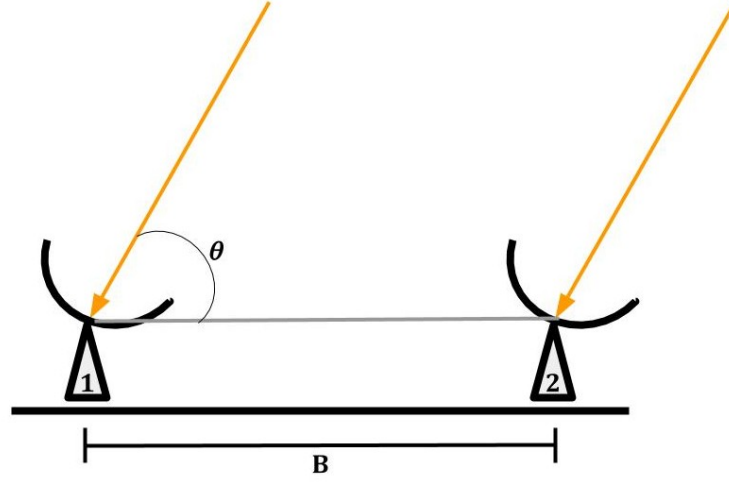


Figure 2.1: Diagram of a simple two-element interferometer, with antennas 1 and 2 separated by baseline B . Incoming light will produce voltages V_1 and V_2 from each element, separated by a geometric time delay $\tau = B \sin \theta v/c$.

baseline, or separation of an antenna pair, that ultimately determines the angular resolution. Interferometers are limited to the same field of view as an individual antenna, but the sensitivity improves non-linearly with the number of elements. A synthesis telescope does not behave exactly like a single dish telescope of the same size, rather the received electric field is used to infer properties of the sources instead of directly measuring the intensity.

The simplest interferometer consists of two antennas, 1 and 2, separated by a baseline B (Figure 2.1). If there is a point source emitting at frequency ν , light from that source will reach each antenna at different times separated by a geometric time delay $\tau = B \sin \theta/c$, where $B \sin \theta$ is the resulting phase difference of light arriving at each aperture. Each antenna converts received light into a voltage, V_1 and V_2 , related to the angular frequency $\omega = 2\pi\nu$, time t , and time delay τ by,

$$V_1 = V \cos(\omega t)$$

$$V_2 = V \cos(\omega(t - \tau)).$$

A correlator multiplies the two voltages together,

$$V_1 V_2 = \frac{V^2}{2} (\cos(2\omega t - \omega\tau) + \cos(\omega\tau)), \quad (2.2)$$

and averages the resulting signal over a long enough time ($\Delta t \gg 0.5\omega$) to remove the $\cos(2\omega t - \omega\tau)$ term from the final signal, which becomes,

$$\begin{aligned} R &= \langle V_1 V_2 \rangle \\ &= \frac{V^2}{2} \cos(\omega\tau). \end{aligned} \quad (2.3)$$

Both an amplitude and a phase term, $V^2/2$ and $\cos(\omega\tau)$, are included in the final expression. This cross-correlation process measures the *coherence* of the two received signals, as opposed to directly measuring the intensity of the source.

An interferometer measures the even and odd components of the amplitudes (cosine and sine, respectively), leading to a complex coherence of the individual antennas that includes both amplitude and phase measurements. This is called the complex visibility function $V(u, v)$, which can then be transformed into a sky brightness. The u direction points *East-West*, and the v direction points *North-South*. The separation between two antennas in an interferometer is typically given in terms of the number of wavelengths λ in the directions u and v . Let the sky plane have an intensity distribution given by the function $T(l, m)$, where l and m are angular measurements in the East-West and North-South directions, and are measured in radians. The u, v and l, m planes are tangent to one another, where the u, v plane is dome-shaped and the l, m plane is the flat sky plane, assuming small angles. The two planes are related to one another by a Fourier transform (see Section 2.2.3), $V(u, v) \xrightarrow{F} T(l, m)$, or

$$V(u, v) = \int \int T(l, m) e^{-i2\pi(ul+vm)} dl dm. \quad (2.4)$$

An interferometer samples the u, v plane according to the number of unique baselines, $\frac{1}{2}N(N - 1)$ times, where N is the total number of antennas. The Fourier transform of the weighted sampling of the u, v plane is called the “dirty beam”, shown in Figure 2.2. As such, each point in the visibility $V(u, v)$ plane contains in-

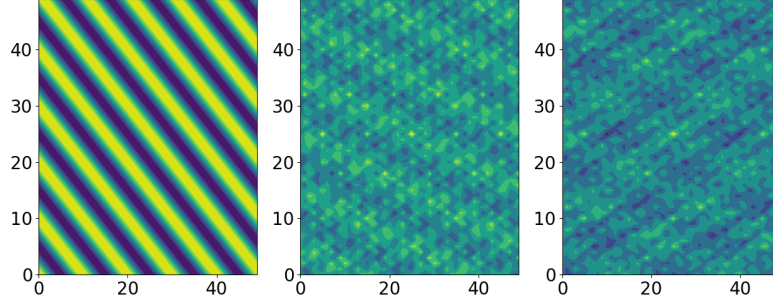


Figure 2.2: Dirty beam produced by an interferometric measurement of one point on the u, v plane, in ambiguous sky coordinates, or the Fourier transform of the sampling function. They are produced by two antennas (left), four antennas (middle), and five antennas (right). The position of the antennas and baseline between them determines the distribution of sine waves in the pattern. Adding additional antennas is useful for filling in the u, v plane.

formation on the sky brightness plane $T(l, m)$ plane everywhere rather than confined to one particular region. Each visibility is also a complex quantity, containing both real and imaginary components that correspond to the amplitude and phase of the coherent signal, respectively. The amplitude component describes the “brightness” at a certain frequency, while the phase component describes the location of the source - so the visibility evaluated at the centre of the visibility plane, $V(u = 0, v = 0)$ is just the total flux density.

In radio interferometry, the “primary beam” is defined as the Fourier transform of the telescope aperture. It is the full-width-half-maximum (λ/D , where D is the diameter of a single dish) of the main lobe directed towards the source. While there is additional response in the antenna due to side lobes (smaller, peripheral beams shown in Figure 2.3), the primary beam of an interferometer is akin to the field of view.

Because the u, v plane sampling is necessarily incomplete, the resulting dirty beam can retain some noise-like structure that is imposed on the dirty image, or sky brightness convolved with the dirty beam. The impact of this beam pattern can

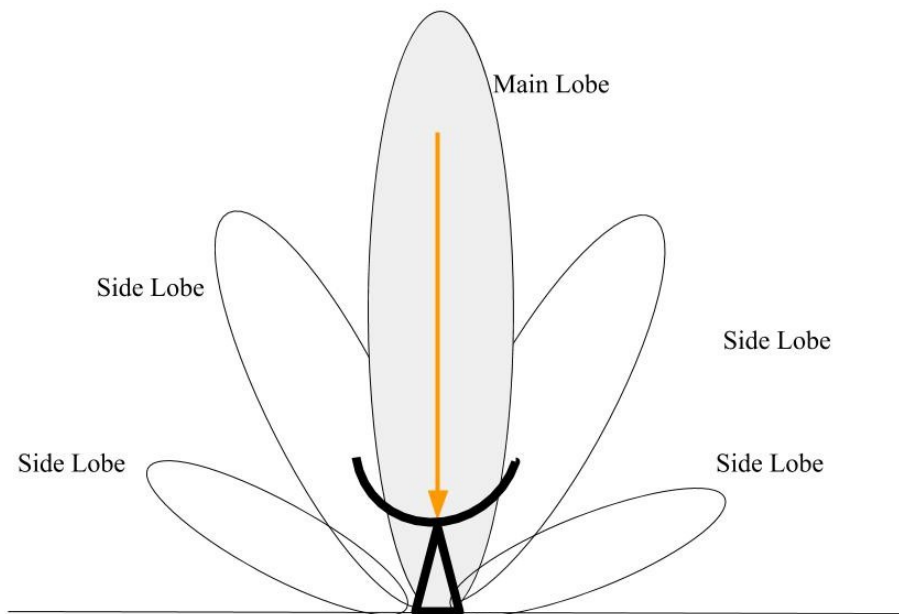


Figure 2.3: The radiation pattern produced by a radio telescope. The main lobe is where the majority of the signal is received, and is oriented toward the observing target. The side lobes, produced by the diffraction pattern of the beam, usually pick up radiation from outside the intended field of view.

be corrected by iteratively removing the antenna response, done in the CLEANing process (discussed in Section 2.2.4). This process is unfortunately not always straightforward, and a bright object captured in the side lobes can introduce significant artefacts to the data that cannot be easily removed, as in the case of my 3 GHz TRAPPIST-1 observations (Figure 2.4).

2.2.1 The Karl G. Jansky Very Large Array

By the mid-twentieth century, it became clear that the construction of radio interferometers was necessary in order to achieve significant improvement in the resolution of radio observations. In 1959, the National Science Foundation (NSF) officially appointed a committee to improve upon existing instrumentation and investigate

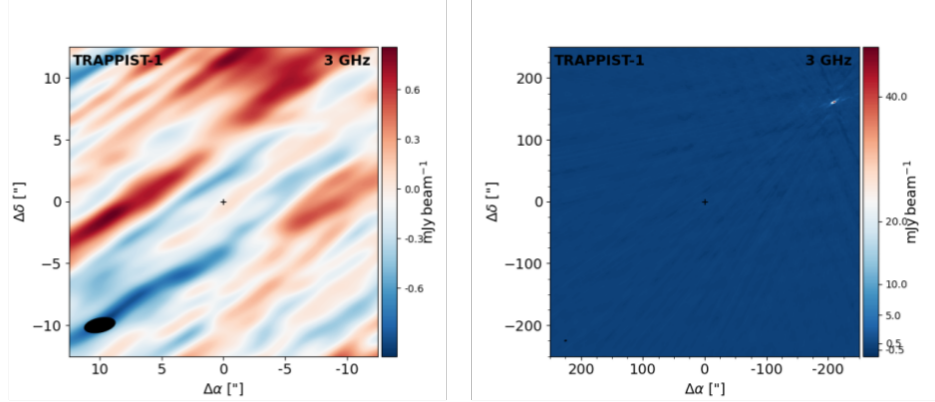


Figure 2.4: 3 GHz observations centred on TRAPPIST-1. The image is corrupted by significant artefacts caused by a bright quasar seen in the wide-field image on the right.

the construction of more powerful radio telescopes. The committee did discuss the development of a 16-element array consisting of 61 8-metre antennas as well as a proposed spherical reflector telescope in Puerto Rico. However, this did not lead to any concrete plans for construction, with the committee noting that the biggest hurdle was a lack of radio astronomers in the United States and recommended increasing the funding for academic programs in radio astronomy.

Fortunately, the National Radio Astronomy Observatory (NRAO) in the early 1960's began developing plans to build a hypothetical telescope called the Very Large Antenna (VLA), later renamed the Very Large Array when the plan evolved from a single dish to an interferometer. It was originally envisioned to include 100-150 antennas and extend for several kilometers in a T-shaped configuration. By the time the VLA was given congressional approval and construction was started in 1972, the details of the telescope had changed significantly to include fewer antennas now arranged in a Y-shape. The VLA was designed to study a range of topics in radio astronomy, although the 1965 initial VLA report did not mention stellar physics and it was only given a cursory note in the 1967 project proposal. It now accounts for a large fraction of VLA observing time. A more detailed history is described in Kellermann et al. (2020).

The VLA today is dedicated to Karl G. Jansky, and is located in the plains of San Augustine, New Mexico. It consists of 27 antennas, each 25 m in diameter. The antennas can be relocated along tracks to accommodate a range of baselines, with maximum separations between dishes ranging from 1 to 36 km depending on the array configuration. The VLA covers a frequency range from 74 MHz - 50 GHz (400 – 0.7 cm), which includes the peak emission frequency for ECMI and gyrosynchrotron emission given the typical UCD magnetic field strength. The VLA is able to achieve an angular resolution ranging from 0.043'' to 46'' depending on the array configuration and observing band.

2.2.2 The Atacama Large Millimetre Array

The Atacama Large Millimetre Array (ALMA) was originally proposed in the late 1990s as a collaborative effort between the NRAO and the European Southern Observatory (ESO) to develop a radio telescope with the sensitivity of the Large Southern Array (LSA) and the Millimetre Array (MMA), planned projects that never saw construction. The National Astronomical Observatory of Japan (NAOJ) later joined the collaboration, adding a smaller array of telescopes called the Atacama Compact Array. The acronym ALMA was agreed upon because the word *alma* translates to “soul” in Spanish and “knowledgeable” in Arabic. Construction on the telescope ran from 2008-2011 in the Atacama desert in Chile, and the telescope began to take observing proposals in 2012.

ALMA consists of 66 total antennas, 54 of which are 12 m in diameter and 12 of which are 7 m in diameter. The antennas can be moved around using massive transporter trucks to accommodate baselines ranging from 0.15 – 16 km, depending on the array configuration. ALMA covers a frequency range significantly higher than the VLA, ranging from 84 GHz (3.6 mm) to 950 GHz (0.3 mm). ALMA is able to achieve an angular resolution of 0.002'' – 50'', depending on the array configuration and observing band.

2.2.3 The Fourier Transform

The Fourier transform is a helpful tool in multiple disciplines ranging from engineering to quantum mechanics, and is particularly useful in radio astronomy. As

discussed above, radio interferometers measure the coherence of antenna pairs, which is represented by the complex visibility function. While radio interferometers cannot directly image sources as optical telescopes can, the Fourier transform can be used to map the visibility (u, v) plane to a sky brightness distribution (l, m) , where it can be imaged and analyzed. The Fourier transform is a special case of the Fourier series, defined by,

$$f(x) = \sum_{n=-\infty}^{\infty} A_n e^{i2\pi n s_0 x}, \quad (2.5)$$

where the function $f(x)$ is period with period L , and A_n is given by the equation,

$$A_n = \frac{1}{L} \int_{L/2}^{L/2} f(x) e^{i2\pi n s_0 x} dx. \quad (2.6)$$

A Fourier transform between the two functions $f(x)$ and $F(s)$ is defined by the following integrals,

$$F(s) = \int_{-\infty}^{\infty} f(x) e^{-i2\pi s x} dx, \quad (2.7)$$

$$f(x) = \int_{-\infty}^{\infty} F(s) e^{i2\pi s x} ds. \quad (2.8)$$

In this formalism, Equation 2.7 is called a *forward* Fourier transform, while Equation 2.8 is a *backwards* or *inverse* Fourier transform. The two-dimensional case of the Fourier transform involves a similar formalism, but integrates over the two variables associated with either function as was done in Equation 2.4 to transform the complex visibilities $V(u, v)$ into a sky brightness distribution $T(l, m)$.

One of the most important applications of the Fourier transform in radio astronomy is the convolution theorem. The convolution, or folding, function finds the “overlap” between two functions as one function is “dragged” over the other, resulting in a third function that expresses the “blending” of the two functions. Formally, the convolution of two functions $f(x)$ and $g(y)$ is,

$$(f * g)(x) = \int_{-\infty}^{\infty} f(y) g(x - y) dy. \quad (2.9)$$

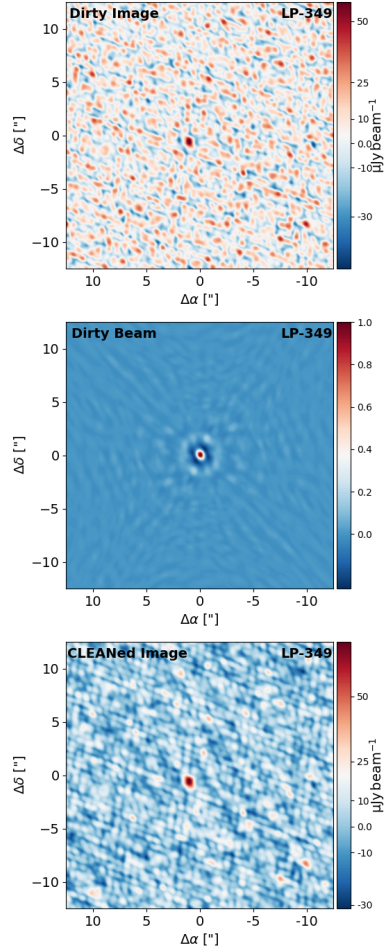


Figure 2.5: The cleaning process for the radio bright UCD LP 349-25, presented in the following Chapter. The “dirty” image constructed from the sampling of points on the $u - v$ plane. The following “clean” image has been processed using the CLEAN algorithm in the CASA software, which removes some of the structure of the dirty beam resulting from artefacts of an incompletely-sampled Fourier space.

In radio astronomy, convolution is used to create an image of the sky brightness, discussed below.

2.2.4 Imaging in Interferometry

Interferometry works by sampling the visibility plane $V(u, v)$ at enough points, using individual antennas at different baselines to synthesize one large antenna that extends to the longest baseline. One pair of antennas comprises one baseline, which provides two samples of the (u, v) plane at a time, and an array of N antennas will provide $N(N - 1)$ samples at a time. The (u, v) plane can be further filled out by making use of the Earth's rotation to sample the (u, v) plane at many different points over time as well as by physically moving the antennas to new configurations. The collection of points measured in the (u, v) plane is given by the sampling function,

$$S(u, v) = \sum_{k=1}^M \delta_k(u - u_k, v - v_k), \quad (2.10)$$

where M is the total number of points where measurements are made. The sampled visibility function is $V(u, v)S(u, v)$, and can be Fourier transformed to give the sampled sky brightness, or “dirty image”, $T^D(u, v)$. $T^D(u, v)$ can also be calculated by convolving the sky brightness with the Fourier transform of the sampling function (the dirty beam),

$$T(l, m) * s(l, m) = T^D(l, m), \quad (2.11)$$

where $s(l, m)$ is also called the point spread function or the dirty beam. Since an image is constructed from limited sampling of points on the $u - v$ plane, significant noise-like structure can be introduced through convolution with the dirty beam. The resulting dirty image resembles the original sky brightness, but retains some of the noise-like structure of the dirty beam. While there is no unique way to deconvolve the dirty beam from the dirty image, reliable and effective algorithms have been developed to do so. In this work, the artefacts introduced by the dirty beam are iteratively removed using the CLEAN algorithm (Högbom, 1974), resulting in a “clean image”. The CLEAN algorithm assumes that the sky brightness can be represented as a collection of point sources. It iteratively searches for the position and strength of the brightest points in the dirty image, multiplies a fraction of those points by the dirty beam, and subtracts that from the image, repeating until a desired RMS is reached. All of the observational CLEANing imaging in this thesis was done using the Common Astronomy Software Application (CASA), a software

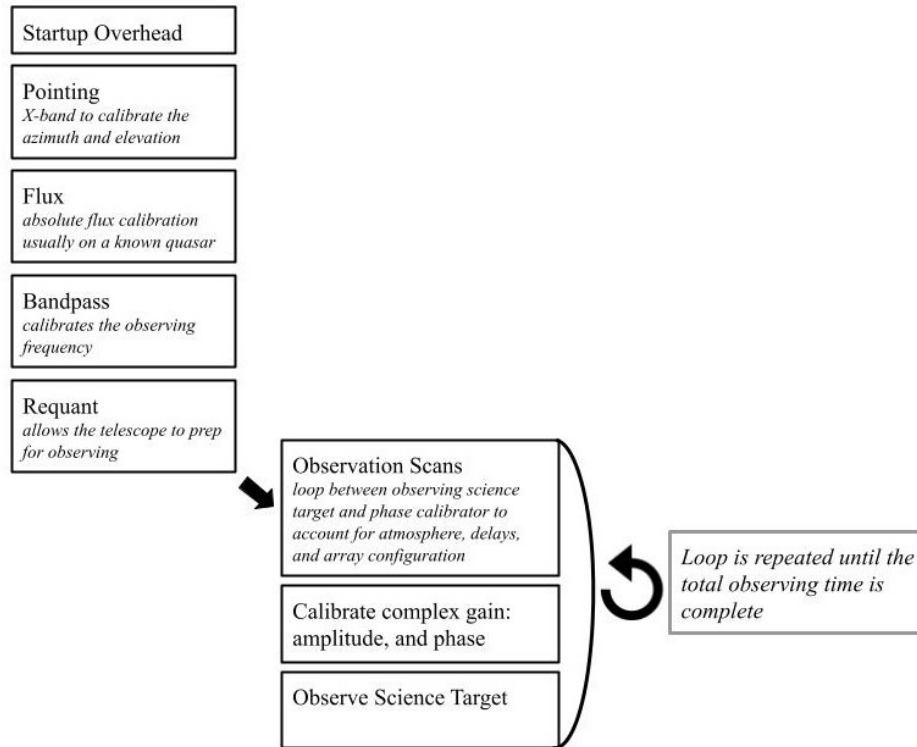


Figure 2.6: The structure of VLA observations, as set up with their Observing Tool. The startup overhead has a fixed time of approximately seven minutes to slew from a previous observing target to the locations of the gain calibrator - usually a quasar with known flux - as well as account for delays due to wire wrapping in the antennas. The following set of calibrations, including pointing, flux, bandpass, and requant are usually done on the gain calibrator, but the phase calibrator can be used as well. If the observations are long enough, an additional flux calibration may be needed to break up observing scan loops as atmospheric conditions may change.

package used to calibrate and analyze radio data for ALMA and the VLA. This is shown in Figure 2.5 for the UCD LP 349-25, discussed further in the following chapter.

Both ALMA and the VLA have a calibration process designed to correct for instrumental and atmospheric conditions that can introduce noise into the data, as

well as measure the absolute flux of a known source. The absolute flux calibration is performed by choosing from a short list of very bright quasars (and sometimes additional Solar System objects for ALMA) that have well-known and monitored brightness at the frequency of observations. This is used to scale the relative amplitudes of the science target to an absolute value. Bandpass calibration solves for timing variations in the phase and amplitude of the signals arriving at each antenna in the array, and can be performed on the same source chosen for the absolute flux calibration or a different source with well-known brightness at the observing frequency. The observations of the science target are done by slewing between the target itself and a nearby gain calibrator that measures the amplitude and phase of a known source. Unlike the flux or bandpass calibrators, the gain calibrator must be located very close to the science target ($<15^\circ$ depending on observing frequency) to minimise the time taken to slew between the science target and gain calibrator and account for atmospheric conditions in the pointing direction of the science target.

Chapter 3

Ultracool Dwarf Radio Emission

This chapter is based on an ApJ submission (Hughes et al., 2021). It uses ALMA and VLA observations of five ultracool dwarfs to measure the strength of radio emission or place upper limits in the case of a non-detection. Co-authors on this paper include Aaron Boley, Rachel Osten, Jacob White, and Marley Leacock.

3.1 Introduction

A large part of my work involved examining the radio emission of a sample of five UCDs at 30-100 GHz frequencies. For typical UCD magnetic field strengths, emission due to both the electron cyclotron maser (Chapter 1.5.3) and gyrosynchrotron radiation (Chapter 1.5.5) is expected to peak in the 1 – 10 GHz range for the expected magnetic field strengths. Coherent emission from ECMI drops off steeply at frequencies outside this range, while gyrosynchrotron emission trails off slowly and remains detectable at higher frequencies. This survey consists of observations of five UCDs, three of which were observed with ALMA at 97.5 GHz and one observed with the VLA at 33 GHz.

As discussed, UCDs are among the most common stellar objects in the Milky Way (Henry et al., 2006), yet due to their faintness they are difficult to study. Early predictions of UCD magnetic activity and radio emission indicated that they should be magnetically inactive due to their fully convective interiors, and the Güdel-Benz relation suggests that they should be radio faint. However, high sensitivity radio

telescopes such as the VLA and the late Arecibo observatory have revealed that about 10% of UCDs are bright at radio frequencies (Antonova et al., 2013; Route and Wolszczan, 2016; Lynch et al., 2016; Berger, 2006), and strong magnetic fields up to kG strength have been measured in UCDs (Reiners and Basri, 2006; Reiners, 2009; Reiners and Basri, 2010). UCDs occupy the mass range in the transition between giant planets and stars, and observations indicate that radio loud UCDs are capable of behaving like either (Berger et al., 2001; Berger, 2006; Hallinan et al., 2006; McLean et al., 2012; Williams et al., 2015), by producing auroral ECMI emission similar to what is seen from Solar System planets or synchrotron and gyrosynchrotron radiation akin to what is seen in stars.

Both emission mechanisms peak near the cyclotron frequency, leading to some potential conflation between the two. Observations at high radio frequencies above the threshold for ECMI emission can uniquely pick out emission due to gyrosynchrotron radiation. These observations are useful to **(a)** determine whether gyrosynchrotron radiation is present in the target, **(b)** determine the strength and spectral index of the emission, and **(c)** use those results to inform theoretical models of UCD magnetic activity.

The emission mechanism(s) of radio loud UCDs has implications for the magnetic field generation in these objects, as different dynamo models may be needed to explain each emission scenario. For example, Williams et al. (2014) suggest a model wherein the magnetic field topology itself causes frequent reconnection events and corresponding radio emission. On the other hand, the presence of auroral emission could suggest a global dipolar magnetic field (Kao et al., 2016; Pineda, 2017; Berdyugina et al., 2017), in which the co-rotation breakdown between magnetospheric plasma and the UCD magnetic field enables electrons to drift along electromagnetic currents (Cowley and Bunce, 2001) as discussed for ECMI emission in Chapter 1. Both situations could occur simultaneously, with a global dipolar magnetic field producing auroral emission and localized reconnection events producing gyrosynchrotron radiation.

UCDs are likely to have a high occurrence rate of terrestrial planets (Dressing and Charbonneau, 2015). This presents a different possibility for the origin of ECMI emission; planets in orbit around UCDs may be capable of inducing auroral radio emission analogous to Io around Jupiter (Turnpenney et al., 2018). However,

should gyrosynchrotron emission and the corresponding reconnection events also be present, then the stability of planetary atmospheres could be threatened by the outgoing energetic particle flux (Segura et al., 2010; Tilley et al., 2017).

In this chapter, I present high radio frequency observations (30 – 100 GHz) of five UCDs. Prior to this work, the only UCD to be detected in this frequency range was TVLM 513-46546, which Williams et al. (2015) found to have 95 GHz emission consistent with gyrosynchrotron radiation. The results of this analysis revealed that only two of the five targets are radio quiet over the course of the observations, while the remaining three were radio bright with emission similar to that of TVLM 513-46546. The detected UCDs represent the second through fourth UCDs found to emit at millimetre wavelengths.

3.2 Observations and Results

In this section, I discuss each of the five targets used in this study along with the corresponding observations. The results and target properties are reported in Table 4.2.

The UCDs in this survey have a range of characteristic, including both high and low $v \sin i$, with rates ranging from around 9 to over 80 km s⁻¹.

Property	LP 349-25 AB	LSR J1835+3259	NLTT 33370	LP 415-20	LP 423-31
Spectral Type	M8 ⁽¹⁾	M8.5 ⁽⁵⁾	M7 ⁽⁷⁾	M9.5 ⁽¹⁰⁾	M7 ⁽¹¹⁾
M_{tot} (M_{\odot})	$0.120^{+0.008(2)}_{-0.007}$	$0.050 \pm 0.0038^{(6)}$	$0.179^{+0.055(8)}_{-0.062}$	0.09 ± 0.06	$0.010 \pm 0.003^{(12)}$
Distance (pc)	$10.3 \pm 1.70^{(3)}$	$5.67 \pm 0.02^{(5)}$	$16.39 \pm 0.75^{(7)}$	$21 \pm 5^{(10)}$	$10.7 \pm 0.3^{(12)}$
Age (Myr)	-	$22 \pm 4^{(6)}$	$\sim 30 - 200^{(8)}$	-	-
T_{eff} (K)	-	$2800 \pm 30^{(6)}$	$3200 \pm 500^{(8)}$ $3100 \pm 500^{(8)}$	$2600 \pm 100^{(10)}$ $2400 \pm 100^{(10)}$	-
$v \sin i$ (km s^{-1})	$55 \pm 2^{(4)}$ $83 \pm 3^{(4)}$	$50 \pm 5^{(6)}$	$45 \pm 5^{(9)}$	$44 \pm 4^{(4)}$ $36 \pm 4^{(4)}$	$9.0 \pm 2^{(11)}$
Obs Frequency (GHz)	97.5	97.5	97.5	97.5	33.0
Flux (μJy)	70 ± 15	114 ± 21	604 ± 61	< 20	< 30

Table 3.1: Properties of ultracool dwarfs presented in this work, including combined spectral type, total mass (M_{tot}), stellar distance, stellar age, effective temperature (T_{eff}), and $v \sin i$, frequency of the observations ν (GHz), and observed flux (μJy). References: (1) Gizis et al. (2000) (2) Konopacky et al. (2010) (3) Schmidt et al. (2007) (4) Konopacky et al. (2012) (5) Reid et al. (2003) (6) Berdyugina et al. (2017) (7) Lépine et al. (2009) (8) Schlieder et al. (2014) (9) McLean et al. (2011) (10) Siegler et al. (2003) (11) Reiners and Basri (2010) (12) Cruz et al. (2003).

LP 349-25, LSR J1835+3259, and NLTT 33370 are detected and exhibit bright radio emission at 97.5 GHz. All three of these targets were also detected at lower radio frequencies in previous studies (e.g., Phan-Bao et al., 2007; Hallinan et al., 2008; McLean et al., 2011). In contrast, the observations of LP 423-31 and LP 415-20 yield null detections at 97.5 GHz and 33 GHz, respectively. LP 423-31 had been previously observed at 8.46 GHz, which also resulted in a null detection, while there are no previous radio observations of LP 415-20. For both targets, I used the non-detections to place upper limits on the radio fluxes.

3.2.1 LP 349-25

LP 349-25 is a spectroscopic binary of spectral types M8 and M9 and combined spectral type M8.5, with rapid rotation speeds of 55 ± 2 and $83 \pm 3 \text{ km s}^{-1}$, respectively (Konopacky et al., 2012). It was previously detected at 8.46 GHz by Phan-Bao et al. (2007) at a flux density of $365 \pm 16 \mu\text{Jy}$, and at 5 GHz with a flux

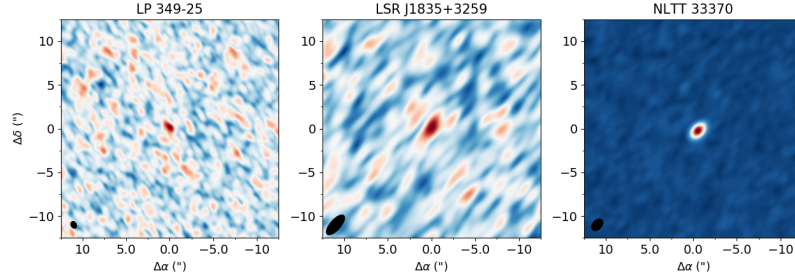


Figure 3.1: All detected UCDs. The visibilities are phase-shifted to account for the proper motion. LP 349-25 has peak flux of $70 \mu\text{Jy}$ with RMS of $9 \mu\text{Jy}$, LSR J1835+3259 has a peak flux of $114 \mu\text{Jy}$ with RMS $18 \mu\text{Jy}$, and NLTT 33370 has a peak quiescent flux of $604 \mu\text{Jy}$ with RMS $7.3 \mu\text{Jy}$. The synthesized beam is denoted by the black ellipse in the bottom left of each image.

densities of $329 \pm 38 \mu\text{Jy}$ by Osten et al. (2009) and by McLean et al. (2012) at $323 \pm 14 \mu\text{Jy}$, also at 8.46 GHz.

The archival ALMA Cycle 4 observations (ID 2016.1.00817.S), were centered on J2000 coordinates RA=00h 27m 55.99s $\delta = +22^\circ 19' 32.80''$, where δ in this context refers to the declination of the source. The data were taken in 3 execution blocks (EBs) from 2016 October 22 to 2016 November 6 for a total of 2 hr on-source (2.9 hr including overhead). There were 45 antennas used with baselines ranging from 15 m to 500 m.

The Band 3 observations have a total bandwidth of 8 GHz split among 4 spectral windows (SPW), or sub-bands of the total observing bandwidth. Each SPW has 128×15.625 MHz channels. The SPWs are centred at 90.4 GHz, 92.4 GHz, 102.5 GHz, and 104.5 GHz, giving an effective continuum frequency of 97.5 GHz. The data were reduced using CASA 5.4.1 (McMullin et al., 2007), which included water vapour radiometer (WVR) calibration; system temperature corrections; flux and bandpass calibration with quasar J0423-0120; and phase calibration with quasar J0431+1731. The average precipitable water vapour (PWV) was 2.08 mm throughout the observations.

I generated CLEANed images using the CASA task *tclean*, natural weighting down to a threshold of the RMS noise, and a cell size of 1/10 the beam size. These

ALMA 97.5 GHz observations achieve an RMS sensitivity of $9 \mu\text{Jy beam}^{-1}$ as measured from the CLEANed image away from the source. The synthesized beam is $0.82'' \times 0.62''$ at a position angle of 28.3° , corresponding to 7 au at the system distance of 10.3 ± 1.70 pc (Schmidt et al., 2007).

From the CLEANed image, I measured a 97.5 GHz flux density of $70 \pm 9 \mu\text{Jy}$. The data were subsequently split by observing scan, and both the flux density and RMS of each scan were taken using *uvmodelfit* to generate a time series. No flaring activity was seen over the course of the observations.

3.2.2 LSR J1835+3259

LSR J1835+3259 is a brown dwarf of spectral type M8.5 (Reid et al., 2003) with a rapid rotation speed of $v \sin i = 50 \pm 5 \text{ km s}^{-1}$ known to be variable across multiple wavelengths. It has been detected at 8.44 GHz with both quiescent, largely unpolarized emission and 100% circularly polarized bursting emission, with an average flux density of $722 \pm 15 \mu\text{Jy}$ and variable emission reaching up to $2500 \mu\text{Jy}$ (Hallinan et al., 2008).

The archival ALMA Cycle 4 observations (ID 2016.1.00817.S), were centered on J2000 coordinates $\text{RA} = 18\text{h } 35\text{m } 37.88\text{s}$, $\delta = +32^\circ 59' 53.31''$. The data were taken in 2 EBs from 2016 November 6 to 2016 December 1 for a total of 1 hr on-source (2 hr including overhead). There were 40 antennas used with baselines ranging from 15 m to 460 m.

The Band 3 observations have a total bandwidth of 8 GHz split among 4 SPWs. Each SPW has 128×15.625 MHz channels. The SPWs are centered at 91.5 GHz, 93.4 GHz, 101.5 GHz, and 103.5 GHz, giving an effective continuum frequency of 97.5 GHz. The data were reduced using CASA 4.7.2, which included WVR calibration; system temperature corrections; flux and bandpass calibration with quasar J2025+3343; and phase calibration with quasar 3 J1848+3219. The average PWV was 2.53 mm throughout the observations.

I generated CLEANed images using the CASA task *tclean*, natural weighting down to a threshold of the RMS noise, and a cell size of 1/10 the beam size. These ALMA 97.5 GHz observations achieve an RMS sensitivity of $18 \mu\text{Jy beam}^{-1}$ as measured from the CLEANed image away from the source. The size of the resulting

synthesized beam is $2.85'' \times 1.18''$ at a position angle of -41.8° , corresponding to 12 au at the system distance of 5.6875 ± 0.0005 pc (Gaia Collaboration et al., 2018). From the CLEANed image, I measure a 97.5 GHz flux density of 114 ± 18 μ Jy. The data were subsequently split by observing scan, and both the flux density and RMS of each scan were taken using *uvmodelfit* to generate a time series. No flaring activity was seen over the course of the observations.

3.2.3 NLTT 33370

NLTT 33370AB (originally LSPM J1314+1320) is a resolved binary of combined spectral type M7.0e (Law et al., 2006; Lépine et al., 2009; Forbrich et al., 2016). This magnetically active system has been well-studied relative to other UCDs due to its brightness. Although the system is binary, I refer to it as NLTT 33370 for ease of reading.

NLTT 33370 has been detected with short, polarized bursts and quiescent, largely unpolarized radio emission, both of which are brighter than that observed in any other UCD. Quasi-quiescent emission was detected with the VLA at 8.46 GHz with flux density of 1156 ± 15 μ Jy and at 22.5 GHz with flux density of 763 ± 84 μ Jy (McLean et al., 2011). It was subsequently detected in a multi-wavelength study by Williams et al. (2015), exhibiting both quasi-periodic steady emission and flaring radio emission. These studies found that the steady emission was circularly polarized and modulated sinusoidally with a period of 3.89 ± 0.05 hr. Williams et al. (2015) further found an additional unpolarized component in one of their two VLA monitoring campaigns. The observations are interpreted to include a combination of flaring due to the ECMI and stable emission due to gyrosynchrotron radiation.

The archival ALMA Cycle 2 observations (ID 2013.1.00976.S), were centered on J2000 coordinates RA = 13h 14m 20.38s, $\delta = +13^\circ 18' 58.34''$. The data were taken in 4 execution blocks (EBs) from 2015 June 10 to 2015 June 12 for a total of 2.7 hr on-source (4.8 hr including overhead). There were 38 antennas used with baselines ranging from 25 m to 820 m.

The Band 3 observations have a total bandwidth of 8 GHz split among 4 SPWs, each with 64×31.25 MHz channels. The SPWs are centred at 90.5 GHz, 92.4 GHz, 102.5 GHz, and 104.5 GHz, giving an effective continuum frequency of 97.5 GHz.

The data were reduced using CASA 4.7.0, which included WVR calibration; system temperature corrections; flux and bandpass calibration with quasar J1229+0203; and phase calibration with quasar J1347+1217. The average PWV was 0.71 mm throughout the observations.

I generated CLEANed images using the CASA task *tclean*, natural weighting down to a threshold of the RMS noise, and a cell size of 1/10 the beam size. These ALMA 97.5 GHz observations achieve an RMS sensitivity of $9 \mu\text{Jy beam}^{-1}$ as measured from the CLEANed image away from the source. The size of the resulting synthesized beam is $1.58'' \times 1.04''$ at a position angle of -44.8° , corresponding to 22 au at the system distance of 16.39 ± 0.75 pc (Lépine et al., 2009). A 10-second flare (Fig. 3.2) was also captured during these observations, with a peak flux of $4880 \pm 360 \mu\text{Jy}$ from the CLEANed image using only the visibilities measured during the flare. From the CLEANed image using data that omit the flare, I measure a 97.5 GHz quiescent flux density of $604 \pm 7.3 \mu\text{Jy}$.

NLTT 33370 Flare

The origin of the NLTT 33370 burst is unclear, but consistent with previous observations of the system at lower frequencies. NLTT 33370 was found by Williams et al. (2015) to have both bursts and quiescent flux modulated with two distinct periodicities of 3.7859 ± 0.0001 and 3.7130 ± 0.0002 hr, slightly less than the stellar rotation period of 3.9 hr (McLean et al., 2011). I did not observe the flare to recur with either of these periods over the course of the rest of the observations. ECMI bursts due to auroral emission are expected to occur with the stellar rotation period. Unfortunately, none of the on-source observing blocks corresponded to a 3.9 hour interval from the time of the burst. Given the presence of quiescent emission at 97.5 GHz, the burst could be associated with gyrosynchrotron radiation released during a major flare. Long-term monitoring of NLTT 33370 at high radio frequencies is necessary to determine if such emission is quasi-periodic or stochastic.

The time-series of the flare (Figure 3.2) was generated by using the CASA task “split” to divide the observations into smaller time chunks, creating individual, short-term observations that are then used to create a light curve.

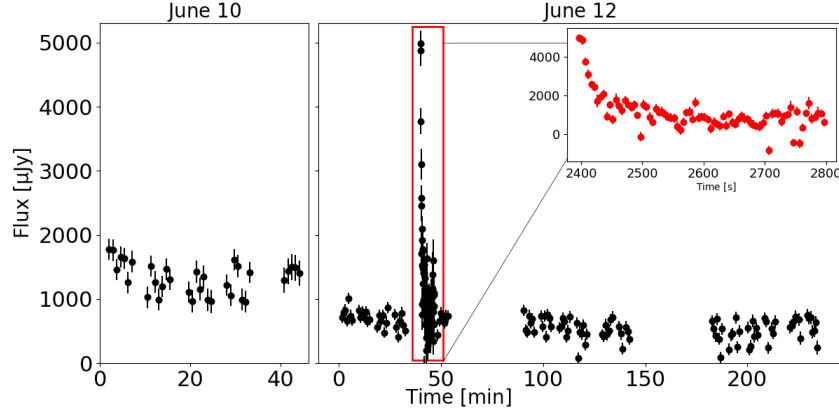


Figure 3.2: Time series of all NLTT 33370 observations presented in this work, including time on June 10th and June 12th, 2015. The data set was split into 30 s bins, and the peak flux and RMS were taken using the CASA task *uvmodelfit*. The two panels show the light curves of each day, while the overlaid plot shows the June 12 flare that reached a peak flux of $4880 \pm 360 \mu\text{Jy}$. Due to the gaps in the data, it is unclear whether this flare repeats with the stellar rotation.

3.2.4 LP 415-20AB

LP 415-20AB is a resolved binary with spectral types M7(A) and M9.5(B) and high $v \sin i$ of 40 ± 5 and $37 \pm 4 \text{ km s}^{-1}$, respectively (Konopacky et al., 2012). The presence of two UCDs with rapid rotation suggests that this system should be a radio emitter; however, I see no evidence of emission throughout the duration of my observations.

The ALMA Cycle 6 observations (ID 2018.1.01088.S, PI Hughes) presented here were taken in 3 EBs from 2019 January 8 to 2019 January 21 for a total of 2 hr on-source (2.7 hr including overhead). There were 58 antennas used with baselines ranging from 15 m to 500 m.

These Band 3 observations have a total bandwidth of 8 GHz split among 4 SPWs, each with $128 \times 15.625 \text{ MHz}$ channels. The SPWs are centred at 90.5 GHz, 92.4 GHz, 102.5 GHz, and 104.5 GHz, giving an effective continuum frequency of 97.50 GHz. The data were reduced using CASA 5.4.1, which included WVR

calibration; system temperature corrections; flux and bandpass calibration with quasar J0423-0120; and phase calibration with quasar J0431+1731. The PWV ranged from 2.9 mm to 5.9 mm throughout the observations.

I generated CLEANed images using the CASA task *tclean*, natural weighting down to a threshold of the RMS noise, and a cell size of 1/10 the beam size. These ALMA 97.5 GHz observations achieve an RMS sensitivity of $6.7 \mu\text{Jy beam}^{-1}$ as measured from the CLEANed image. The size of the resulting synthesized beam is $3.26'' \times 2.91''$ at a position angle of 30.1° , corresponding to 65 au at the system distance of 21 pc. It was a 97.5 GHz non-detection of LP 415-20AB with a 3σ upper level flux limit of $20 \mu\text{Jy}$ measured from the CLEANed image.

LP 423-31

LP 423-31 is an M7 star with a relatively low rotation rate of 9 km s^{-1} and strong magnetic field of $3500^{+400}_{-600} \text{ G}$ (McLean et al., 2011; Reiners and Basri, 2010). Berger (2006) placed an upper flux limit of $< 39 \mu\text{Jy}$ using VLA observations at 8.46 GHz. This star is expected to be radio silent given the existing trends and models in UCD radio emission, but confirmation is needed.

The observations were taken during the VLA Semester 18B (ID VLA-18B-241, PI Hughes) over 2 scheduling blocks (SBs) on 2018 December 12 for a total of 12.8 minutes on-source (35.5 min including overhead). Data were acquired with the array in the C antenna configuration, with 26 antennas and baselines ranging from 35 m to 3400 m.

The instrument configuration uses the Ka band receiver with a correlator setup consisting of $7808 \times 1 \text{ MHz}$ channels for a total bandwidth of 7.8 GHz. Four separate basebands are included with rest frequency centres at 30 GHz, 32 GHz, 34 GHz, and 36 GHz giving an effective continuum frequency of 33.0 GHz. The quasar J0750+1231 was used for gain and phase calibration and quasar 3C286 was used as a bandpass and flux calibrator. Data were reduced using the CASA 4.7.2 pipeline, which included bandpass, flux, and phase calibrations.

I generated CLEANed images using the CASA task *tclean*, natural weighting down to a threshold of the RMS noise, and a cell size of 1/10 the beam size. These VLA 33 GHz observations achieve an RMS sensitivity of $10 \mu\text{Jy beam}^{-1}$

as measured from the CLEANed image. The size of the synthesized beam is $0.86'' \times 0.72''$ at a position angle of 40.7° . The beam size corresponds to 8 au at the system's distance of 10.3 ± 1.7 pc (Konopacky et al., 2012). It was a 33 GHz non-detection of LP 423-31 with a 3σ upper level flux limit of $30 \mu\text{Jy}$ measured from the CLEANed image. The lack of emission at high radio frequencies of a slowly rotating UCD observed to be radio-quiet at lower frequencies is consistent with emerging trends in UCD radio emission that indicate rapid rotators are more likely to be radio bright, and that all UCDs active at high radio frequencies are also active at low radio frequencies.

3.3 Discussion

The five UCDs presented in this chapter have a range of properties, including low/high $v \sin i$ value, binarity, and detection/non-detection at low radio frequencies, making them a good selection for probing trends in high radio frequency emission. LP 349-25, LSR J1835+3259, NLTT 33370, and LP 423-31 have all been observed at lower radio frequencies. LSR J1835+3259, LP 349-45 and NLTT 33370 have been observed multiple times in the 1-10 GHz range where radio emission is expected to peak for typical magnetic field strengths. In all cases the observations were separated by years, suggesting that the low radio frequency emission is steady over multi-year timescales. LP 423-31, however, has been detected in some 8.46 GHz observations (Stelzer et al. in prep, private communication) and not detected in others (Berger, 2006). Altogether, I find that all three UCDs that are consistently active at low radio frequencies are also active at high radio frequencies, where ECMI emission is cut off. Furthermore, if the emission is largely due to ECMI, then there could be some level of circular polarisation present in the ALMA data. In principle, this would provide an additional metric to disentangle the emission mechanisms. Unfortunately, these data were taken in earlier ALMA cycles when polarisation calibration was unreliable so no conclusive determination on the presence of polarisation during the observations can be made. However, the inferred spectral indices and strength of emission at these high frequencies suggest that gyrosynchrotron radiation is active in all the detected UCDs. A larger sample of UCDs must be observed in this range to determine whether this small sample is

representative of radio emitting UCDs as a whole.

The measurements at different frequencies can be used to estimate a spectral index α such that $F_\nu \propto \nu^\alpha$ for flux density F_ν (Fig 3.3). Moreover, if gyrosynchrotron radiation is responsible for the detections, then the spectral indices can be related to an electron energy distribution following Dulk and Marsh (1982). LSR J1835-46546 and LP 349-25 have spectral indices of $\alpha = -0.76 \pm 0.07$ and $\alpha = -0.52 \pm 0.06$, respectively, which are consistent with optically thin gyrosynchrotron radiation. NLTT 33370 is best fit by a spectral index of $\alpha = -0.29 \pm 0.04$, slightly more shallow than what would be expected for gyrosynchrotron or synchrotron radiation. Using the relation between α and δ for gyrosynchrotron radiation (defined in Chapter 1.5.5), I calculate a common electron index of $\delta \approx 2$, with individual values ranging from 2.20 ± 0.08 to 1.68 ± 0.05 . Also plotted in Figure 3.3 are ECMI profiles of Jupiter and Saturn, shifted to the peak flux and frequency of NLTT 33370, which illustrate the sharp cutoff of ECMI with increasing frequency compared with gyrosynchrotron radiation.

The three detected UCDs share two key characteristics: reliably detectable emission at 8.46 GHz and rotation speeds far in excess of the ad hoc 40 km s^{-1} cutoff, where radio emission becomes much more likely (McLean et al., 2011; Pineda, 2017). Previous detections of radio emission from UCDs are generally focused on characterizing the ECMI component (Hallinan et al., 2008), however, the detections presented in this chapter are attributable to gyrosynchrotron radiation. The emission from LSR J1835+3259 and LP 349-25 AB was quiescent over the respective 1-hour and 2-hour observations, with no evidence of flaring or variability. While the emission of NLTT 33370 was mostly quasi-quiescent, the June 12 observations included a massive 20-second burst, with emission over 5 times brighter than the quiescent flux.

The other UCDs in the sample, LP 415-20 and LP 423-31 were not detected. I place 3σ upper flux density limits of $21 \text{ } \mu\text{Jy}$ and $30 \text{ } \mu\text{Jy}$, respectively. LP 415-20 has not been previously observed at low radio frequencies, but its high $v \sin i$ makes the non-detection surprising compared with the other targets and is an important target for follow up. While I did not detect emission at 33 GHz, the slowly rotating LP 423-31 has been observed to have variable and highly polarized emission at 8 GHz (Stelzer et al. in prep, private communication). Taking into account previous

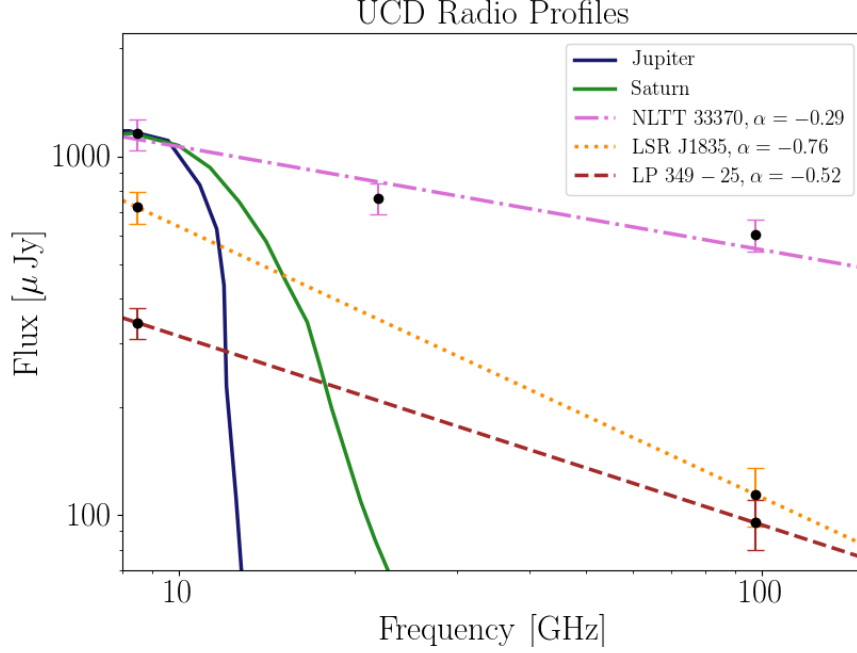


Figure 3.3: Radio emission profiles of all three detected UCDs are shown. The kilometric radiation profiles of Jupiter and Saturn adapted from Zarka (1998) are plotted in blue and green, scaled to the peak flux and frequency of NLTT 33370, whereas the dotted lines correspond to fitted gyrosynchrotron models. The spectral indices of LP 349-25 and LSR J1835-46546 were determined by connecting the two existing data points for each UCD, and were $\alpha = -0.52$ and $\alpha = -0.76$, respectively.

observations at lower frequencies, the lack of 33 GHz emission might suggest that ECMI is present in this object and quiescent gyrosynchrotron is weak or not present at all. However, because previous observations by Berger (2006) at 8.46 GHz have also reported non-detections, additional observations of this target are required to confirm whether it is also variable at high radio frequencies and possibly inactive over the course of the 35 minute observations presented in this work.

Estimating the Size of the Emitting Region

The measured flux can be used to estimate the size of the emitting region in units of Jupiter radii (R_J). Assuming the low frequency limit of $h\nu \ll k_B T$, which is valid for the frequency of observation, the Rayleigh-Jeans law can be rearranged to give,

$$X_{R_J} \approx 1400 \frac{d_{\text{pc}}}{\nu_{\text{GHz}}} \sqrt{\frac{S_{\mu\text{Jy}}}{T_b}}, \quad (3.1)$$

where d_{pc} is the stellar distance, ν_{GHz} is the observing frequency, $S_{\mu\text{Jy}}$ is the flux density, and T_b is the brightness temperature. In the transition region between optically thick and thin regimes, or at the peak emission frequency where $\tau \approx 1$, the brightness temperature is roughly equal to the effective temperature of gyrosynchrotron emission (Equation 1.41). In the case of an isolated source with constant effective temperature, the brightness temperature can be related to the effective temperature by $T_b = (1 - e^{-\tau(\nu)})T_{\text{eff}}$, where $\tau(\nu)$ is the optical depth. This gives the size of the emitting region in the optically thin regime,

$$X_{R_J} \approx 1400 \frac{d_{\text{pc}}}{\nu_{\text{GHz}}} \sqrt{\frac{S_{\mu\text{Jy}}}{(1 - \exp^{-\tau(\nu)})T_{\text{eff}}}}. \quad (3.2)$$

The precise value of the optical depth for gyrosynchrotron emission depends critically on the angle between the magnetic field, the line-of-sight to the observer (Zheleznyakov, 1970), and the frequency of observations.

The size of the emitting region is plotted against magnetic field strength for all three UCDs in Figure 3.3. The solid lines are determined from the previously published ~ 8.5 GHz flux densities of all UCDs. The emitting region is calculated by following Equation 3.1, where I am assuming the observations are at approximately the peak emission frequency where $\tau \approx 1$ and $T_b \rightarrow T_{\text{eff}}$. Taking the average UCD radius to be that of Jupiter (Sorahana et al., 2013), these results show that LP 349-25 and LSR J1835+3259 have emitting regions ranging between the full stellar disc at large magnetic field strengths (~ 2000 G) to a fraction of the stellar disc for low magnetic field strengths. The dotted curves are set assuming the 97.5 GHz flux densities are from regions where $\tau \gg 1$. This provides a lower limit to the size of the emitting region, although we anticipate that the actual size of

the emitting region is closer to that given by the 8.5 GHz observations. Indeed, the higher frequency observations are expected to be from optically thin emission, which would require an optical depth of $\tau \approx 0.0001$ should the 8.5 GHz and 97.5 GHz emission be from the same regions.

The values spanned by this range are consistent with observations of M stars that show significant portions of the disc covered with magnetically active regions (Alekseev and Kozlova, 2002; Johns-Krull and Valenti, 1996), showing a magnetic filling factor - or fraction of surface covered by magnetically active area - significantly higher than Solar values (which are typically $<1\%$). The emitting region for NLTT 33370 is larger than the stellar disc for magnetic field strengths > 100 G. This enhanced emitting region is possibly owing in part to the binarity of the system. If both NLTT 33370 A and NLTT 33370 B are radio loud, then the inferred size of the emitting region includes contributions from both stellar discs and accounts for an additional factor of up to $\sqrt{2}$, but cannot explain the predicted emitting region of NLTT 33370 for magnetic field strengths of ~ 170 G. If the magnetic field strength exceeds this value, the size of the emitting region could be enhanced by the effect of a companion, prompting a significantly larger magnetosphere.

As discussed in Chapter 1.5.5, gyrosynchrotron radiation is likely produced by magnetic reconnection events. In that case, quasi-quiet gyrosynchrotron radiation as is seen in these observations could be the result of small but constant reconnection events due to the twisting and tangling of UCD magnetic fields (Williams et al., 2014). If these reconnection events are similar to Solar reconnection events, they are also likely releasing an outward-directed population of energetic particles, which may have catastrophic effects on planetary atmospheres. A full discussion on energetic particles and planetary habitability is presented in Chapter 5. If gyrosynchrotron radiation is indeed produced by reconnection events and is commonplace around the 10% of UCDs that are radio loud, then it could be indicative of high energetic proton fluxes incident on surrounding planets. Thus, its presence might be an important consideration for modeling of exoplanet atmospheres in orbit around such UCDs. These results also show that if both ECMI and gyrosynchrotron radiation are present in the same target, there must be a magnetic dynamo mechanism that combines the two seemingly at-odds models of UCD magnetic field generation: large scale, axisymmetric dynamos consistent with ECMI

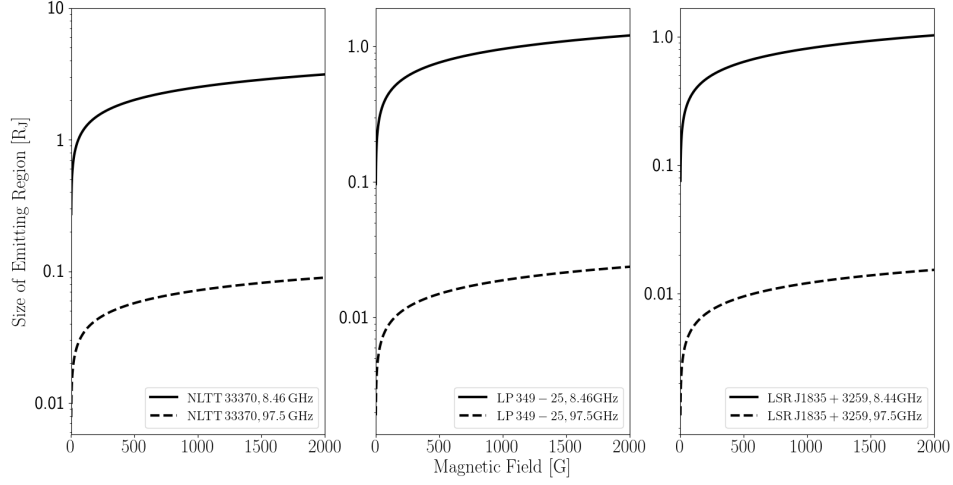


Figure 3.4: The size of the emitting region for a given magnetic field strength for all detected UCDs. The solid curves show the size of the emitting region given ~ 8.5 GHz flux density of each UCD, assuming this is in the transition region where $\tau = 1$. The dotted line at the bottom denotes the minimum size of the emitting region set by assuming the 97.5 GHz observations are in the optically thick regime where $T_b = T_{\text{eff}}$. The size of the emitting region is given in Jupiter radii R_J , characteristic of UCD sizes, while the magnetic field range is chosen to be representative of Solar to typical UCD values. Note that all y-scales are plotted logarithmically and the y-scale for NLTT 33370 extends to larger values than the other UCDs, potentially at least partially owing to contributions from both stars in this binary system or to enhanced magnetospheres due to a companion.

and a non-axisymmetric chaotic fields with breaking and reconnecting magnetic field lines.

There are a few consequences for planets in orbit about UCDs. If the gyrosynchrotron radiation is produced by reconnection events, then the resulting energetic particle flux can threaten the stability of planetary atmospheres. If these detections are instead indicative of synchrotron radiation (Pineda, 2017; Kao et al., 2019), radiation belts could create a plasma environment around the UCD that would require robust planetary magnetic fields for the atmospheres to be stable. Assuming that gyrosynchrotron radiation is the dominant emission mechanism, non-detections can

be used to limit the population of outgoing high-energy protons during potential reconnection events for this scenario. This is explored further in Chapter 5.

3.4 Summary

In this chapter I presented ALMA and VLA observations of five UCDs at radio frequencies from 30 to 100 GHz, where gyrosynchrotron radiation is the preferred emission mechanism. Three UCDs in the survey were found to be active at 97.5 GHz, whereas two were not detected at 33 GHz (LP 423-31) or 97.5 GHz (LP 415-20). This survey quadrupled the number of UCDs detected within this frequency range, with spectral indices ranging from $\alpha = -0.76$ to $\alpha = -0.29$, most consistent with optically thin gyrosynchrotron emission. NLTT 33370 exhibits both minor temporal variability and a strong flare twenty times brighter than the quiescent emission.

Of the non-detections, LP 415-20 is a very rapid rotator that has not previously been observed at radio frequencies. My observations at 33 GHz show it to be radio quiet, consistent with most UCDs but potentially at odds with other rapidly rotating UCDs. LP 423-31 exhibited no detectable high radio frequency emission during the observations. This particular source has been observed twice previously, one of which resulted in a detection (Stelzer et al. in prep, private communication) and the other in a non-detection (Berger, 2006) at low radio frequencies. The presence of variable emission at low radio frequencies and the lack of detectable quiescent emission at high radio frequencies is suggestive of ECMI. However, the low $v \sin i$, uncommon of radio bright UCDs via either emission mechanism, of this source muddles this picture.

These results both suggest that gyrosynchrotron radiation may be ubiquitous in radio loud UCDs, and show the need to observe a larger sample at these frequencies to build meaningful statistics. The presence of gyrosynchrotron emission may indicate that the planetary atmospheres are exposed to damaging energetic particle radiation.

Chapter 4

TRAPPIST-1

This chapter is based on an MNRAS publication (Hughes et al., 2019). It uses ALMA and VLA observations of TRAPPIST-1 to place upper limits on the millimetre flux density of the star. Co-authors on this paper include Aaron Boley, Rachel Osten, and Jacob White.

This chapter also makes use of VLA observations of TRAPPIST-1 to monitor the star for evidence of variability, currently in prep. for publication.

4.1 Background

TRAPPIST-1 (2MASS J23062928-0502285) is an M7.5e star originally discovered by the Two Micron All-Sky Survey in 1999 (Gizis et al., 2000). At a distance of 12.43 ± 0.02 pc (Kane, 2018), luminosity of $5.22 \pm 0.19 \times 10^{-4} L_{\odot}$, and radius of $0.121 \pm 0.003 R_{\odot}$ (Van Grootel et al., 2018), TRAPPIST-1 is not visible to the naked eye. Both its size and its absence of lithium absorption (Reiners and Basri, 2010) indicate that TRAPPIST-1 is a main sequence M dwarf and not a brown dwarf. Furthermore, Reiners and Basri (2010) used FeH absorption lines to determine a surface magnetic field of 600^{+200}_{-400} G. Additional properties are listed in Table 4.1. The star became the centre of attention when it was discovered to be orbited by a system of seven short-period terrestrial planets (Gillon et al., 2017).

In 2015, TRAPPIST-1 was first found to host just three terrestrial planets. This initial discovery was made with TRAPPIST (TRAnsiting Planets and PlanetIsimals

Table 4.1: Stellar Parameters of TRAPPIST-1 taken from the literature.

Parameter	Value	Reference
Mass [M_{\odot}]	0.089 ± 0.006	Van Grootel et al. (2018)
Radius [R_{\odot}]	0.121 ± 0.003	Van Grootel et al. (2018)
T_{eff} [K]	2516 ± 41	Delrez et al. (2018)
P_{rot} [d]	3.295 ± 0.003	Vida et al. (2017)
$v \sin i$ [km s^{-1}]	< 2.0	Reiners et al. (2018)
B [G]	600^{+200}_{-400}	Reiners and Basri (2010)
L_x [$\frac{\text{erg}}{\text{s}}$]	$3.8 - 7.9 \times 10^{26}$	Wheatley et al. (2017)
Age [Gyr]	7.6 ± 2.2	Burgasser and Mamajek (2017)
d [pc]	12.43 ± 0.02	Kane (2018)

Small Telescope), a 60 cm telescope at the La Silla Observatory. The TRAPPIST telescope was given the primary objective of detecting and characterizing exoplanets after Gillon et al. (2016) discovered three planets in orbit around TRAPPIST-1 by observing the small star for a total of 245 hours over the course of 92 days in late 2015. An additional four planets were discovered in 2017 by Gillon et al. (2017) using the Spitzer Space telescope.

The planetary masses were estimated from transit timing variations - small temporal changes in planetary orbits caused by the gravitational pull of planets on one another. All planets in the system were determined to have masses between 0.4 and 1.4 M_{Earth} . Using both 1-dimensional and 3-dimensional climate modeling, Gillon et al. (2017) show that the TRAPPIST-1 e, f, & g all likely have the appropriate surface temperatures for liquid water, whereas the inner TRAPPIST-1 planets TRAPPIST-1 b, c, & d are likely too close to the star to avoid a runaway greenhouse effect, and the orbit of TRAPPIST-1 h is likely too distant for it to maintain an equilibrium temperature above 273 K. Subsequent work including the impact of vegetation on planetary albedo suggests that TRAPPIST-1 d may also be an appropriate temperature to support liquid water (Alberti et al., 2017).

With an effective temperature of 2511 ± 37 K (Delrez et al., 2018), the habitable zone of TRAPPIST-1 is significantly closer to the star than for Solar type stars. All orbits of the TRAPPIST-1 planets are within 0.06 au, with a habitable zone encompassing TRAPPIST-1e, f, and g and the closest nominally habitable planet located just 0.02 au from the star. Due to this proximity, the planets are likely

tidally locked (Gillon et al., 2017), and as such they are unlikely to have intrinsic protective magnetic fields needed to deflect incident energetic particles. Even worse, Garraffo et al. (2017) find that all but the outermost TRAPPIST-1 planets cross into the Alfvén surface of TRAPPIST-1’s stellar magnetosphere, where the planets are subjected to severe space weather events. Between all of these factors, the TRAPPIST-1 planets are particularly vulnerable to damaging stellar particle radiation.

4.2 Introduction

The discovery of its extensive planetary system and the potential for hosting ex-traterrestrial life made TRAPPIST-1 a high-interest star for astronomers, and a primary target for early JWST Guaranteed Time Observing programs to investigate the planetary atmospheres. Astronomers have also been particularly interested in the stellar activity and the impacts it could have on the surrounding planets. TRAPPIST-1 has been observed across the electromagnetic spectrum, and found to have a photometric flare rate of 0.38 flares per day (Vida et al., 2017) and $L_X/L_{\text{bol}} \sim 10^{-4}$ (Wheatley et al., 2017). However, UV flares alone are not a death sentence for life on surrounding planets, and UV emission could even aid in the development of life (e.g., Sagan and Khare, 1971; Sarker et al., 2013; Ranjan and Sassellov, 2016). Simulations (discussed in detail in Chapter 5) have shown that high-energy particles, rather than flares or UV emission alone, pose the biggest threat to the stability of planetary atmospheres. In this chapter, I use the ALMA and VLA radio telescopes to search for evidence of gyrosynchrotron radiation as evidence for these particles.

Gyrosynchrotron radiation released during magnetic reconnection events can be used as a tracer of outgoing energetic particles. Reconnection events can manifest in explosive flares and bursting radio emission, or potentially in smaller but ubiquitous reconnection events producing quiescent radio emission in the case of radio loud UCDs (Williams et al., 2014). As discussed in Chapters 1 and 3, stellar non-thermal emission present at frequencies between 1 and 100 GHz for typical UCD magnetic field strengths is attributed to gyrosynchrotron radiation, which can probe stellar activity close to the photosphere and constrain the size of radio emitting region

and magnetic field strength. While X-ray and γ -ray observations can determine accelerated particle populations in Solar magnetic events, observations at high radio frequencies where gyrosynchrotron emission is dominant are one of the only ways to constrain the population of accelerated particles in UCDs. A flux measurement of gyrosynchrotron radiation from a UCD can, in turn, be used to estimate the energetic proton flux incident on surrounding planets. A non-detection can also be used to place upper limits and constrain particle fluxes.

In this chapter I present ALMA and VLA observations of TRAPPIST-1 at 97.5 and 44 GHz respectively, frequencies at which gyrosynchrotron radiation could be present (Dulk, 1985), but not likely other types of significant radio emission. Observations of UCDs at such high radio frequencies are scarce. TVLM 513-46546 and the three detected targets presented in Chapter 3 are the only UCDs to be detected in the 45 – 100 GHz range, with quiescent emission attributed to gyrosynchrotron radiation (Williams et al., 2015). The aim of these observations was to determine whether TRAPPIST-1 has comparable radio emission and to make a connection between that emission or upper limit and the particle flux incident on planets. Scaling the TVLM 513-46546 flux measurements to the size and distance of TRAPPIST-1, the expected emission would be 45 μ Jy at 100 GHz, and 60 μ Jy at 45 GHz if TRAPPIST-1 is emitting gyrosynchrotron radiation of identical strength. The on-source observation times were chosen in order to achieve a signal-to-noise ratio of 10 for each observation. The source was not detected at either frequency, which I use to place upper limits on the quiescent flux of TRAPPIST-1 in both cases, constrain the properties of any radio emitting region, and put TRAPPIST-1 in the context of UCD radio emission. In Chapter 5 I use the upper level flux to place limits on inferred outgoing energetic proton populations from the star, and put this in the context of planetary habitability.

4.3 Observations

The 97.5 GHz ALMA and 44 GHz VLA observations were centred on TRAPPIST-1 using J2000 coordinates $RA = 23^h 06^m 29.37^s$ and $\delta = -05^d 02^m 29.03^s$. The data from both facilities were reduced using the Common Astronomy Software Applications (CASA) pipeline CASA v5.1.2 (McMullin et al., 2007) and are described

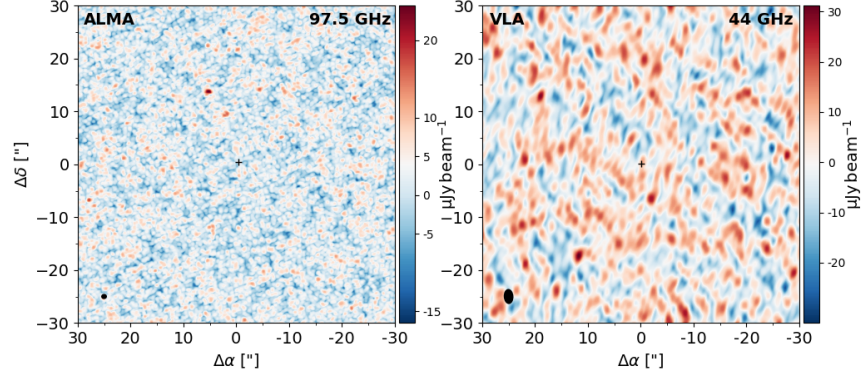


Figure 4.1: Continuum images showing the $60'' \times 60''$ region around the positions of TRAPPIST-1 for my 97.5 GHz ALMA (left) and 44 GHz VLA (right) observations. The crosses at the centres of both images indicate the position of TRAPPIST-1. The synthesized beam is indicated by the black ellipses in the lower left of each image. TRAPPIST-1 was not detected, with RMS sensitivities of $5.34 \mu\text{Jy}$ and $3.52 \mu\text{Jy}$ in my VLA and ALMA observations, respectively. The brighter of the two unresolved bright spots in the ALMA image located to the NE of TRAPPIST-1 is likely a background object, whereas the other can be attributed to Gaussian noise.

Table 4.2: 3σ upper flux and radio luminosity limits on TRAPPIST-1. The 6 GHz observations are from Pineda and Hallinan (2018).

Frequency [GHz]	Flux [μJy]	$L_{\nu,R}$ [$\text{erg s}^{-1} \text{Hz}^{-1}$]	Ref.
6	<8.1	$<1.5 \times 10^{12}$	Pineda and Hallinan (2018)
44	<16.2	$<3.0 \times 10^{12}$	This work
97.5	<10.6	$<2.0 \times 10^{12}$	This work

below.

4.3.1 ALMA Observations

The ALMA Cycle 5 observations (ID 017.1.00986.S, PI Hughes) were taken in 8 executions blocks (EBs) from 2018 January 22 to 2018 January 28 for a total of

8.83 hr including overhead and 6.41 hr on-source. There were 43 antennas used with baselines ranging from 15 m to 1397 m.

Observations were in Band 3 with a total bandwidth of 8 GHz split among 4 spectral windows (SPW). Each SPW has 128×15.625 MHz channels for a total bandwidth of 2 GHz. The SPWs were centred at 90.495 GHz, 92.432 GHz, 102.495 GHz, and 104.495 GHz, giving an effective continuum frequency of 97.50 GHz. The data were reduced using CASA 4.7.2, which included WVR calibration; system temperature corrections; flux and bandpass calibration with quasar J0006-0623; and phase calibration with quasar J2301-0158. The precipitable water vapour (PWV) ranged from 1.7 mm to 7.15 mm throughout the observations.

The ALMA 97.5 GHz observations have a RMS sensitivity of $3.52 \mu\text{Jy beam}^{-1}$ as taken from the CLEANed image. The size of the resulting synthesized beam is $0.835'' \times 0.738''$ at a position angle of -86.4° , corresponding to 10 au at the system distance of 12.45 pc.

4.3.2 VLA Observations

The observations were taken during the VLA Semester 18A (ID VLA-18A-327, PI Hughes) over 4 scheduling blocks (SBs) from 2018 September 4 to 13 for a total of 8.29 hr including overhead and 7.20 hr on-source. Data were acquired with the array in the D antenna configuration, with 26 antennas and baselines ranging from 35 m to 1030 m.

The instrument configuration used the Q band receiver with a correlator setup consisting of 3968×2.0 MHz channels for a total bandwidth of 7.936 GHz. Four separate basebands were used with rest frequency centres at 41 GHz, 43 GHz, 45 GHz, and 47 GHz giving an effective continuum frequency of 44.0 GHz. The quasar J2323-0317 was used for gain and phase calibration and quasar 3C48 was used as a bandpass and flux calibrator. Data were reduced using the (CASA 5.1.2) pipeline, which included bandpass, flux, and phase calibrations.

These VLA 44.0 GHz observations achieve a RMS sensitivity of $5.39 \mu\text{Jy beam}^{-1}$ as taken from the CLEANed image. The size of the synthesized beam is $2.58'' \times 1.53''$ at a position angle of -86.4° . The beam size corresponds to 26 au at the system's distance.

4.3.3 Null detections of TRAPPIST-1

Our 44 GHz VLA and 97.5 GHz ALMA observations were both non-detections, with 3σ upper limits of $16.2 \mu\text{Jy}$ and $10.6 \mu\text{Jy}$ respectively (Table 4.2). I confirmed that the phase centre is at the expected location of TRAPPIST-1, taking into account proper motion.

To ensure that weak variability is not present, I analyzed each observation's individual scans, which are ~ 4 minutes for the VLA observations and ~ 7 minutes for the ALMA data. I found no evidence of flaring or variability at median 3σ upper limits of $110 \mu\text{Jy}$ and $190 \mu\text{Jy}$ per scan for ALMA and the VLA, respectively.

There are two unresolved bright source candidates in the ALMA image located to the NE of TRAPPIST-1. They are absent in the VLA observations, and I was not able to identify the object candidates in source catalogues. The brighter candidate has a flux of $24 \mu\text{Jy}$. and the fainter has a flux of $16 \mu\text{Jy}$. This corresponds to SNRs of 6.8 and 4.5, respectively. The significance of this is tested by producing 10^4 images of Gaussian noise and convolving those images with the synthesized beam. A 4.5σ peak was found in 16% of the realisations, while a 6.8σ peak did not occur, implying we should expect such a peak less than 0.01% of the time. Based on this, the 6.8σ source is likely real, while the 4.5σ source may just be noise.

4.4 TRAPPIST-1 in the Context of UCD Radio Emission

Previous 6 GHz observations by Pineda and Hallinan (2018), unpublished prior to the ALMA observations in this work, also did not detect TRAPPIST-1 with a 3σ upper limit of $8.1 \mu\text{Jy}$. This, along with the observations presented in this work, demonstrates that the radio emission of TRAPPIST-1 is in line with what would be expected given its X-ray luminosity and rotation rate.

While the observations presented in this work are at 44 and 97.5 GHz, I briefly consider lower frequencies to provide context for further discussion of TRAPPIST-1. The Güdel-Benz relation between the X-ray and radio luminosity of magnetically active stars (discussed in Chapter 1) suggests that TRAPPIST-1 should be radio quiet unless it is part of the $\sim 10\%$ of radio bright UCDs that violate the GBR. TRAPPIST-1's position along the GBR with X-ray luminosity from Wheatley et al. (2017) and upper limit on 6 GHz emission from Pineda and Hallinan (2018) is

shown in Figure 1.5. At 6 GHz, the dominant emission mechanism is expected to be ECMI as opposed to gyrosynchrotron radiation. The high radio frequency observations presented here can better constrain the size of the emitting region and estimate accelerated particle populations.

Despite scarce data, a few trends have been noted in UCD radio emission. There appear to be two distinct populations of UCDs determined by X-ray luminosity and projected rotation speed: X-ray bright and slowly rotating UCDs tend to be radio dim, while X-ray dim and rapidly rotating UCDs are more likely to have radio emission that exceeds the GBR (Williams et al., 2014; Cook et al., 2014). All objects that deviate very strongly have $v \sin i \geq 20 \text{ km s}^{-1}$, although the reverse is not true. This is seen in both previously published work as well as my observations of the three UCDs presented in the previous chapter.

This bimodal behaviour is different from early- and mid- M dwarfs, which can exhibit significant activity and correlate with the GBR. The difference could be related to the change in magnetic field generation at the onset of full convectivity. As discussed in Chapter 1, late-type M dwarfs are fully convective, and thus unable to generate magnetic fields via the same mechanisms as Solar-type stars, which are thought to rely heavily on the shear between convective and radiative layers (Spiegel and Zahn, 1992). Prior to the development of highly sensitive radio telescopes, it was not guaranteed that convective stars and brown dwarfs would be capable of producing significant magnetic activity at all (Fleming et al., 2000; Linsky et al., 1994; Reid et al., 1999). However, in some cases for which the magnetic fields of UCDs have been measured, field strengths can reach up to kG levels (Reiners and Basri, 2010), a thousand times stronger than that of the Sun. While UCDs are unable to generate magnetic fields via the same mechanism as the Sun, there must be some convective dynamo at play.

It is unclear why there are two different populations of UCDs. The UCD branch cannot be explained through variability, as the same break is seen in simultaneous X-ray and radio observations of UCDs (Williams et al., 2014; Berger et al., 2008a; Williams et al., 2015), including during flares. A few models exist to explain UCD magnetic field generation and corresponding radio emission. For example, Hallinan et al. (2007) and Pineda (2017) argue that radio emission due to ECMI requires global, dipolar magnetic fields. In the case of gyrosynchrotron radiation,

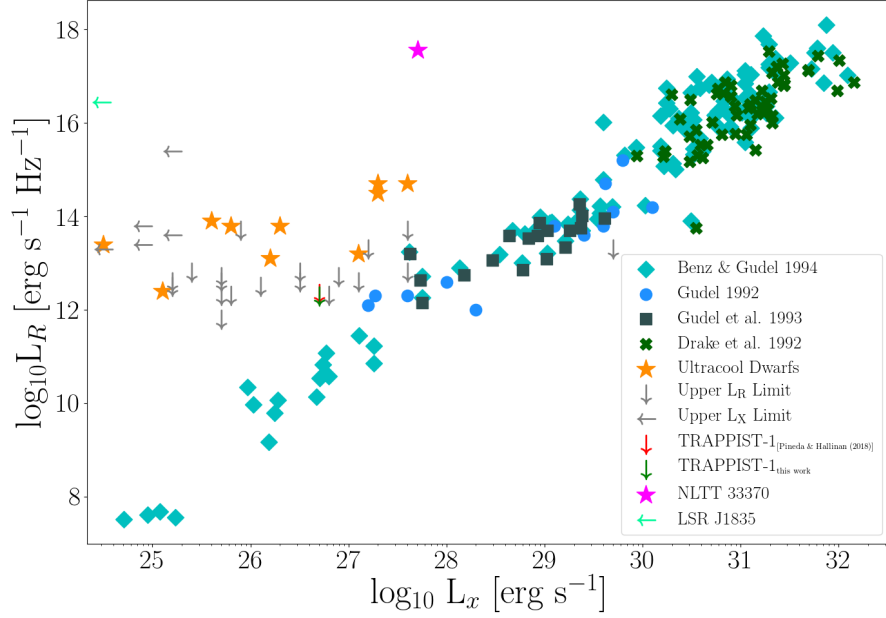


Figure 4.2: The Güdel-Benz relation between X-ray and $\sim 5 - 9$ GHz radio luminosity. Blue diamond data points represent Solar flares from Benz and Güdel (1994), green ‘x’ and blue circles represent magnetically active F, G, & K stars (Güdel, 1992; Drake et al., 1992). Dark green squares represent mid- to late-M dwarfs in line with the GBR (Güdel et al., 1993), whereas the orange stars show a population of ultracool dwarfs in violation of the GBR. Grey arrows show upper-limits on X-ray and/or radio luminosities of UCDs. TRAPPIST-1 is shown along the GBR with a red arrow. The upper limit in this plot uses the 6 GHz VLA observations by Pineda and Hallinan (2018) and the X-ray luminosity measured by Wheatley et al. (2017). Uncertainties are not plotted but are typically within 10%. Two of the detected UCDs presented in the previous chapter, NLTT 33370 and LSR J1835, with previously measured X-ray luminosity are shown as well (Berger et al., 2008a; Williams et al., 2015).

Williams et al. (2014) propose that the magnetic field topology, rather than strength, is responsible for the presence of radio emission. The divergence in M dwarf behaviour would be the result of two distinct magnetic modes possible in M dwarf populations, where late-type M dwarfs are able to inhabit either mode (Morin et al., 2010). In this bimodal dynamo model, whichever magnetic mode a UCD has is loosely dependent on its rotation rate (McLean et al., 2012). In the absence of photometric light curves for most UCDs, $v \sin i$ is used rather than the rotation period.

Slowly rotating UCDs ($v \sin i \leq 10 \text{ km s}^{-1}$) tend towards axisymmetric dynamos and strong magnetic fields (Stelzer et al., 2012), whereas rapidly rotating UCDs ($v \sin i \geq 20 \text{ km s}^{-1}$) are capable of having either an axisymmetric or non-axisymmetric dynamo and any strength field. Each dynamo creates a distinct field topology, which determines the radio behaviour of the star.

In their model, Williams et al. (2014) posit that UCDs with axisymmetric dynamos have radio emission in agreement with the GBR, whereas the outlying higher radio emission comes from UCDs with weak non-axisymmetric dynamos. Frequent low-energy magnetic reconnection events due to the tangled multi-polar fields in non-axisymmetric dynamos accelerate electrons along field lines, producing both quiescent and bursting gyrosynchrotron emission at radio frequencies (Berger et al., 2008a).

I find TRAPPIST-1 to be consistent with the trends seen in other UCDs. With $v \sin i < 6 \text{ km s}^{-1}$ and $L_x \sim 10^{26} \text{ erg s}^{-1}$, it is expected to have negligible radio emission. The position of TRAPPIST-1 on the GBR is shown in the bottom panel of Fig. 4.2. If the emission is below the telescope sensitivity, then TRAPPIST-1 could be in line with the trend for radio quiet UCDs.

While an emission mechanism cannot be inferred from only non-detections, a particular emission mechanism can be adopted to calculate some potential constraints on the system. Pineda and Hallinan (2018) focused on ECMI, and this work complements that discussion by focusing on gyrosynchrotron emission. First, following the framework of White et al. (1989) and Osten et al. (2009) used in Chapter 3, I calculate the size of the emitting region in units of Jupiter radii in the Rayleigh-Jeans limit using Equation 3.1 and assuming, for a limiting case, that the brightness temperature is equal to the effective temperature. I otherwise use the

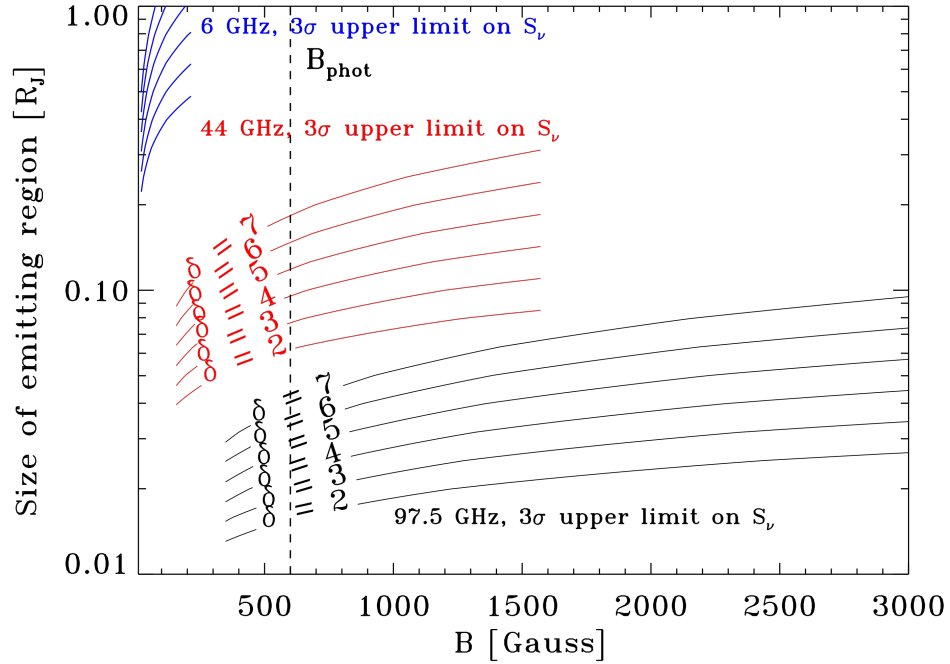


Figure 4.3: Constraints on the size of the emitting region and magnetic field strength for an assumed electron energy index δ in the optically thick gyrosynchrotron regime following Equation 3.1. In the case of optically thin emission, the emitting region can be enhanced by up to 10 for an optical depth $\tau(\nu) = 0.01$. The upper blue curves are set by the 6 GHz VLA observations presented in Pineda and Hallinan (2018), while the red and black curves are set by the 44 GHz VLA and 97.5 GHz ALMA observations presented in this work. The vertical black dotted line shows the magnetic field strength determined by Reiners and Basri (2010).

equations in Dulk (1985) appropriate for the optically thin regime. Fig. 4.3 shows the range of x values set by each radio observation of TRAPPIST-1 for an assumed electron energy index and magnetic field strength. For a magnetic field of 600 G and electron energy index $\delta = 2$, the emitting region is constrained by my ALMA upper limits to $\leq 0.02 R_J$.

This upper limit is significantly smaller than the constraints placed on the radio bright UCD NLTT 33370 presented in the previous chapter, and just smaller than

values for LP 349-25 and LSR J1835 at the same magnetic field strength (600 kG). If TRAPPIST-1 does have a gyrosynchrotron-emitting region, these results show that it must be substantially smaller than what is found for radio bright UCDs. Deeper constraints on the flux density could further limit this value, but the current limit can be used to infer upper limits on the outgoing high energy particle population incident on the TRAPPIST-1 planets, discussed in the next chapter.

4.5 Monitoring Campaign of TRAPPIST-1

While my (<10 hr) ALMA and VLA observations placed tight constraints on the possible quiescent radio emission of TRAPPIST-1, this cannot rule out whether the star exhibits bursting or variable emission only apparent over longer time periods. As noted, TRAPPIST-1 is known to flare, showing that the star exhibits some degree of transient magnetic activity at least at optical wavelengths. I successfully observed TRAPPIST-1 with the VLA for nearly 40 hours on-source to look for indications of bursting or flaring radio activity near the cyclotron frequency. In this frequency range, emission could be prompted by either ECMI or gyrosynchrotron radiation, produced in flares, CMEs, or other variable processes missed by short-term observations.

Optical light flares on TRAPPIST-1 have been observed with both the Trappist telescope and K2 (Gillon et al., 2016; Vida et al., 2017), but it is unclear what causes these flares or the extent to which the flares impact the space weather environment around the star. As discussed, Solar flares are generated through magnetic reconnection events, which produce radiation across the electromagnetic spectrum through bremsstrahlung, gyrosynchrotron, synchrotron, and plasma emission. However, it is unknown whether UCD flares behave like Solar flares; the Sun may indeed be a poor model. For example, the flares of the UCD Proxima Centauri are Solar-like in temperature and density at X-ray wavelengths, but MacGregor et al. (2018) measured a radio flare that was $10\times$ the maximum luminosity of Solar flares. This “mega-flare” could indicate that the radio emission during UCD flares is significantly stronger than that of Sun-like stars. This could, in turn, be indicative of more severe space weather. If TRAPPIST-1 does behave similarly to the Sun, then accompanying radio emission would be too faint to detect during flares. On the

other hand, if TRAPPIST-1 behaves like the more analogous star Proxima Centauri, its flares would be bright enough for the VLA to measure at 3 GHz.

The 3.3 day rotation period of TRAPPIST-1 corresponds to periodic fluctuations in brightness seen in K2 data (Luger et al., 2017). While these modulations are thought to be due to surface features, it is unclear whether starspots or hotspots are rotating into and out of view. Morris et al. (2018) find that the light curves are more consistent with hot spots. Since brighter regions coincide with more frequent flaring, the two may be due to the same magnetic events. Morris et al. (2018) note that the 3.3 day periodicity could instead be caused by the changing size of surface bright spots rather than stellar rotation. Radio observations could capture flares concentrated around hot spots and constrain the hot spot size, energy, and magnetic field strength. If no radio emission is present at all, changing surface morphology rather than modulation of starspots could be the origin of the observed periodicity, or the radio emission accompanying hot spots is of lower magnitude than the Proxima Centauri flare.

Without any previous radio detections of TRAPPIST-1, it is difficult to estimate the star’s radio brightness during a flare or other variable outburst. If TRAPPIST-1 has radio emission during flares similar to the quiescent gyrosynchrotron emission of known radio bright UCDs, the flux density scaled to the distance of TRAPPIST-1 should be around 140 μ Jy. This is a low estimate, however, as UCD radio outbursts are significantly brighter than their quiescent radio emission.

4.5.1 Observations

The 3 GHz VLA observations (Figure 4.4) were centred on TRAPPIST-1 using J2000 coordinates $RA = 23^h 06^m 29.37^s$ and $\delta = -05^d 02^m 29.03^s$. The data were reduced using the Common Astronomy Software Applications (CASA) pipeline CASA (v5.1.2; McMullin et al. (2007)).

The observations were taken during the VLA Semester 19A (ID VLA-19A-215, PI Hughes) over 58 scheduling blocks (SBs) from 2019 April 8 to July 24 for a total of 49.99 hr including overhead and 39.0 hr on-source. Data were acquired with the array in the B antenna configuration, with 37 antennas and baselines ranging from 35 m to 1030 m.

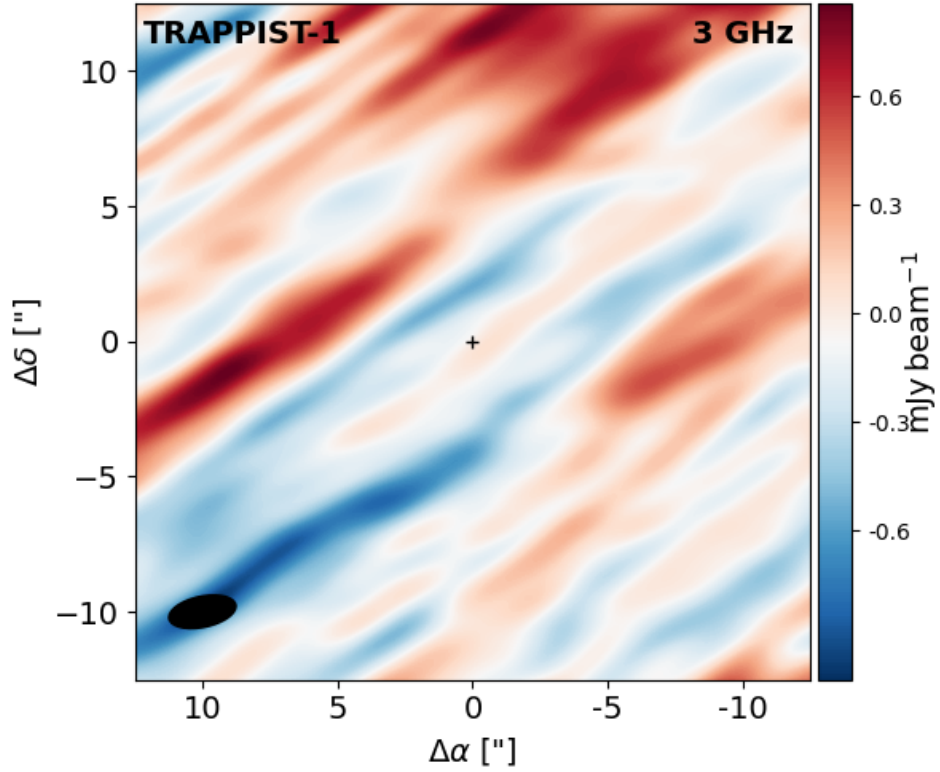


Figure 4.4: Continuum image showing the $12'' \times 12''$ region centred on the sky position of TRAPPIST-1 for my 3 GHz VLA observations. The crosses at the centre of the image indicate the position of TRAPPIST-1. The synthesized beam is indicated by the black ellipse in the lower left of the image. TRAPPIST-1 was not detected, with RMS sensitivity of $170 \mu\text{Jy}$. The streaking structure that resembles telescope tracking is due to artefacts introduced by the quasar.

The instrument configuration used the S band receiver with a correlator setup consisting of 1224×2.0 MHz channels for a total bandwidth of 2.08 GHz. Spectral windows of 64-channel width had bandwidths ranging from 1.988 GHz to 3.884 GHz, giving an effective continuum frequency of 2.9 GHz. The quasar J2246-1246 was used for gain and phase calibration and quasar 3C48 was used as a bandpass and flux calibrator. Data were reduced using the (CASA 5.1.2) pipeline, which included bandpass, flux, and phase calibrations.

These VLA 2.9 GHz observations achieve a RMS sensitivity of $170 \mu\text{Jy beam}^{-1}$ as taken from the CLEANed image, insufficient to reveal a weak detection. The size of the synthesized beam is $2.52'' \times 1.14''$ at a position angle of -78.1° . The beam size corresponds to 22 au, or a beam radius of 11 au, at the system's distance of 12.1 pc.

In addition to the non-detection produced by stacking the observations of TRAPPIST-1, I saw no evidence of emission throughout any of the 58 SBs. This indicates the star may not be variable or flaring, or that the flares are strongly “concentrated” and modulated with the rotation period of the star.

These observations were complicated by the presence of a bright quasar in one of the side lobes that introduced significant artefacts into the image (Figure 4.5). This can be accounted for in the self-calibration process. However, the presence of the quasar increases the RMS of the observations by an order of magnitude. Removing the quasar from these observations to improve the RMS and place deep 3 GHz constraints on the radio emission of TRAPPIST-1 is part of my ongoing work before these observations are published.

4.6 Summary

In this chapter I presented observations of the UCD TRAPPIST-1. I observed the star at 97.5 GHz with ALMA and at 44 GHz with the VLA to measure the quiescent flux density, and monitored the star at 3 GHz with the VLA for signatures of variability. I find non-detections of the quiescent flux at both 97.5 GHz with a 3σ upper level flux limit of $10.6 \mu\text{Jy}$ and at 44 GHz with a 3σ upper level flux limit of $16.2 \mu\text{Jy}$. The individual scans showed no signs of variability over the course of the 97.5 and 44 GHz observations.

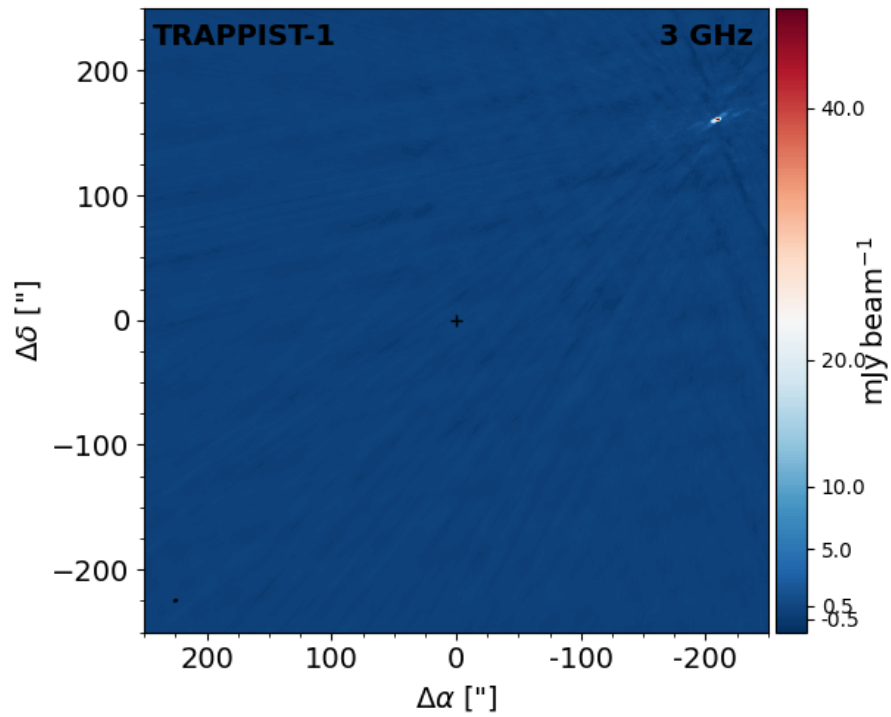


Figure 4.5: Wide-field continuum image showing the $240'' \times 240''$ region centred around the sky position of TRAPPIST-1 for my 3 GHz VLA observations. The crosses at the centre of the image indicate the position of TRAPPIST-1. The synthesized beam is indicated by the black ellipse in the lower left of the image. This image is significantly zoomed out in order to show the bright quasar, seen in the top right, that introduced significant noise-like artefacts into the observations and raised the RMS.

From these observations, TRAPPIST-1 conforms to trends in UCD radio brightness; slowly rotating UCDs with high X-ray emission are unlikely to be detected at radio frequencies, whereas rapidly rotating UCDs with low X-ray emission are more likely to be radio bright. TRAPPIST-1 has a long rotation period of 3.295 ± 0.003 days and high X-ray luminosity of $3.8 - 7.9 \times 10^{26} \text{ erg s}^{-1}$, making these results consistent with the GBR. I also presented preliminary results from my monitoring campaign of TRAPPIST-1, which included 39 hours of on-source observations to search for transient bright radio activity near the cyclotron frequency. The presence of a radio bright quasar in one of the sidelobes introduces a strong noise-like signal into the observations, lowering the RMS substantially. Additional analysis is necessary prior to the publication of these results, described in Chapter 6.

Chapter 5

Ultracool Dwarf Magnetism and Habitability

Among the interesting consequences of stellar magnetic activity is the impact of that activity on surrounding planets. Exoplanet surveys have shown that M dwarfs are frequent hosts of close-orbiting terrestrial planets, making their activity of particular importance in the context of habitability. Dressing and Charbonneau (2015) estimate an occurrence rate of about 0.5 Earth-like planets per M dwarf habitable zone, where this habitable zone has conventionally been defined as the orbital distance around a host star where an Earth-like planet would be within the right equilibrium temperature range to support liquid water on its surface.

While the equilibrium temperature of a planet is important to harboring Earth-like life, atmospheric chemistry and surface life can also be impacted by stellar magnetic activity and variability. This point is particularly crucial for planets in orbit around low-mass stars. Due to low stellar temperatures, the habitable zone of cool stars is located at much smaller stellocentric distances (e.g. Figure 5.1). This leaves planets vulnerable to both a higher degree of activity from the star and stronger tidal forces that could lead to spin-orbit resonances or tidal locking in extreme cases (Barnes, 2017).

The precise impacts of stellar emission on “habitable” planets are not straightforward and depend on many unknowns about both the planets and their host stars. Heightened magnetic activity typical of M dwarfs may not actually be prohibitive

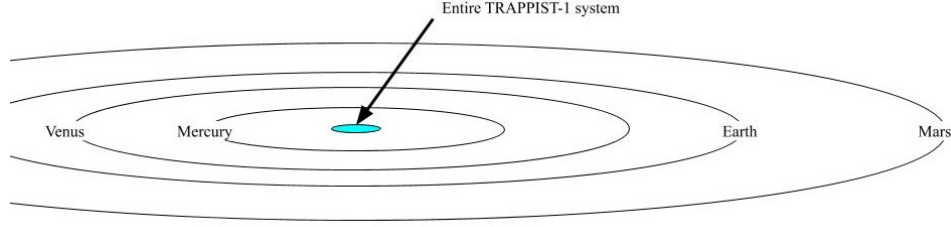


Figure 5.1: Diagram comparing the orbits of the inner Solar System planets, with semi-major axes ranging from 0.38 – 0.72 au to the TRAPPIST-1 planetary system, with semi-major axes ranging from 0.01 – 0.06 au.

to the development and survival of surface life. UV radiation may even aid in the development of life, as noted in Section 1.5.6, and when unaccompanied by other radiation it may not be enough to significantly impact planetary atmospheres.

5.1 The Habitable Zone

Unlike TRAPPIST-1, none of the UCDs presented in my survey have known orbiting exoplanets, let alone known planets with the potential to harbour life under Earth-like conditions. To determine the particle flux incident on hypothetical habitable planets around each UCD, I first estimate the location of the habitable zone around each star. The habitable zone is not well defined, as there are many factors to consider: the received radiation, atmospheric composition, oceanic circulation, etc. Moreover, definitions based on surface temperatures ignore the possibility of subsurface life subsisting on an internal energy source (e.g. Stevenson (2018); Tasker et al. (2017)). For the purposes of this calculation with these caveats in mind, I use the equilibrium temperature definition of the habitable zone. Specifically, I consider the orbital region around a star where a planet with an Earth-like albedo of $A = 0.3$ and emissivity $\epsilon = 0.9$ has an equilibrium temperature within the range $273 \text{ K} < T < 373 \text{ K}$ necessary for liquid water (Hart, 1980). I also consider an insolation definition of the habitable zone, but the inner and outer limits do not deviate significantly enough from the equilibrium temperature definition, and are ultimately not used in my calculations.

Table 5.1: Properties of UCDs included in the survey, all presented in Chapter 3, that are used in the energetic particle flux estimates.

Target Name	S (μJy)	α	δ	R (R_J)	T (K)
LSR J1835	114	-0.76	2.2	0.04	2800
LP 349-25	70	-0.52	1.9	0.05	2400
NLTT 33370	600	-0.29	1.7	0.2	3200

The equilibrium temperature can be calculated by equating the incoming stellar radiation incident on a planet with the outgoing radiation, assuming the planet and star radiate as a blackbody. The star-facing hemisphere of a planet will receive stellar radiation given by,

$$P_{\text{in}} = (1 - A) \frac{L_{\star}}{4\pi a^2} \pi R^2, \quad (5.1)$$

where A is the albedo of the planet, R is the planet radius, and a is the semi-major axis. Correspondingly, the planet re-radiates from its entire surface by,

$$P_{\text{out}} = 4\pi R^2 \epsilon \sigma T^4, \quad (5.2)$$

where T is the temperature of the planet, ϵ is the emissivity, and σ is the Stefan-Boltzmann constant. Equating the incoming stellar radiation with the radiation emitted by the planets and solving for the temperature in equilibrium, T_{eq} ,

$$T_{\text{eq}} = \left[\frac{(1 - A)L_{\star}}{16\pi a^2 \epsilon \sigma} \right]^{1/4}. \quad (5.3)$$

Using the Stefan-Boltzmann law between stellar luminosity and temperature, $L_{\star} = 4\pi \sigma R_{\star}^2 T_{\star}^4$,

$$T_{\text{eq}} = T_{\star} \left(\frac{1 - A}{\epsilon} \right)^{1/4} \sqrt{\frac{R_{\star}}{2a}}. \quad (5.4)$$

Re-arranged to solve for the semi-major axis a ,

$$a = \sqrt{\frac{1-A}{\epsilon}} \frac{R_{\star} T_{\star}^2}{2 T_{\text{eq}}^2}. \quad (5.5)$$

To get an estimate of the proton flux on a planet within this range, I use the median temperature required for liquid water as the planetary equilibrium temperature, $T_{\text{eq}} = 323$ K and stellar radius $R_{\star} = R_{\text{J}}$. The habitable zones for each UCD, including the inner and outer limits, are shown in Table 5.2.

As noted above, the habitable zones can be alternately defined in relation to the insolation only, or comparison between the stellar and Solar luminosity L_{\star}/L_{\odot} . The inner and outer edges of the habitable zones in this definition are a'_{in} and a'_{out} . Following the work of Lunine et al. (2008) and Turnbull et al. (2012), they are expressed,

$$a'_{\text{in}} = 0.75 \text{ au} \sqrt{\frac{L_{\star}}{L_{\odot}}}, \quad (5.6)$$

and

$$a'_{\text{out}} = 1.8 \text{ au} \sqrt{\frac{L_{\star}}{L_{\odot}}}, \quad (5.7)$$

respectively. Under these definitions, the locations of the inner and outer habitable zones vary only slightly from the equilibrium temperature estimates shown in Table 5.2; with NLTT 33370 now predicted to have a habitable zone range from 0.013 - 0.031 au. Given that these habitable zone estimates are so similar to the equilibrium temperature values, I do not give them further consideration.

The short orbital distances involved in the habitable zones around UCDs expose planets to heightened levels of stellar activity. In this work, I am particularly concerned with the outgoing energetic particle flux - predominantly energetic protons - thought to accompany reconnection events traceable at GHz radio frequencies.

5.2 Particle Flux in Context

The impact of stellar particle flux estimates can be understood in the context of Solar storms. Typically, Solar energetic particles (SEPs) have low enough energy that they are deflected by the Earth's magnetic field. However, Solar flares and

Table 5.2: The locations of the habitable zone as determined from the equilibrium temperature around each UCD presented in Chapter 2. The average values, bolded in column 2, are used for the primary particle flux estimates. The inner a_{in} and outer a_{out} ends of the habitable zone are used to calculate the extremes of particle flux values.

	a_{in} (au)	a_{avg} (au)	a_{out} (au)
LSR J1835	0.012	0.016	0.021
LP 349-25	0.008	0.012	0.016
NLTT 33370	0.016	0.019	0.028

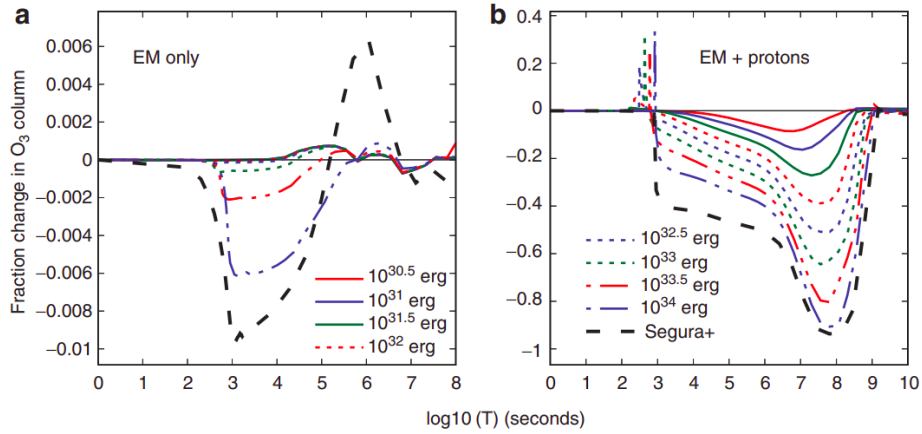


Figure 5.2: The plot from Tilley et al. (2017) on the left (a) shows the effects of an electromagnetic radiation only single flare on the ozone column on an Earth-like atmosphere, while the plot on the right (b) shows the effects of the same flare with the addition of energetic proton fluxes ranging from $\sim 3 \times 10^5$ pfu for the $10^{30.5}$ erg flare to $\sim 6 \times 10^8$ pfu for a 10^{34} erg flare. Note the split legend. Used with permissions under the Creative Commons CC-BY-NC license.

coronal mass ejections accelerate particles to sufficiently high energies to penetrate into the polar ionosphere. During strong Solar storms, energetic protons can cause dangerous levels of radiation for airplanes near the poles and astronauts outside of the Earth's magnetosphere, but increases in radiation on the ground due to secondary neutrons are rare.

The damaging effects of energetic particle radiation on Earth-like atmospheric chemistry are unambiguous. Incident high energy protons released during Solar particle events (SPEs) ionize molecules in the Earth's stratosphere and mesosphere. This ionisation results in enhancements in nitric oxides (NO_y) and hydrogen oxides (HO_x), both of which are seen to increase during large SPEs (e.g., Storini and Damiani, 2008; Gerard and Barth, 1977; Iwagami and Ogawa, 1980). Ozone, or O_3 , reacts through a few catalytic cycles with nitric and hydrogen oxides in the hours following an event (Jackman et al., 2005), causing a measurable depletion in local ozone levels. Even the global ozone content is impacted by Solar activity, and is seen to vary with the same periodicity as the Solar cycle with an amplitude of roughly $1.8 \pm 0.3\%$ (Hood and McCormack, 1992). Radiocarbon signatures indicate that a very strong SPE occurred in 775 AD (Usoskin et al., 2013), leading to an estimated 8.5% depletion in total ozone (Sukhodolov et al., 2017). While ozone depletion in the Earth's atmosphere due to SPEs has consequences for surface life, including making us more vulnerable to incoming ultraviolet radiation, even the most severe recorded events have eroded less than 10% of the Earth's ozone and all have been recoverable. The impacts of energetic particles on the atmosphere of planets around UCDs are likely much worse. The outgoing particle radiation from a magnetically active UCD could be significantly higher than that of Sun-like stars, while the habitable zones around UCDs are also much closer, subjecting them to even higher levels of radiation.

Fortunately for us, the Sun does not exhibit the level of heightened magnetic activity thought to be responsible for radio emission in ultracool dwarfs. This also means that SPEs cannot be used to evaluate the effects of rapidly recurring or even quasi-quiescent strong energetic particle events on UCDs. In this case, simulations can provide insight into the effects of typical M dwarf emission on planetary atmospheres.

To get an idea of the impacts that reconnection events from UCDs can have on surrounding planets, I look to simulations that model the response of exoplanet atmospheres to stellar flares. In particular, Tilley et al. (2017) and Segura et al. (2010) ran simulations that explored the effects of repeated M dwarf flares on the ozone column depths in planetary atmospheres. All planets were envisioned to be Earth-like, including their atmospheric composition, and were all orbiting in the

habitable zone of an M dwarf. Both works consider two cases: one includes only the effects of electromagnetic radiation, and the other includes the combined effects of EM radiation and energetic protons. The results of these studies show that the electromagnetic radiation-only flares have a limited effect, while the addition of energetic protons causes more lasting and often irreversible damage. Tilley et al. (2017) found that an Earth-like planet exposed to UV flares without accompanying energetic protons had a fraction of a percent loss in ozone for the highest energy flaring events, whereas a single electromagnetic plus proton radiation event (of 5.9×10^8 pfu) can deplete the ozone abundance by up to 94% two years after the event, with a recovery time of 50 years. Even recurring flares with only EM radiation have limited effects on an Earth-like atmosphere, with 1-year interval flares showing no significant change in the ozone column over a 1000-year duration. More frequent flares with a 1 day separation can reduce the ozone column by a few percent, where it reaches a new equilibrium. Even in the most extreme electromagnetic-radiation-only scenarios, where very strong flares are recurring on an hourly basis continued over the course of the age of the universe (4×10^{17} s), the ozone column loss is less than that of a single high-energy flare that includes energetic protons. Conversely, the lowest energy electromagnetic plus proton flares, with 3×10^5 pfu, that recur over two-hour intervals will deplete the atmospheric ozone by $\geq 99\%$ in just over 1 year.

Energetic protons are released through magnetic stellar events such as magnetic reconnection during flares or in coronal mass ejections, and can be traced by millimetre emission. If gyrosynchrotron radiation from UCDs is indeed produced by sustained, small reconnection events as suggested by Williams et al. (2015), then corresponding energetic protons are also released into the circumstellar environment. While we cannot measure the energetic proton flux from a reconnection event directly, it can be inferred from the strength and spectral index of detected gyrosynchrotron radiation. Non-detections can further place upper limits on the particle flux. The resulting proton flux incident on surrounding planets can then be compared to the “catastrophic” values determined by simulations, as well as proton flux values from damaging Solar storms, to put the severity of the proton flux in context.

With this in mind, in this Chapter I investigate the potential proton flux incident

on hypothetical planets in orbit around the detected UCDs presented in Chapter 3, and place upper limits on the particle flux incident on the TRAPPIST-1 planets. These values are necessarily very speculative, as there are many outstanding unknowns regarding the magnetic activity of UCDs.

5.3 Estimating the Particle Flux

I use two strategies to estimate the UCD proton flux incident on surrounding planets, based on a range of assumptions about the nature of UCD reconnection events. First, I use known SEP flux values arriving at Earth and scale these to the size of UCD reconnection events and the inner and outer limits of their habitable zones, following Equation 5.5. This gives the proton flux incident on planets in orbit around UCDs if the quasi-quietescent energetic proton flux from radio loud UCD is similar to the Solar flare environment. The second method involves using the correlation between millimetre emission in Solar flares and subsequent proton flux measured at Earth to estimate the proton flux resulting from UCD millimetre emission.

5.3.1 Scaling the Proton Flux

The distance dependence of the energetic proton flux is not straightforward, even in the case of the Sun where in-situ observations are plentiful. Solar System spacecraft demonstrate that the proton flux can have a non-trivial radial profile that is dependent on the specific event and the orbital location of the detector. For example, Lario et al. (2013) find that at distances greater than 1 au the maximum proton flux scales as $d^{-3.3}$ and as d^{-3} at distances less than 1 au for the observed event. In prior observations, Lario et al. (2006) found an energy dependence on the proton scaling, with >4 MeV protons having a distance dependence of $d^{-2.7}$ and >51 MeV protons following $d^{-1.9}$. Theoretical work by Verkhoglyadova et al. (2012) suggests a weaker radial dependence, consistent with d^{-2} for MeV protons or even d^{-1} for protons with $E > 50$ MeV, while He et al. (2017) suggest $d^{-1.7}$ as a lower limit for the radial dependence. In this work, I adopt a characteristic d^{-2} distance dependence, but note that this scaling can vary.

It is also important to note that the outgoing protons follow helio-longitudinal

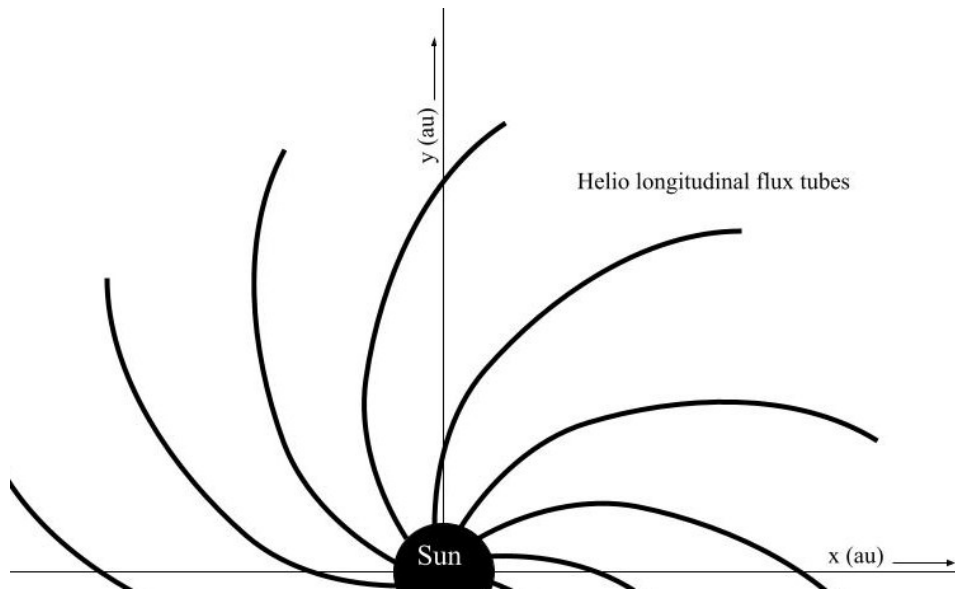


Figure 5.3: Schematic of the propagation of helio longitudinal flux tubes from the Sun, where outgoing particles extend along interplanetary magnetic field lines.

flux tubes along magnetic field lines (Figure 5.3), and can be influenced by other space weather such as coronal mass ejections. The dominant factor in the fluence, or time-integrated flux, of Solar energetic protons depends more on the helio-longitudinal distance between the Sun and spacecraft, rather than the heliocentric separation. The intensity of the proton flux arriving at Earth can be best estimated following the observed helio longitudinal path of outgoing energetic particles. The estimates in the following subsections are the proton fluxes a planet would receive if its orbit coincides with a flux tube. Given the quasi-quietescent nature of the radio emission, I expect the planet to sweep through multiple flux tubes throughout its orbit.

5.3.2 Proton Flux from Solar Particle Events

Solar storms are considered strong by the NOAA (*National Oceanic and Atmospheric Association*) storm radiation scale when the incident protons on Earth

Table 5.3: Estimates of proton fluxes received at UCD-orbiting planets if quasi-quiet UCD emission is equivalent to energetic protons released during Solar particle events.

UCD	Orbital Distance		
NLTT 33370	a_{in} (au)	a_{avg} (au)	a_{out} (au)
F_{p^+} (pfu)	4×10^6	3×10^6	1×10^6
LSR J1835	a_{in} (au)	a_{avg} (au)	a_{out} (au)
F_{p^+} (pfu)	7×10^6	4×10^6	2×10^6
LP 349	a_{in} (au)	a_{avg} (au)	a_{out} (au)
F_{p^+} (pfu)	2×10^7	7×10^6	4×10^6

reach values of 10^3 pfu (where $1 \text{ pfu} = 1 \text{ particle cm}^{-2} \text{ s}^{-1} \text{ sr}^{-1}$), and extend to $\geq 10^5$ pfu for the strongest storms. The September 1859 Solar Flare known as the Carrington event resulted in the strongest geomagnetic storm in recorded history. Since the Carrington event occurred prior to the development of Solar proton detectors, the resulting proton flux is unknown, but Miroshnichenko and Nymmik (2014) estimate an upper limit of 10^6 pfu for 10 MeV and greater protons.

In the following calculations I use the incident energetic protons emitted during SPEs measured at Earth to estimate the energetic protons received by a planet orbiting a UCD during a comparable event. This involves scaling the Solar proton flux values to the orbital distances of planets in the habitable zones calculated in Equation 5.5. I use the low values from the NOAA Solar storm radiation scale (10^3 pfu) in these calculations.

For a Solar particle flux arriving at Earth $F_{p^+}^\odot$, the outgoing energetic particles at the surface of the Sun at distance $d_\odot = 1 \text{ au}$ is,

$$L_{p^+}^\odot = F_{p^+}^\odot (4\pi d_\odot^2). \quad (5.8)$$

The magnetically active regions of UCDs are thought to cover a significant fraction of the surface, up to the full stellar disc for a magnetic field strength of $\sim 1 \text{ kG}$ and an assumed UCD radius of R_j following the limits set in Chapter 3. In the below calculations I treat the size of the emitting region as the full stellar disc, or πR_j^2 . Since magnetically active regions on the Sun have an average total size of 1% of the Solar disc (Canfield, 2000; Kallunki and Uunila, 2017), the emitting region of

the Sun ($0.01 \pi R_{\odot}^2$) is approximately the same size as a UCD. Therefore I do not use any scaling between the size of the Solar active region and the size of a UCD emitting region. The energetic proton luminosity in units of $\text{p}^+ \text{s}^{-1} \text{sr}^{-1}$ during a reconnection event at the UCD surface, L_{\odot}^{\star} is then,

$$L_{p^+}^{\star} = L_{p^+}^{\odot} = F_{p^+}^{\odot} (4\pi d_{\odot}^2). \quad (5.9)$$

The final step is to scale this value to the habitable zone distances,

$$F_{p^+}^{\star} = \frac{L_{p^+}^{\star}}{4\pi d_{\star}^2} = F_{p^+}^{\odot} \left(\frac{d_{\odot}}{d_{\star}} \right)^2. \quad (5.10)$$

Using the habitable zone calculations in Section 5.1, I use Equation 5.10 to estimate the proton flux that would be incident on planets in orbit around UCDs. This method assumes that quasi-quietescent reconnection events on UCDs release energetic protons similarly to Solar flares.

These energetic particle flux values exceed those measured at Earth, due to the close orbital distances of UCDs. The values found via this method are in excess of even the high end of the NOAA Solar storm scale, and the same order of magnitude as the proton flux theorised for the Carrington event. While this method does imply high proton flux values, the calculations were based on specific events. According to the M dwarf flare simulations of Tilley et al. (2017) and Segura et al. (2010), an Earth-like atmosphere would not be able to recover from this level of proton flux.

5.3.3 Proton Flux from Solar Radio Bursts

The method used in the previous subsection relies on scaling the Solar proton flux values only to estimate the proton flux incident on surrounding planets. This method does not take into account the detected emission from UCDs, which is likely the result of magnetic reconnection events. The measured millimetre emission of UCDs can be used instead to estimate the proton flux by applying to the UCDs the median ratio between Solar millimetre emission during flares and subsequent proton fluxes at Earth. Unlike the previous method, this does not involve assuming anything about the size of the UCD emitting region.

Millimetre emission from the Sun has been proposed as a predictor for ener-

Table 5.4: The 5, 9 and 15 GHz emission measured by the Radio Solar Telescope Network along with the maximum energetic (> 10 MeV) particle flux measured by the GOES satellite from the SPEs that accompanied all 6 of the observed flares. [1] Joshi et al. (2013) [2] Belov et al. (2015) [3] Neal et al. (2013) [4] Paassilta et al. (2017).

Date	$F_{5 \text{ GHz}}$ (Jy)	$F_{9 \text{ GHz}}$ (Jy)	$F_{15 \text{ GHz}}$ (Jy)	F_{p^+} (pfu)
23 Jan 2012	1.2×10^7	1×10^7	7×10^6	3000 ^[1]
27 Jan 2012	7×10^7	7×10^7	4×10^7	800 ^[2]
7 Mar 2012	4×10^6	6×10^6	9×10^6	6000 ^[2]
13 Mar 2012	3×10^7	4×10^7	2×10^7	470 ^[3]
12 Jul 2012	9×10^6	1×10^8	9×10^6	96 ^[4]
28 Sep 2012	6×10^8	4×10^8	4×10^8	60 ^[4]

getic protons (Klein et al., 2018). Solar radio bursts are characterised by intense millimetre emission associated with Solar flares, many of which are followed by a heightened flux of energetic protons measured at Earth. Zucca et al. (2017) observed 6 SEP events throughout 2012, and found that the combination of 5, 9, and 15 GHz observations of Solar flares, covering the full Solar disc, were just as accurate at predicting Solar particle events as the previous method that relied on the time derivative of soft X-ray emission, and included no false alarms.

In this method, I use the maximum millimetre flux values during the 6 observed Solar flares and the subsequent proton flux during the subsequent SPEs measured at Earth to find an average ratio between the radio luminosity and outgoing proton luminosity. The radio observations in this study were taken by the Radio Solar Telescope Network (RSTN), a group of four observatories that gather whole-Sun radio flux densities across a few radio frequencies. The RSTN data are publicly available through the National Geophysical Data Centre, which I rely on for the Solar radio burst measurements. The maximum radio flux values during each Solar flare, as determined from the RSTN observations, are shown in Table 5.4 with the peak proton fluxes measured from the subsequent SPEs on those dates as well.

A 2018 study on well-observed Solar flares that occurred in early September 2017 similarly found that GHz radio bursts were followed by increased >10 MeV proton fluxes received at Earth. Chertok (2018) found that a 4 Sept 2017 flare had a peak 3 GHz flux of 2×10^7 Jy and an energetic proton flux of 100 pfu, and a 10 Sept

Table 5.5: Radio luminosities, proton luminosities, and ratios of the two for all Solar flares in this section. The radio luminosities of the events detailed in Table 5.4 were found by averaging all maximum flux values for each event. Note that the units of L_R and L_{p^+} are not the same, so the ratio in the last column is not unitless.

Date	L_R (erg s ⁻¹ Hz ⁻¹)	L_{p^+} (p ⁺ s ⁻¹ sr ⁻¹)	L_R / L_{p^+} (p ⁺ ⁻¹ erg Hz ⁻¹ sr)
23 Jan 2012	3×10^{11}	9×10^{30}	3×10^{-20}
27 Jan 2012	2×10^{12}	2×10^{30}	1×10^{-18}
7 Mar 2012	2×10^{11}	2×10^{31}	1×10^{-20}
13 Mar 2012	8×10^{11}	1×10^{30}	8×10^{-19}
12 Jul 2012	1×10^{12}	3×10^{29}	3×10^{-18}
28 Sep 2012	1×10^{13}	2×10^{29}	5×10^{-17}
4 Sep 2017	6×10^{11}	3×10^{29}	2×10^{-18}
10 Sep 2017	6×10^{12}	3×10^{30}	2×10^{-18}
28 Aug 1966	8×10^{11}	4×10^{28}	2×10^{-17}
30 Aug 1966	1×10^{11}	3×10^{29}	3×10^{-19}

2017 flare had at 15 GHz flux of 2×10^8 Jy followed by an energetic proton flux of 1000 pfu. Observations during the 1966 Proton Flare Project (Švestka and Simon, 1969) found a 28 August 1966 Solar flare reached a peak 10.7 GHz flux of 3×10^7 Jy and outgoing proton flux of roughly 15 pfu, while a 30 Aug 1966 flare reached a peak 91 GHz flux of 5×10^6 Jy and a received particle flux of approximately 100 pfu.

To determine the ratio of radio luminosity to resulting proton luminosity, I scale the measured radio and proton flux values measured at Earth following $L = 4\pi d^2 F$. The resulting radio luminosities (L_R) in units of ergs and proton luminosities (L_{p^+}) in units of p⁺ s⁻¹ sr⁻¹ for each event are listed in Table 5.5, where the radio luminosities from the Table 5.4 events were found by averaging the 5, 9, and 15 GHz fluxes. There is a large spread in L_R / L_{p^+} values spanning three orders of magnitude. While there is no straightforward numerical correlation between the radio and proton luminosities, it is clear that the increased radio luminosity during flares corresponds to an increase in proton luminosity as well. I adopt the median value of $L_R / L_{p^+} \approx 10^{-18} \text{ p}^{+1} \text{ erg Hz}^{-1} \text{ sr}$ from all Solar events in Table 5.5 in my estimates.

Table 5.6: Proton fluxes received at the inner and outer edges of the habitable zone for the detected UCDs and at TRAPPIST-1e and g following Equation 5.11. The distances and fluxes of each UCD are rounded to the nearest integer for these calculations. These estimates include values for both the quiescent and flaring flux of NLTT 33370 and the VLA and ALMA limits on TRAPPIST-1, as well as values found by assuming TRAPPIST-1 has radio flux consistent with the GBR.

UCD	Dist (pc)	Freq (ν)	F (μ Jy)	$F_{p^+}^{\text{in}}$ (pfu)	$F_{p^+}^{\text{out}}$ (pfu)
NLTT 33370 (quiesc)	97.5	16	600	3×10^8	8×10^7
NLTT 33370 (flare)	97.5	16	4880	2×10^9	7×10^8
LP 349-25	10	97.5	70	4×10^9	1×10^7
LSR J1835	6	97.5	114	1×10^7	4×10^6
TRAPPIST-1 (VLA)	44	12	<16	$<1 \times 10^6$	$<5 \times 10^5$
TRAPPIST-1 (ALMA)	97.5	12	<11	$<9 \times 10^5$	$<3 \times 10^5$
TRAPPIST-1 (GBR)	8	12	0.06	4000	2000

I apply this ratio to the radio emission of the detected UCDs, as well as on the upper limits for TRAPPIST-1. The radio luminosities in units of $\text{erg s}^{-1} \text{Hz}^{-1}$ are found by multiplying the measured flux values by $4\pi d^2$, where d is the distance to the UCD. Dividing by the ratio of $\sim 10^{-18} \text{p}^+ \text{erg Hz}^{-1} \text{sr}$ determined for Solar events gives a proton luminosity at the surface of the UCD in units of $\text{p}^+ \text{s}^{-1} \text{sr}^{-1}$. Energetic proton fluxes arriving at habitable zone distances can then be found by dividing the proton luminosity by $4\pi a^2$, where a is the orbital distance of the habitable zone. Thus,

$$F_{p^+} = 4\pi d^2 F_R \frac{10^{18} \text{p}^+ \text{erg}^{-1} \text{Hz sr}^{-1}}{4\pi a^2} = 10^{18} F_R \left(\frac{d}{a} \right)^2 \text{p}^+ \text{erg}^{-1} \text{Hz sr}^{-1}. \quad (5.11)$$

Taking the measured flux densities of the detected UCDs presented in Chapter 3 and the upper limits set on the TRAPPIST-1 observations, I estimate the incident protons on the inner and outer edges of the habitable zone for the detected UCDs, and on the closest and most distant habitable zone planets in the TRAPPIST-1 system. All values are shown in Table 5.6, and span a range that encompasses the values estimated in Subsection 5.3.2. Most proton flux approximations in this

section exceed the upper values during Solar storms (10^5 pfu), and most exceed the estimated proton flux for the Carrington event (10^6 pfu). The TRAPPIST-1 estimates include both the 44 GHz VLA and 97.5 GHz ALMA observations as well as the peak radio flux if the star does emit in agreement with the GBR. These values are noticeably lower than those found for the radio loud UCDs, but still higher than quiescent values measured on Earth of roughly 1 pfu.

5.4 Implications for Planets in Radio Loud UCD Systems

The lower ranges of both methods of estimating the proton flux incident on the habitable zones around UCDs return estimates consistent with the NOAA Solar storm range of 10^3 to 10^5 pfu, and the highest estimates exceed the theorised proton flux from the Carrington Event. The high values are comparable to what Tilley et al. (2017) determined to be catastrophic for an Earth-like atmosphere from a single flare (see Figure 5.2). The proton flux estimates in Subsection 5.3.2 assumes that planets align with the flux tube of energetic protons. Since the radio emission is quasi-quiescent and could be representative of continuous surface reconnection activity, a UCD-orbiting planet would sweep through multiple flux tubes throughout its orbit. The impacts of quiescent reconnection events releasing a constant flow of energetic proton fluxes at Solar storm values are yet to be explored, and many assumptions are necessary for the estimates. However, if the high proton flux estimates are representative of UCD particle events, it is difficult to see how planets in close orbit around active UCDs could retain Earth-like atmospheres in this paradigm.

The proton flux estimates on the TRAPPIST-1 planets present a more optimistic picture for radio quiet UCDs. If TRAPPIST-1 does have radio emission in line with the GBR, then the incident protons estimates in Subsection 5.3.3 are consistent with the lowest values on the NOAA Solar storm range. The lowest estimates predicted by both methods are higher than the quiescent particle flux values arriving at Earth (Gopalswamy et al., 2020).

My estimates of the upper limit on the quiescent energetic proton flux incident on TRAPPIST-1e indicate that the TRAPPIST-1 planets may not be overtly threatened by catastrophic magnetic processes. This does not, however, guarantee that the TRAPPIST-1 planets are safe from such processes altogether. While the upper

proton flux limit is well below the catastrophic value used by Tilley et al. (2017) and Segura et al. (2010), it is still within the range considered “strong” for Solar radiation storms on Earth. Smaller scale gyrosynchrotron events such as those seen on the Sun are still possible in the TRAPPIST-1 system. Bursting rather than quiescent radio emission may also be possible, but not present during the relatively short on-source timescales of previous observations. The flare rate of TRAPPIST-1 is 0.38 day^{-1} (Vida et al., 2017), meaning that each of our observations only monitored $\sim 10\%$ of the characteristic timescale of active regions (Morris et al., 2018). Assuming the flares follow a Poisson distribution, then the probability of not detecting a flare in both the ALMA and 33 GHz VLA observations is $\sim 80\%$. However, my 50-hour monitoring campaign of TRAPPIST-1 failed to capture any variability at 3 GHz, at least suggesting that the star may be radio quiet even during flares.

It is important to recognize that many assumptions went into these calculations in the absence of more detailed observations of UCDs. The conclusions drawn from the proton flux estimates should not be seen as absolutes, but can be used to prioritise exoplanet targets for future biosignature searches and inform exoplanet atmosphere models, discussed further in Chapter 5.

5.5 Summary

In this chapter I have used the results of my UCD survey to estimate the energetic particle flux incident on the surrounding planets, or in the case of TRAPPIST-1, place upper limits on the energetic flux value. Under some reasonable assumptions about the behaviour of UCD reconnection events, my results indicate that radio bright UCDs could inundate their planets with particle fluxes that would be catastrophic for Earth-like atmospheres. The upper limits I placed for incoming particle flux incident on the closest TRAPPIST-1 planet in the habitable zone indicate that the planets are not exposed to similarly high levels, whereas if TRAPPIST-1 emits consistently with GBR, the TRAPPIST-1 planets are exposed to similar quiescent proton flux levels as the Earth during heightened periods of Solar activity.

Chapter 6

Summary and Future Work

Despite the ubiquity of low-mass stars and substellar objects in the Solar Neighbourhood, many questions remain about their magnetic field configuration, dynamo mechanism, radio frequency behaviour, and the space weather environment they create for orbiting planets. Previous radio studies of UCDs have been predominately focused on the radio frequency range where UCD emission is brightest, 1-10 GHz for typical magnetic field strengths. These studies have revealed that roughly 10% of UCDs are indeed radio bright, defying expectations based on the absence of a tachocline in fully convective objects and empirical trends observed in magnetically active F through M stars. However, prior to this work only one UCD had been detected at millimetre wavelengths where gyrosynchrotron radiation dominates, and little attention has been given to the consequences of UCD magnetic activity on surrounding planets.

In this thesis I have presented the second through fourth detections of UCDs at millimetre wavelengths, placed upper limits on the radio emission of the infamous planet-hosting UCD TRAPPIST-1, and explored new methods for investigating the impact of UCD magnetic activity on surrounding planets. My results indicate that gyrosynchrotron emission detectable at millimetre wavelengths may be ubiquitous in UCDs that are radio bright at 1 – 10 GHz, and show the need for further high radio frequency observations of UCDs to build larger sample sizes. I have determined that, given a few reasonable assumptions about the underlying magnetic activity, radio loud UCDs with a gyrosynchrotron component could be inundating their

planets with high levels of particle flux that would be damaging for Earth-like atmospheres and surface life according to the Tilley et al. (2017) and Segura et al. (2010) models. My investigation into the UCD TRAPPIST-1, conversely, found sustained radio silence, indicating that the TRAPPIST-1 planets may not be subject to the same high levels of particle flux.

6.1 Summary

This work combines elements of both stellar astrophysics and planetary astronomy to build a more complete picture of ultracool dwarfs and the planets around them. This involved measuring the radio emission of UCDs to **(a)** determine the emission mechanism, **(b)** characterize magnetic properties of the dwarf, and **(c)** infer details about the space weather environment incident on planets in orbit around radio emitting UCDs. Prior to the development of telescopes such as the VLA and ALMA that achieved high radio sensitivity, measurable radio emission from UCDs was unexpected, given both their fully convective interiors - which were thought to inhibit the necessary level of magnetic activity to produce detectable radio emission - as well as observational trends seen in the X-ray and radio luminosities of more massive stars. However, since the initial discovery of radio emission from a brown dwarf, VLA and Arecibo surveys have found that just over 10% of them are radio loud, with emission up to four orders of magnitude brighter than values predicted following the GBR. Although a handful of both incoherent and coherent processes are capable of producing emission in the relevant frequency range, two primary emission mechanisms are thought to be responsible for this unexpected activity: ECMI and gyrosynchrotron radiation. Both mechanisms produce emission peaking near the cyclotron frequency, but ECMI emission becomes unphysical at higher frequencies where gyrosynchrotron radiation is expected to dominate. Observations at these higher radio frequencies, 30 – 100 GHz for typical UCD magnetic field strengths, are uniquely useful for determining the presence and strength of gyrosynchrotron radiation only.

In Chapter 3, I presented ALMA and VLA observations of five UCDs with a range of properties and radio behavior. Of these targets, three were found to be active at 97.5 GHz, whereas two were not detected at 33 GHz (LP 423-31) or

97.5 GHz (LP 415-20). Thus far, all UCDs that have been reliably detected near 8 GHz and within 30 – 100 GHz exhibit emission in both of these frequency ranges. The observations presented here give spectral indices ranging from $\alpha = -0.76$ to $\alpha = -0.29$, most consistent with gyrosynchrotron emission in the optically thin regime. The data for all detected UCDs were split into smaller time bins, with the peak flux and RMS taken from each chunk using the *CASA* task *uvmodelfit*. Each peak flux was then used to generate a time series of the stellar brightness. Two of the detections (LP 349-25 and LSR J1835) show little time variation throughout the observations (2 hr and 1 hr on source, respectively), while NLTT 33370 shows minor temporal variability and a strong flare that exceeded the average quiescent flux by a factor of 20. These results provide evidence that gyrosynchrotron radiation may be common in radio emitting UCDs, and speak to the need for additional high radio frequency observations of a larger sample.

In Chapter 4, I presented 97.5 GHz ALMA and 44 GHz VLA observations of the TRAPPIST-1 system. I find non-detections at both frequencies, and place 3σ upper level flux limits of 10.6 μJy and 16.2 μJy at 97.5 GHz and 44 GHz, respectively. Analysis of the individual scans showed no signs of variability with median 3σ upper limits of 110 μJy and 190 μJy per scan for ALMA and the VLA, respectively. Only 10% of ultracool dwarfs emit in excess of the Güdel-Benz relation, with a loose correlation with rotation rate and anti-correlation X-ray luminosity. UCDs with slow rotation rates and high X-ray emission tend to be dim or undetected at radio frequencies, whereas UCDs with high rotation rates and low X-ray emission are more likely to have detectable radio emission. With a slow rotation rate of 3.295 ± 0.003 days and high X-ray luminosity of $(3.8 - 7.9) \times 10^{26} \text{ erg s}^{-1}$, TRAPPIST-1 conforms to this trend. I also presented preliminary results from my monitoring campaign of TRAPPIST-1, which included 39 hours of on-source observations to search for transient bright radio activity near the cyclotron frequency. While my results show a non-detection, additional processing is required before publication and described in Section 6.2.1.

In Chapter 5, I used the results of my observations to estimate the energetic particle flux incident on planets in orbit around UCDs. I find that, giving a reasonable set of assumptions about the origin and strength of UCD reconnection events, the particle flux incident on planets in the habitable zone of radio loud

UCDs matches and exceeds values of Solar storms and the monumental Carrington event. This indicates that, if UCD reconnection events are similar to those on the Sun, then Earth-like planets in orbit around radio loud UCDs are likely subject to damaging levels of energetic particle radiation. Conversely, the non-detections of TRAPPIST-1 suggest that the planets may not be exposed to similar levels of radiation.

6.2 Future Work

In future work, I will expand on my Ph.D. research, surveying a larger sample of UCDs at high and low radio frequencies and across the electromagnetic spectrum to build a more complete understanding of their radio emission and magnetic structure, and further investigate the consequences for planetary atmospheres. I aim to answer the questions - **what is the dominant emission mechanism of radio emitting UCDs, what correlations exist in emission across the electromagnetic spectrum, and what does this mean for life on the planets around them?** This will involve:

- **Completing the self-calibration process for my monitoring campaign of TRAPPIST-1, and publishing the results**

My preliminary results show a non-detection, but self-calibration on the data is necessary to remove artefacts introduced by a bright quasar present in the side lobes and lower the RMS.

- **Expanding the sample of UCDs known to be active at 1-10 GHz through radio surveys**

With my upcoming VLA observations, future radio surveys, and existing unpublished radio observations, I will expand the number of UCDs that have been observed in the 1 – 10 GHz frequency range, refining the detection rate and identifying candidates for follow-up observations at higher radio frequencies and across the electromagnetic spectrum. These candidates will be selected from existing optical, infrared, and X-ray surveys, including K2, Chandra, XMM-Newton, Spitzer, and TESS.

- **Conducting follow-up high radio frequency observations of UCDs known**

to emit at low radio frequencies to constrain the spectral index of gyrosynchrotron radiation

Observations, such as my upcoming VLA survey at 33 GHz, can break the degeneracy between ECMI and gyrosynchrotron radiation and better characterize the latter.

- **Investigating the Impact of UCD Activity on Surrounding Planets**

The strength and spectral index of optically thin gyrosynchrotron radiation can be used to approximate the space weather environment around the UCD, as I did in my Ph.D. work. In the future, I would like to do a more detailed analysis of additional targets, and work with exoplanet astronomers to inform models of UCD particle flux on surrounding planets.

- **Conducting Multi-Wavelength Observations of UCDs**

Observations across the electromagnetic spectrum are crucial to characterize UCD activity. I will cross-match all radio observed UCDs with existing light curves from K2, Spitzer, and TESS to measure their rotation periods and their flare rates and energies, to search for correlations with radio activity. I will also pursue simultaneous multi-wavelength follow-up of known radio-active UCDs using UV and X-ray observations with Swift, Hubble, Chandra, and XMM-Newton to further investigate correlations in activity from radio to X-ray wavelengths, and place further constraints on UCD activity and the potential impact on exoplanet atmospheres.

6.2.1 TRAPPIST-1 Monitoring Campaign

My 50-hour observations of TRAPPIST-1 show a preliminary null detection with 3σ upper flux density limit of $510 \mu\text{Jy}$. The sensitivity of these observations was significantly impacted by the presence of a bright radio quasar that was not removed in CASA pipeline calibration.

I will continue to perform self-calibration on the observations to remove the noise-like artefacts caused by the quasar. This involves a largely guess-and-check method of creating a model of the observations and calibrating the corrupted data against that model.

6.2.2 Upcoming VLA Surveys

I have two ongoing Semester 2020A VLA proposals to observe (i) a sample of 5 UCDs at 33 GHz that are known to emit at 8 GHz and (ii) a sample of 21 UCDs at 2 GHz with known $v \sin i$. The 33 GHz survey has the goal of measuring the high radio frequency emission from targets known to be active at lower frequencies, and from this constraining spectral indices of those active in both frequency ranges and the size of the radio emitting region and impacts on planetary atmospheres. The 2 GHz survey will investigate the still-tenuous relationship between rotation rate and radio brightness.

In the models proposed by McLean et al. (2012) and Williams et al. (2014), the presence of radio emission is due to the magnetic field topology rather than the strength. Slowly rotating UCDs ($v \sin i \leq 10 \text{ km s}^{-1}$) tend towards axisymmetric dynamos and strong magnetic fields (Stelzer et al., 2012), whereas rapidly rotating UCDs ($v \sin i \geq 20 \text{ km s}^{-1}$) can have either an axisymmetric or non-axisymmetric dynamo and any strength field. Each dynamo creates a distinct field topology, which determines the radio behavior of the star. In other models (Pineda, 2017; Hallinan et al., 2007), global aurorae are responsible for UCD radio emission. This requires strong magnetic fields as well as rapid rotation; indicating that all UCDs with detectable radio emission will also be rapidly rotating.

In order to test these models and gain insight into the magnetic behavior of UCDs, it is important to have accurate statistics on the correlation between rotation rate and both likelihood and strength of radio emission. My target list in this survey includes both rapidly and slower rotating UCDs. All of these targets have known rotation period, thus removing the $v \sin i$ ambiguity.

My other VLA survey includes 33 GHz observations of UCDs known to be radio bright in the 1 – 10 GHz frequency range. These observations will provide tight constraints on the spectral index, and determine the radio emission mechanism, as was done in Chapter 3 of this work.

6.2.3 Archival Data

At least 10 UCDs have unpublished archival VLA and ALMA observations at high frequencies between 20 – 100 GHz. I will download and reduce these observations

as part of my ongoing work to survey UCDs at millimetre wavelengths where gyrosynchrotron radiation dominates. The VLA Sky Survey and Stripe Survey have wide-field observations at 2 and 1.4 GHz, respectively. Between K2, Spitzer, GAIA, and TESS, there are on the order of hundreds of UCDs that fall within the large field of view encompassed by these surveys. I will look for the brightest UCDs in these surveys, expanding the number (currently ~ 200) of those observed at low radio frequencies to ≥ 300 . Upper flux density estimates can be made for all non-detections, fully utilizing the results of the VLA surveys. Between archival data and my upcoming VLA surveys, I expect to expand the number of UCDs observed at low radio frequencies between 1 – 10 GHz from 200 to ≥ 300 , at least a 50% increase. This work will also expand the number of UCDs observed at medium-to-high radio frequencies 20 – 100 GHz from 7 to 22, a $>200\%$ increase.

6.2.4 Investigating the impact on planetary habitability

This work exists at the intersection between stellar physics and planetary astronomy. The observations and analysis themselves are concerned with the magnetic activity of low-mass stars and brown dwarfs, while the implications extend to planetary atmospheres. As seen in Chapter 5, the presence of gyrosynchrotron radiation traceable by radio observations could be catastrophic for life on planets in orbit around UCDs. I will further explore the effects of gyrosynchrotron radiation of UCDs on the terrestrial planets in close orbit. In future work, I would like these result to inform simulations on the impacts UCD activity has on the stability surrounding planets. This would involve collaboration with exoplanet atmosphere scientists who can use my quiescent flux values and habitable zone distances to run simulations of their impacts on the ozone content of Earth-like atmospheres.

6.2.5 Correlating Observations Across Wavelengths

Radio observations alone are insufficient to fully characterize UCDs - observations at multiple frequencies are necessary both to identify promising targets for radio observation and investigate correlations between emission across the electromagnetic spectrum. The TESS, Spitzer, and K2 missions can measure flares, which are a signature of reconnection driving radio emission, as well as determine stellar

rotation rates by tracking the motion of starspots. Knowing the true rotation rate is crucial to determine whether the observed correlation between radio brightness and $v \sin i$ is dependent on the stellar inclination. An inclination or $v \sin i$ dependence would be expected of ECMI that is strongly dependent on beaming, whereas a correlation with rotation rate is more consistent with gyrosynchrotron models where rapid rotation correlates to more reconnection events. As part of my future work, I will examine the archival K2, TESS, and Spitzer light curves of known radio bright UCDs to investigate these correlations, as well as identify photometrically variable UCDs for follow-up multi-wavelength observations.

Finally, I will propose simultaneous multi-wavelength observations using Swift, Hubble, TESS, NICER, Chandra, and the VLA. These observations of UCDs known to exhibit variability and flaring will investigate the underlying physical processes. In a magnetic reconnection event, electrons spiraling along magnetic field lines produce non-thermal gyrosynchrotron emission at radio wavelengths and X-ray emission. This then heats the chromospheric gas, releasing visible and UV emission observable with HST, TESS, and Swift. If no correlation is observed between emission at these wavelengths, that would suggest a disconnect in physical processes. The VLA has the sensitivity necessary to capture radio emission from these very dim objects, while Swift has the advantage of both X-ray and UV telescopes, with a flexible Target of Opportunity program that has a high acceptance rate, making simultaneous observation straightforward. In the event that I have radio observations scheduled and the target is being observed by TESS in the extended mission, requesting a Target of Opportunity on Swift would give me radio, optical, UV, and X-ray data.

Multiwavelength M Dwarf Flares

While Solar flares provide us with a template of the stellar flaring process because they are relatively straightforward to study, M dwarfs differ significantly from G stars in terms of density, temperature, and levels of magnetic activity. Existing observations of M dwarf flares show that their behaviour does depart significantly from that of Solar flares, including more coronal emission than what is observed from any other spectral type (Osten et al., 2004). Multi-wavelength observations

of Solar flares reveal that emission follows something called the Neupert effect, an observational description showing that hard X-ray, optical, and UV emission is released first, followed by soft X-ray and extreme UV emission (Dennis and Schwartz, 1989; Neupert, 1968). The generally accepted explanation of this is that reconnection events begin with non-thermal emission prompted by electrons accelerated along magnetic field lines, resulting in radio, optical, UV, and hard X-ray emission. The energy released into the Solar atmosphere by these processes temporarily heats the ambient chromospheric gas, releasing thermal emission at soft X-ray and extreme UV frequencies.

Solar flares usually originate in surface regions of high magnetic activity along magnetic inversion lines (or magnetic neutral lines), separating areas of opposing magnetic polarity. These areas are associated with filaments, lines of cooler plasma suspended in the Solar atmosphere. Observations of Solar flares and coronal mass ejections (CMEs) show an initial period of filament activation, where filaments extend upward over roughly 30 minute timescales prior to the flare or CME (Kopp and Pneuman, 1976). Unstable magnetic fields seem to trigger the onset of a flare. This is thought to happen under a number of different circumstances, such as an imbalance in the ambient pressure triggered by winds, or shifting of the magnetic field footpoints in the photosphere (e.g. Priest et al., 1994), which increases the stored magnetic energy.

This process begins when stressed magnetic field lines underneath the photosphere begin to rise, increasing the free energy stored in the corona (Priest and Forbes, 2002). By some triggering event, likely triggered by motion of the magnetic field footpoints, the magnetic field falls out of equilibrium and becomes unstable. This causes the field lines to break apart and extend outward into the heliosphere. It is in this stage that they release energy in the form of radiation, accelerated particles, and sometimes plasma in the event of a coronal mass ejection. The magnetic field lines then close in the reconnection phase, and the magnetic field settles into a lower energy, equilibrium state. In this final stage the coronal plasma is heated thermally. These events are thought to be magnetically driven because of the plasma β , where

the ratio of plasma pressure to magnetic pressure is given by,

$$\beta = \frac{nk_B T}{B^2/2\mu_0}. \quad (6.1)$$

In the case of the Sun, $\beta < 0.01$ (Cairns, 2005), indicating that the energy necessary for energetic flares and coronal mass ejections is almost certainly stored in the magnetic field.

Some observations of M dwarf flares suggest that their behaviour departs from what is typically seen in Solar flares. While there is some evidence that the Neupert effect does hold for multiple spectral types (Hawley et al., 1995), M dwarfs behave differently. Osten et al. (2004) found that while EV Lac showed strong correlated X-ray and radio flares, there was no clear correlation with soft X-ray emission.

While millimetre observations probe the optically thin gyrosynchrotron emission, UV/X-ray and optical observations can determine whether there is a (dis)connect between the processes of radio-emitting particle acceleration and plasma heating during the flare, resulting in delayed UV and X-ray emission. Including observations across multiple frequencies allows for a more complete characterisation of the stellar variability of UCDs, and as a consequence, the space weather environment of planets in orbit around radio emitting UCDs.

Bibliography

Adams, F. C., P. Bodenheimer, and G. Laughlin

2005. M dwarfs: planet formation and long term evolution. *Astronomische Nachrichten*, 326(10):913–919. → page 5

Alberti, T., V. Carbone, F. Lepreti, and A. Vecchio

2017. Comparative climates of the trappist-1 planetary system: Results from a simple climate-vegetation model. *The Astrophysical Journal*, 844(1):19. → page 75

Alekseev, I. Y. and O. V. Kozlova

2002. Starspots and active regions on the emission red dwarf star LQ Hydrae. *Astronomy and Astrophysics*, 396:203–211. → page 71

Alibert, Y. and W. Benz

2017. Formation and composition of planets around very low mass stars. *Astronomy and Astrophysics*, 598:L5. → page 5

Antonova, A., G. Hallinan, J. G. Doyle, S. Yu, A. Kuznetsov, Y. Metodieva, A. Golden, and K. L. Cruz

2013. Volume-limited radio survey of ultracool dwarfs. *Astronomy and Astrophysics*, 549:A131. → pages 1, 19, 58

Barnes, R.

2017. Tidal locking of habitable exoplanets. *Celestial Mechanics and Dynamical Astronomy*, 129(4):509–536. → pages 6, 91

Basri, G.

1998. The Lithium Test for Young Brown Dwarfs (invited review). In *Brown Dwarfs and Extrasolar Planets*, R. Rebolo, E. L. Martin, and M. R. Zapatero Osorio, eds., volume 134 of *Astronomical Society of the Pacific Conference Series*, P. 394. → page 8

- Basri, G.
2000. Observations of Brown Dwarfs. *Annual Review of Astron and Astrophys*, 38:485–519. → page 6
- Bastian, T. S., A. O. Benz, and D. E. Gary
1998. Radio Emission from Solar Flares. *Annual Review of Astron and Astrophys*, 36:131–188. → page 40
- Beccari, G. and G. Carraro
2015. *Introduction to the Theory of Stellar Evolution*, volume 413, P. 1. → page 2
- Belov, A., E. Eroshenko, O. Kryakunova, N. Nikolayevskiy, A. Malimbayev, I. Tsepakina, and V. Yanke
2015. Possible ground level enhancements at the beginning of the maximum of Solar Cycle 24. In *Journal of Physics Conference Series*, volume 632 of *Journal of Physics Conference Series*, P. 012063. → pages x, 102
- Bensby, T., S. Feltzing, and I. Lundström
2003. Elemental abundance trends in the Galactic thin and thick disks as traced by nearby F and G dwarf stars. *Astronomy and Astrophysics*, 410:527–551. → page 4
- Benz, A. O. and M. Güdel
1994. X-ray/microwave ratio of flares and coronae. *Astronomy and Astrophysics*, 285:621–630. → pages xii, xvii, 18, 82
- Berdyugina, S. V., D. M. Harrington, O. Kuzmychov, J. R. Kuhn, G. Hallinan, A. F. Kowalski, and S. L. Hawley
2017. First Detection of a Strong Magnetic Field on a Bursty Brown Dwarf: Puzzle Solved. *Astrophysical Journal*, 847(1):61. → pages ix, 58, 60
- Berger, E.
2002. Flaring up All Over-Radio Activity in Rapidly Rotating Late M and L Dwarfs. *Astrophysical Journal*, 572(1):503–513. → page 38
- Berger, E.
2006. Radio Observations of a Large Sample of Late M, L, and T Dwarfs: The Distribution of Magnetic Field Strengths. *Astrophysical Journal*, 648:629–636. → pages 1, 19, 58, 66, 67, 69, 73
- Berger, E., S. Ball, K. M. Becker, M. Clarke, D. A. Frail, T. A. Fukuda, I. M. Hoffman, R. Mellon, E. Momjian, N. W. Murphy, S. H. Teng, T. Woodruff,

- B. A. Zauderer, and R. T. Zavala
2001. Discovery of radio emission from the brown dwarf LP944-20. *Nature*, 410(6826):338–340. → pages 19, 58
- Berger, E., G. Basri, J. E. Gizis, M. S. Giampapa, R. E. Rutledge, J. Liebert, E. Martín, T. A. Fleming, C. M. Johns-Krull, N. Phan-Bao, and W. H. Sherry
2008a. Simultaneous Multiwavelength Observations of Magnetic Activity in Ultracool Dwarfs. II. Mixed Trends in VB 10 and LSR 1835+32 and the Possible Role of Rotation. *Astrophysical Journal*, 676(2):1307–1318. → pages xvii, 27, 81, 82, 83
- Berger, E., J. E. Gizis, M. S. Giampapa, R. E. Rutledge, J. Liebert, E. Martín, G. Basri, T. A. Fleming, C. M. Johns-Krull, N. Phan-Bao, and W. H. Sherry
2008b. Simultaneous Multiwavelength Observations of Magnetic Activity in Ultracool Dwarfs. I. The Complex Behavior of the M8.5 Dwarf TVLM 513-46546. *Astrophysical Journal*, 673:1080–1087. → page 30
- Blackman, E. G. and A. Hubbard
2014. Ribbons characterize magnetohydrodynamic magnetic fields better than lines: a lesson from dynamo theory. *Astrophysics and Space Science*, 442(2):1040–1048. → pages xii, 15
- Burbidge, G.
1957. The Crab Nebula-A Cosmic Synchrotron. *Leaflet of the Astronomical Society of the Pacific*, 7(332):257. → page 36
- Burgasser, A. J. and E. E. Mamajek
2017. On the Age of the TRAPPIST-1 System. *Astrophysical Journal*, 845:110. → page 75
- Burgasser, A. J. and M. E. Putman
2005. Quiescent Radio Emission from Southern Late-Type M Dwarfs and a Spectacular Radio Flare from the M8 Dwarf DENIS 1048-3956. *Astrophysical Journal*, 626:486–497. → page 30
- Cairns, R. A.
2005. Tokamaks 3rd Edition by John Wesson, Oxford University Press 2004, 749pp, Hardback 0 19 850922, £135. *Journal of Plasma Physics*, 71(3):377–377. → page 116
- Canfield, R.
2000. *Solar Active Regions*, P. 2023. → page 100

- Chabrier, G., I. Baraffe, F. Allard, and P. Hauschildt
2000. Evolutionary Models for Very Low-Mass Stars and Brown Dwarfs with Dusty Atmospheres. *Astrophysical Journal*, 542(1):464–472. → pages 6, 11
- Chabrier, G., I. Baraffe, J. Leconte, J. Gallardo, and T. Barman
2009. The mass-radius relationship from solar-type stars to terrestrial planets: a review. In *15th Cambridge Workshop on Cool Stars, Stellar Systems, and the Sun*, E. Stempels, ed., volume 1094 of *American Institute of Physics Conference Series*, Pp. 102–111. → page 8
- Chabrier, G. and M. Küker
2006. Large-scale α^2 -dynamo in low-mass stars and brown dwarfs. *Astronomy and Astrophysics*, 446(3):1027–1037. → pages 11, 17
- Chertok, I. M.
2018. Diagnostic Analysis of the Solar Proton Flares of September 2017 by Their Radio Bursts. *Geomagnetism and Aeronomy*, 58(4):457–463. → page 102
- Chu, K. R.
2004. The electron cyclotron maser. *Reviews of Modern Physics*, 76(2):489–540. → page 31
- Condon, J. J. and S. M. Ransom
2016. *Essential Radio Astronomy*. → pages 22, 26
- Connerney, J. E. P. and N. F. Ness
1988. *Mercury's magnetic field and interior.*, Pp. 494–513. → page 6
- Contopoulos, I.
2009. The pulsar synchrotron: coherent radio emission. *Astrophysics and Space Science*, 396(1):L6–L10. → page 36
- Cook, B. A., P. K. G. Williams, and E. Berger
2014. Trends in Ultracool Dwarf Magnetism. II. The Inverse Correlation Between X-Ray Activity and Rotation as Evidence for a Bimodal Dynamo. *Astrophysical Journal*, 785:10. → pages 20, 81
- Cowley, S. W. H. and E. J. Bunce
2001. Origin of the main auroral oval in Jupiter's coupled magnetosphere-ionosphere system. *Planetary Space Science*, 49(10-11):1067–1088. → page 58

- Cruz, K. L., I. N. Reid, J. Liebert, J. D. Kirkpatrick, and P. J. Lowrance
2003. Meeting the Cool Neighbors. V. A 2MASS-Selected Sample of Ultracool Dwarfs. *Astronomical Journal*, 126(5):2421–2448. → pages ix, 60
- Culhane, J. L.
1969. Thermal continuum radiation from coronal plasmas at soft X-ray wavelengths. *Astrophysics and Space Science*, 144:375. → page 26
- Débarbat, S., J. Lequeux, and W. Orchiston
2007. Highlighting the history of French radio astronomy. 1: Nordmann’s attempt to observe solar radio emission in 1901. *Journal of Astronomical History and Heritage*, 10(1):1–10. → page 21
- Delisle, J. B., A. C. M. Correia, A. Leleu, and P. Robutel
2017. Spin dynamics of close-in planets exhibiting large transit timing variations. *Astronomy and Astrophysics*, 605:A37. → page 6
- Delrez, L., M. Gillon, A. H. Triaud, B.-O. Demory, J. de Wit, J. G. Ingalls, E. Agol, E. Bolmont, A. Burdanov, A. J. Burgasser, et al.
2018. Early 2017 observations of trappist-1 with spitzer. *Monthly Notices of the Royal Astronomical Society*, 475(3):3577–3597. → page 75
- Dennis, B. R. and R. A. Schwartz
1989. Solar flares: The impulsive phase. *International Astronomical Union Colloquium*, 104(1):75–94. → page 115
- Drake, S. A., T. Simon, and J. L. Linsky
1992. Radio Continuum and X-Ray Properties of the Coronae of RS Canum Venaticorum and Related Active Binary Systems. *Astrophysical Journals*, 82:311. → pages xii, xvii, 18, 82
- Dressing, C. D. and D. Charbonneau
2015. The Occurrence of Potentially Habitable Planets Orbiting M Dwarfs Estimated from the Full Kepler Dataset and an Empirical Measurement of the Detection Sensitivity. *Astrophysical Journal*, 807(1):45. → pages 5, 58, 91
- Driscoll, P. E. and R. Barnes
2015. Tidal Heating of Earth-like Exoplanets around M Stars: Thermal, Magnetic, and Orbital Evolutions. *Astrobiology*, 15(9):739–760. → page 6
- Drummond, W. E., J. H. Malmberg, T. M. O’Neil, and J. R. Thompson
1970. Nonlinear Development of the Beam-Plasma Instability. *Physics of Fluids*, 13(9):2422–2425. → page 29

- Dulk, G. A.
1985. Radio emission from the sun and stars. *Annual Review of Astron and Astrophys*, 23:169–224. → pages 22, 33, 35, 39, 77, 84
- Dulk, G. A. and K. A. Marsh
1982. Simplified expressions for the gyrosynchrotron radiation from mildly relativistic, nonthermal and thermal electrons. *Astrophysical Journal*, 259:350–358. → pages xiii, 39, 41, 68
- Duric, N., E. Bourneuf, and P. C. Gregory
1988. The Separation of Synchrotron and Bremsstrahlung Radio Emission in Spiral Galaxies. *Astronomical Journal*, 96:81. → page 27
- Ergun, R. E., C. W. Carlson, J. P. McFadden, G. T. Delory, R. J. Strangeway, and P. L. Pritchett
2000. Electron-Cyclotron Maser Driven by Charged-Particle Acceleration from Magnetic Field-aligned Electric Fields. *Astrophysical Journal*, 538(1):456–466. → page 34
- Fleming, T. A., M. S. Giampapa, and J. H. M. M. Schmitt
2000. An X-Ray Flare Detected on the M8 Dwarf VB 10. *Astrophysical Journal*, 533(1):372–377. → pages 18, 81
- Forbrich, J., T. J. Dupuy, M. J. Reid, E. Berger, A. Rizzuto, A. W. Mann, M. C. Liu, K. Aller, and A. L. Kraus
2016. High-precision Radio and Infrared Astrometry of LSPM J1314+1320AB. I. Parallax, Proper Motions, and Limits on Planets. *Astrophysical Journal*, 827(1):22. → page 63
- Fuhrmann, K.
1998. Nearby stars of the Galactic disk and halo. *Astronomy and Astrophysics*, 338:161–183. → page 4
- Gaia Collaboration, A. G. A. Brown, A. Vallenari, T. Prusti, J. H. J. de Bruijne, C. Babusiaux, C. A. L. Bailer-Jones, M. Biermann, D. W. Evans, L. Eyer, F. Jansen, C. Jordi, S. A. Klioner, U. Lammers, L. Lindegren, X. Luri, F. Mignard, C. Panem, D. Pourbaix, S. Randich, P. Sartoretti, H. I. Siddiqui, C. Soubiran, F. van Leeuwen, N. A. Walton, F. Arenou, U. Bastian, M. Cropper, R. Drimmel, D. Katz, M. G. Lattanzi, J. Bakker, C. Cacciari, J. Castañeda, L. Chaoul, N. Cheek, F. De Angeli, C. Fabricius, R. Guerra, B. Holl, E. Masana, R. Messineo, N. Mowlavi, K. Nienartowicz, P. Panuzzo, J. Portell, M. Riello, G. M. Seabroke, P. Tanga, F. Thévenin, G. Gracia-Abril, G. Comoretto,

M. Garcia-Reinaldos, D. Teyssier, M. Altmann, R. Andrae, M. Audard,
 I. Bellas-Velidis, K. Benson, J. Berthier, R. Blomme, P. Burgess, G. Busso,
 B. Carry, A. Cellino, G. Clementini, M. Clotet, O. Creevey, M. Davidson, J. De
 Ridder, L. Delchambre, A. Dell'Oro, C. Ducourant, J. Fernández-Hernández,
 M. Fouesneau, Y. Frémat, L. Galluccio, M. García-Torres, J. González-Núñez,
 J. J. González-Vidal, E. Gosset, L. P. Guy, J. L. Halbwachs, N. C. Hambly,
 D. L. Harrison, J. Hernández, D. Hestroffer, S. T. Hodgkin, A. Hutton,
 G. Jasniewicz, A. Jean-Antoine-Piccolo, S. Jordan, A. J. Korn,
 A. Krone-Martins, A. C. Lanzafame, T. Lebzelter, W. Löffler, M. Manteiga,
 P. M. Marrese, J. M. Martín-Fleitas, A. Moitinho, A. Mora, K. Muinonen,
 J. Osinde, E. Pancino, T. Pauwels, J. M. Petit, A. Recio-Blanco, P. J. Richards,
 L. Rimoldini, A. C. Robin, L. M. Sarro, C. Siopis, M. Smith, A. Sozzetti,
 M. Süveges, J. Torra, W. van Reeve, U. Abbas, A. Abreu Aramburu, S. Accart,
 C. Aerts, G. Altavilla, M. A. Álvarez, R. Alvarez, J. Alves, R. I. Anderson,
 A. H. Andrei, E. Anglada Varela, E. Antiche, T. Antoja, B. Arcay, T. L.
 Astraatmadja, N. Bach, S. G. Baker, L. Balaguer-Núñez, P. Balm, C. Barache,
 C. Barata, D. Barbato, F. Barblan, P. S. Barklem, D. Barrado, M. Barros, M. A.
 Barstow, S. Bartholomé Muñoz, J. L. Bassilana, U. Becciani, M. Bellazzini,
 A. Berihuete, S. Bertone, L. Bianchi, O. Bienaymé, S. Blanco-Cuaresma,
 T. Boch, C. Boeche, A. Bombrun, R. Borrachero, D. Bossini, S. Bouquillon,
 G. Bourda, A. Bragaglia, L. Bramante, M. A. Breddels, A. Bressan,
 N. Brouillet, T. Brüsemeister, E. Brugaletta, B. Bucciarelli, A. Burlacu,
 D. Busonero, A. G. Butkevich, R. Buzzì, E. Caffau, R. Cancelliere,
 G. Cannizzaro, T. Cantat-Gaudin, R. Carballo, T. Carlucci, J. M. Carrasco,
 L. Casamiquela, M. Castellani, A. Castro-Ginard, P. Charlot, L. Chemin,
 A. Chiavassa, G. Cocozza, G. Costigan, S. Cowell, F. Crifo, M. Crosta,
 C. Crowley, J. Cuypers, C. Dafonte, Y. Damerdjì, A. Dapergolas, P. David,
 M. David, P. de Laverny, F. De Luise, R. De March, D. de Martino, R. de
 Souza, A. de Torres, J. Debosscher, E. del Pozo, M. Delbo, A. Delgado, H. E.
 Delgado, P. Di Matteo, S. Diakite, C. Diener, E. Distefano, C. Dolding,
 P. Drazinos, J. Durán, B. Edvardsson, H. Enke, K. Eriksson, P. Esquej,
 G. Eynard Bontemps, C. Fabre, M. Fabrizio, S. Faigler, A. J. Falcão, M. Farràs
 Casas, L. Federici, G. Fedorets, P. Fernique, F. Figueras, F. Filippi,
 K. Findeisen, A. Fonti, E. Fraile, M. Fraser, B. Frézouls, M. Gai, S. Galleti,
 D. Garabato, F. García-Sedano, A. Garofalo, N. Garralda, A. Gavel, P. Gavras,
 J. Gerssen, R. Geyer, P. Giacobbe, G. Gilmore, S. Girona, G. Giuffrida,
 F. Glass, M. Gomes, M. Granvik, A. Gueguen, A. Guerrier, J. Guiraud,
 R. Gutiérrez-Sánchez, R. Haigron, D. Hatzidimitriou, M. Hauser, M. Haywood,
 U. Heiter, A. Helmi, J. Heu, T. Hilger, D. Hobbs, W. Hofmann, G. Holland,
 H. E. Huckle, A. Hypki, V. Icardi, K. Janßen, G. Jevardat de Fombelle, P. G.

Jonker, Á. L. Juhász, F. Julbe, A. Karamelas, A. Kewley, J. Klar, A. Kochoska, R. Kohley, K. Kolenberg, M. Kontizas, E. Kontizas, S. E. Koposov, G. Kordopatis, Z. Kostrzewa-Rutkowska, P. Koubsky, S. Lambert, A. F. Lanza, Y. Lasne, J. B. Lavigne, Y. Le Fustec, C. Le Poncin-Lafitte, Y. Lebreton, S. Leccia, N. Leclerc, I. Lecoeur-Taibi, H. Lenhardt, F. Leroux, S. Liao, E. Licata, H. E. P. Lindstrøm, T. A. Lister, E. Livanou, A. Lobel, M. López, S. Managau, R. G. Mann, G. Mantelet, O. Marchal, J. M. Marchant, M. Marconi, S. Marinoni, G. Marschalló, D. J. Marshall, M. Martino, G. Marton, N. Mary, D. Massari, G. Matijević, T. Mazeh, P. J. McMillan, S. Messina, D. Michalik, N. R. Millar, D. Molina, R. Molinaro, L. Molnár, P. Montegriffo, R. Mor, R. Morbidelli, T. Morel, D. Morris, A. F. Mulone, T. Muraveva, I. Musella, G. Nelemans, L. Nicastro, L. Noval, W. O'Mullane, C. Ordénovic, D. Ordóñez-Blanco, P. Osborne, C. Pagani, I. Pagano, F. Pailler, H. Palacin, L. Palaversa, A. Panahi, M. Pawlak, A. M. Piersimoni, F. X. Pineau, E. Plachy, G. Plum, E. Poggio, E. Poujoulet, A. Prša, L. Pulone, E. Racero, S. Ragaini, N. Rambaux, M. Ramos-Lerate, S. Regibo, C. Reylé, F. Riclet, V. Ripepi, A. Riva, A. Rivard, G. Rixon, T. Roegiers, M. Roelens, M. Romero-Gómez, N. Rowell, F. Royer, L. Ruiz-Dern, G. Sadowski, T. Sagristà Sellés, J. Sahlmann, J. Salgado, E. Salguero, N. Sanna, T. Santana-Ros, M. Sarasso, H. Savietto, M. Schultheis, E. Sciacca, M. Segol, J. C. Segovia, D. Ségransan, I. C. Shih, L. Siltala, A. F. Silva, R. L. Smart, K. W. Smith, E. Solano, F. Solitro, R. Sordo, S. Soria Nieto, J. Souchay, A. Spagna, F. Spoto, U. Stampa, I. A. Steele, H. Steidelmüller, C. A. Stephenson, H. Stoev, F. F. Suess, J. Surdej, L. Szabados, E. Szegedi-Elek, D. Tapiador, F. Taris, G. Tauran, M. B. Taylor, R. Teixeira, D. Terrett, P. Teyssandier, W. Thuillot, A. Titarenko, F. Torra Clotet, C. Turon, A. Ulla, E. Utrilla, S. Uzzi, M. Vaillant, G. Valentini, V. Valette, A. van Elteren, E. Van Hemelryck, M. van Leeuwen, M. Vaschetto, A. Vecchiato, J. Veljanoski, Y. Viala, D. Vicente, S. Vogt, C. von Essen, H. Voss, V. Votruba, S. Voutsinas, G. Walmsley, M. Weiler, O. Wertz, T. Wevers, Ł. Wyrzykowski, A. Yoldas, M. Žerjal, H. Ziaeepour, J. Zorec, S. Zschocke, S. Zucker, C. Zurbach, and T. Zwitter
 2018. Gaia Data Release 2. Summary of the contents and survey properties. *Astronomy and Astrophysics*, 616:A1. → page 63

Garraffo, C., J. J. Drake, O. Cohen, J. D. Alvarado-Gómez, and S. P. Moschou
 2017. The Threatening Magnetic and Plasma Environment of the TRAPPIST-1 Planets. *Astrophysical Journal, Letters*, 843:L33. → page 76

Gary, D. E. and G. J. Hurford

1987. Multifrequency Observations of a Solar Active Region during a Partial Eclipse. *Astrophysical Journal*, 317:522. → page 38

Gerard, J. C. and C. A. Barth

1977. High-latitude nitric oxide in the lower thermosphere. *Journal of Geophysics Research*, 82(4):674. → page 96

Gillon, M., E. Jehin, S. M. Lederer, L. Delrez, J. de Wit, A. Burdanov,

V. Van Grootel, A. J. Burgasser, A. H. M. J. Triaud, C. Opitom, and et al.

2016. Temperate earth-sized planets transiting a nearby ultracool dwarf star. *Nature*, 533(7602):221–224. → pages 75, 85

Gillon, M., A. H. M. J. Triaud, B.-O. Demory, E. Jehin, E. Agol, K. M. Deck,

S. M. Lederer, J. de Wit, A. Burdanov, J. G. Ingalls, and et al.

2017. Seven temperate terrestrial planets around the nearby ultracool dwarf star trappist-1. *Nature*, 542(7642):456–460. → pages 74, 75, 76

Gilman, P. A.

2005. The tachocline and the solar dynamo. *Astronomische Nachrichten*, 326(2):208–217. → page 11

Ginzburg, V. L. and V. V. Zhelezniakov

1958. On the Possible Mechanisms of Sporadic Solar Radio Emission

(Radiation in an Isotropic Plasma). *Soviet Astronomy*, 2:653. → pages 28, 30

Girard, J. N., P. Zarka, C. Tasse, S. Hess, I. de Pater, D. Santos-Costa, Q. Nenon,

A. Sicard, S. Bourdarie, J. Anderson, A. Asgekar, M. E. Bell, I. van Bemmell,

M. J. Bentum, G. Bernardi, P. Best, A. Bonafede, F. Breitling, R. P. Breton,

J. W. Broderick, W. N. Brouw, M. Brüggen, B. Ciardi, S. Corbel, A. Corstanje,

F. de Gasperin, E. de Geus, A. Deller, S. Duscha, J. Eislöffel, H. Falcke,

W. Frieswijk, M. A. Garrett, J. Grießmeier, A. W. Gunst, J. W. T. Hessels,

M. Hoeft, J. Hörandel, M. Iacobelli, E. Juette, V. I. Kondratiev, M. Kuniyoshi,

G. Kuper, J. van Leeuwen, M. Loose, P. Maat, G. Mann, S. Markoff,

R. McFadden, D. McKay-Bukowski, J. Moldon, H. Munk, A. Nelles, M. J.

Norden, E. Orru, H. Paas, M. Pandey-Pommier, R. Pizzo, A. G. Polatidis,

W. Reich, H. Röttgering, A. Rowlinson, D. Schwarz, O. Smirnov, M. Steinmetz,

J. Swinbank, M. Tagger, S. Thoudam, M. C. Toribio, R. Vermeulen, C. Vocks,

R. J. van Weeren, R. A. M. J. Wijers, and O. Wucknitz

2016. Imaging Jupiter’s radiation belts down to 127 MHz with LOFAR.

Astronomy and Astrophysics, 587:A3. → page 38

- Girard, P. and C. Soubiran
2006. *Abundances and Ages of the Deconvolved Thin/Thick Disks of the Galaxy*, P. 56. → page 4
- Gizis, J. E., D. G. Monet, I. N. Reid, J. D. Kirkpatrick, J. Liebert, and R. J. Williams
2000. New Neighbors from 2MASS: Activity and Kinematics at the Bottom of the Main Sequence. *Astronomical Journal*, 120(2):1085–1099. → pages ix, 60, 74
- Gopalswamy, N., P. Mäkelä, S. Yashiro, S. Akiyama, H. Xie, and N. Thakur
2020. Source of Energetic Protons in the 2014 September 1 Sustained Gamma-ray Emission Event. *Solar Physics*, 295(2):18. → page 105
- Green, J., D. Draper, S. Boardsen, and C. Dong
2020. When the moon had a magnetosphere. *Science Advances*, 6(42). → page 6
- Grißmeier, J.-M., A. Stadelmann, T. Penz, H. Lammer, F. Selsis, I. Ribas, E. F. Guinan, U. Motschmann, H. K. Biernat, and W. W. Weiss
2004a. The effect of tidal locking on the magnetospheric and atmospheric evolution of “Hot Jupiters”. *Astronomy and Astrophysics*, 425:753–762. → page 6
- Grißmeier, J. M., A. Stadelmann, T. Penz, H. Lammer, F. Selsis, I. Ribas, E. F. Guinan, U. Motschmann, H. K. Biernat, and W. W. Weiss
2004b. The effect of tidal locking on the magnetospheric and atmospheric evolution of “Hot Jupiters”. *Astronomy and Astrophysics*, 425:753–762. → page 6
- Güdel, M.
1992. Radio and X-ray emission from main-sequence K stars. *Astronomy and Astrophysics*, 264:L31–L34. → pages xii, xvii, 18, 82
- Güdel, M.
2002. Stellar Radio Astronomy: Probing Stellar Atmospheres from Protostars to Giants. *Annual Review of Astron and Astrophys*, 40:217–261. → page 40
- Güdel, M. and A. O. Benz
1993. X-Ray/Microwave Relation of Different Types of Active Stars. *Astrophysical Journal, Letters*, 405:L63. → pages xii, 17, 18

- Güdel, M., J. H. M. M. Schmitt, J. A. Bookbinder, and T. A. Fleming
1993. A tight correlation between radio and X-ray luminosities of M dwarfs. *Astrophysical Journal*, 415:236–239. → pages xvii, 82
- Gurnett, D. A. and R. R. Anderson
1981. The kilometric radio emission spectrum: Relationship to auroral acceleration processes. *Washington DC American Geophysical Union Geophysical Monograph Series*, 25:341–350. → page 34
- Haddock, F. T.
1984. U. S. Radio Astronomy Following World War II. In *Serendipitous Discoveries in Radio Astronomy*, P. 115. → page 21
- Hallinan, G., A. Antonova, J. G. Doyle, S. Bourke, W. F. Briskin, and A. Golden
2006. Rotational Modulation of the Radio Emission from the M9 Dwarf TVLM 513-46546: Broadband Coherent Emission at the Substellar Boundary? *Astrophysical Journal*, 653(1):690–699. → pages 38, 58
- Hallinan, G., A. Antonova, J. G. Doyle, S. Bourke, C. Lane, and A. Golden
2008. Confirmation of the Electron Cyclotron Maser Instability as the Dominant Source of Radio Emission from Very Low Mass Stars and Brown Dwarfs. *Astrophysical Journal*, 684(1):644–653. → pages 30, 35, 60, 62, 68
- Hallinan, G., S. Bourke, C. Lane, A. Antonova, R. T. Zavala, W. F. Briskin, R. P. Boyle, F. J. Vrba, J. G. Doyle, and A. Golden
2007. Periodic Bursts of Coherent Radio Emission from an Ultracool Dwarf. *Astrophysical Journal, Letters*, 663:L25–L28. → pages 81, 112
- Hart, M.
1980. *Habitable Zones about Main Sequence Stars*, P. 236. → page 92
- Hawley, S. L., G. H. Fisher, T. Simon, S. L. Cully, S. E. Deustua, M. Jablonski, C. M. Johns-Krull, B. R. Pettersen, V. Smith, W. J. Spiesman, and J. Valenti
1995. Simultaneous Extreme-Ultraviolet Explorer and Optical Observations of AD Leonis: Evidence for Large Coronal Loops and the Neupert Effect in Stellar Flares. *Astrophysical Journal*, 453:464. → page 116
- He, H. Q., G. Zhou, and W. Wan
2017. Propagation of Solar Energetic Particles in Three-dimensional Interplanetary Magnetic Fields: Radial Dependence of Peak Intensities. *Astrophysical Journal*, 842(2):71. → page 98

- Heller, R., J. Leconte, and R. Barnes
2011. Tidal obliquity evolution of potentially habitable planets. *Astronomy and Astrophysics*, 528:A27. → page 6
- Henry, T. J., W.-C. Jao, J. P. Subasavage, T. D. Beaulieu, P. A. Ianna, E. Costa, and R. A. Méndez
2006. The Solar Neighborhood. XVII. Parallax Results from the CTIOPI 0.9 m Program: 20 New Members of the RECONS 10 Parsec Sample. *Astronomical Journal*, 132(6):2360–2371. → pages 2, 57
- Herbig, G. H.
1956. Observations of the Spectrum of the Companion to BD + 4°4048. , 68(405):531. → page 18
- Hey, J. S.
1946. Solar Radiations in the 4-6 Metre Radio Wave-Length Band. *Nature*, 157(3976):47–48. → page 22
- Högbom, J. A.
1974. Aperture Synthesis with a Non-Regular Distribution of Interferometer Baselines. *Astronomy and Astrophysics, Supplement*, 15:417. → page 54
- Hood, L. L. and J. P. McCormack
1992. components of interannual ozone change based on NIMBUS 7 TOMS data. *Geophysics Research Letters*, 19(23):2309–2312. → page 96
- Hughes, A. G., A. C. Boley, R. A. Osten, and J. A. White
2019. Constraining the Radio Emission of TRAPPIST-1. *Astrophysical Journal*, 881(1):33. → page 40
- Iben, Icko, J.
1967. Stellar Evolution Within and off the Main Sequence. *Annual Review of Astron and Astrophys*, 5:571. → page 4
- Iwagami, N. and T. Ogawa
1980. An Antarctic no density profile deduced from the gamma band airglow. *Planetary Space Science*, 28(8):867–873. → page 96
- Jackman, C. H., M. T. Deland, G. J. Labow, E. L. Fleming, D. K. Weisenstein, M. K. W. Ko, M. Sinnhuber, J. Anderson, and J. M. Russell
2005. The influence of the several very large solar proton events in years 2000 2003 on the neutral middle atmosphere. *Advances in Space Research*, 35(3):445–450. → page 96

- Jackson, R. J. and R. D. Jeffries
2013. On the relationship between the size and surface coverage of starspots on magnetically active low-mass stars. *Astrophysics and Space Science*, 431(2):1883–1890. → page 6
- Jardine, M. and Y. C. Unruh
1999. Coronal emission and dynamo saturation. *Astronomy and Astrophysics*, 346:883–891. → page 20
- Johns-Krull, C. M. and J. A. Valenti
1996. Detection of Strong Magnetic Fields on M Dwarfs. *Astrophysical Journal, Letters*, 459:L95. → page 71
- Joshi, N. C., W. Uddin, A. K. Srivastava, R. Chandra, N. Gopalswamy, P. K. Manoharan, M. J. Aschwanden, D. P. Choudhary, R. Jain, N. V. Nitta, H. Xie, S. Yashiro, S. Akiyama, P. Mäkelä, P. Kayshap, A. K. Awasthi, V. C. Dwivedi, and K. Mahalakshmi
2013. A multiwavelength study of eruptive events on January 23, 2012 associated with a major solar energetic particle event. *Advances in Space Research*, 52(1):1–14. → pages x, 102
- Kallunki, J. and M. Uunila
2017. Sizes of solar active regions at 8 mm. *Astronomische Nachrichten*, 338(4):398–406. → page 100
- Kane, S. R.
2018. The Impact of Stellar Distances on Habitable Zone Planets. *Astrophysical Journal*, 861:L21. → pages 74, 75
- Kao, M. M.
2017. *Constraining Substellar Magnetic Dynamos using Brown Dwarf Radio Aurorae*. PhD thesis, California Institute of Technology. → page 11
- Kao, M. M., G. Hallinan, and J. S. Pineda
2019. Constraints on magnetospheric radio emission from Y dwarfs. *Astrophysics and Space Science*, 487(2):1994–2004. → page 72
- Kao, M. M., G. Hallinan, J. S. Pineda, I. Escala, A. Burgasser, S. Bourke, and D. Stevenson
2016. Auroral Radio Emission from Late L and T Dwarfs: A New Constraint on Dynamo Theory in the Substellar Regime. *Astrophysical Journal*, 818(1):24. → page 58

- Kasting, J. F., D. P. Whitmire, and R. T. Reynolds
1993. Habitable Zones around Main Sequence Stars. *Icarus*, 101(1):108–128.
→ page 6
- Kellermann, K. I., E. N. Bouton, and S. S. Brandt
2020. *The Very Large Array*, Pp. 319–390. Cham: Springer International Publishing. → page 50
- Khodachenko, M. L., H. Lammer, H. I. M. Lichtenegger, J.-M. Grießmeier, M. Holmström, and A. Ekenbäck
2009. The role of intrinsic magnetic fields in planetary evolution and habitability: the planetary protection aspect. In *Cosmic Magnetic Fields: From Planets, to Stars and Galaxies*, K. G. Strassmeier, A. G. Kosovichev, and J. E. Beckman, eds., volume 259 of *IAU Symposium*, Pp. 283–294. → page 6
- Kilic, M., J. A. Munn, H. C. Harris, T. von Hippel, J. W. Liebert, K. A. Williams, E. Jeffery, and S. DeGennaro
2017. The Ages of the Thin Disk, Thick Disk, and the Halo from Nearby White Dwarfs. *Astrophysical Journal*, 837(2):162. → page 4
- Kirkpatrick, J. D., T. J. Henry, and M. J. Irwin
1997. Ultra-Cool M Dwarfs Discovered by QSO Surveys.I: The APM Objects. *Astronomical Journal*, 113:1421–1428. → page 9
- Klein, U., U. Lisenfeld, and S. Verley
2018. Radio synchrotron spectra of star-forming galaxies. *Astronomy and Astrophysics*, 611:A55. → pages 36, 102
- Konopacky, Q. M., A. M. Ghez, T. S. Barman, E. L. Rice, J. I. Bailey, R. J. White, I. S. McLean, and G. Duchêne
2010. High-precision dynamical masses of very low mass binaries. *The Astrophysical Journal*, 711(2):1087–1122. → pages ix, 60
- Konopacky, Q. M., A. M. Ghez, D. C. Fabrycky, B. A. Macintosh, R. J. White, T. S. Barman, E. L. Rice, G. Hallinan, and G. Duchêne
2012. Rotational Velocities of Individual Components in Very Low Mass Binaries. *Astrophysical Journal*, 750:79. → pages ix, 60, 65, 67
- Kopp, R. A. and G. W. Pneuman
1976. Magnetic reconnection in the corona and the loop prominence phenomenon. *Solar Physics*, 50(1):85–98. → page 115

- Kruse, U. E., L. Marshall, and J. R. Platt
1956. Synchrotron Radiation in the Sun's Radio Spectrum. *Astrophysical Journal*, 124:601. → page 38
- Küker, M. and G. Rüdiger
1999. Magnetic field generation in weak-line T Tauri stars: an alpha (2)-dynamo. *Astronomy and Astrophysics*, 346:922–928. → page 16
- Kumar, S. S.
1962. Study of Degeneracy in Very Light Stars. *Astronomical Journal*, 67:579. → page 7
- Kundu, M. R., A. Nindos, S. M. White, and V. V. Grechnev
2001. A Multiwavelength Study of Three Solar Flares. *Astrophysical Journal*, 557(2):880–890. → page 38
- La Mura, G., G. Busetto, S. Ciroi, P. Rafanelli, M. Berton, E. Congiu, V. Cracco, and M. Frezzato
2017. Relativistic plasmas in AGN jets. From synchrotron radiation to γ -ray emission. *European Physical Journal D*, 71(4):95. → page 36
- Lario, D., A. Aran, R. Gómez-Herrero, N. Dresing, B. Heber, G. C. Ho, R. B. Decker, and E. C. Roelof
2013. Longitudinal and Radial Dependence of Solar Energetic Particle Peak Intensities: STEREO, ACE, SOHO, GOES, and MESSENGER Observations. *Astrophysical Journal*, 767:41. → page 98
- Lario, D., M. B. Kallenrode, R. B. Decker, E. C. Roelof, S. M. Krimigis, A. Aran, and B. Sanahuja
2006. Radial and Longitudinal Dependence of Solar 4-13 MeV and 27-37 MeV Proton Peak Intensities and Fluences: Helios and IMP 8 Observations. *Astrophysical Journal*, 653(2):1531–1544. → page 98
- Laughlin, G., P. Bodenheimer, and F. C. Adams
1997. The End of the Main Sequence. *Astrophysical Journal*, 482(1):420–432. → page 4
- Law, N. M., S. T. Hodgkin, and C. D. Mackay
2006. Discovery of five very low mass close binaries, resolved in the visible with lucky imaging*. *Astrophysics and Space Science*, 368(4):1917–1924. → page 63

- Leconte, J., H. Wu, K. Menou, and N. Murray
2015. Asynchronous rotation of Earth-mass planets in the habitable zone of lower-mass stars. *Science*, 347(6222):632–635. → page 6
- Lépine, S., J. R. Thorstensen, M. M. Shara, and R. M. Rich
2009. New Neighbors: Parallaxes of 18 Nearby Stars Selected from the LSPM-North Catalog. *Astronomical Journal*, 137(5):4109–4117. → pages ix, 60, 63, 64
- Limber, D. N.
1953. The Analysis of Counts of the Extragalactic Nebulae in Terms of a Fluctuating Density Field. *Astrophysical Journal*, 117:134. → page 10
- Linsky, J. L., C. Andrusis, S. H. Saar, T. R. Ayres, and M. S. Giampapa
1994. The Relationship Between Radiative and Magnetic Fluxes on Three Active Solar-type Dwarfs. In *Cool Stars, Stellar Systems, and the Sun*, J.-P. Caillault, ed., volume 64 of *Astronomical Society of the Pacific Conference Series*. → page 81
- Linsky, J. L., B. E. Wood, A. Brown, M. S. Giampapa, and C. Ambruster
1995. Stellar Activity at the End of the Main Sequence: GHRS Observations of the M8 Ve Star VB 10. *Astrophysical Journal*, 455:670. → page 18
- Longair, M. S.
2011. *High Energy Astrophysics*. → page 36
- Loyd, R. O. P., E. L. Shkolnik, A. C. Schneider, T. S. Barman, V. S. Meadows, I. Pagano, and S. Peacock
2018. HAZMAT. IV. Flares and Superflares on Young M Stars in the Far Ultraviolet. *Astrophysical Journal*, 867(1):70. → page 6
- Luger, R., M. Sestovic, E. Kruse, S. L. Grimm, B.-O. Demory, E. Agol, E. Bolmont, D. Fabrycky, C. S. Fernandes, V. Van Grootel, A. Burgasser, M. Gillon, J. G. Ingalls, E. Jehin, S. N. Raymond, F. Selsis, A. H. M. J. Triaud, T. Barclay, G. Barentsen, S. B. Howell, L. Delrez, J. de Wit, D. Foreman-Mackey, D. L. Holdsworth, J. Leconte, S. Lederer, M. Turbet, Y. Almleaky, Z. Benkhaldoun, P. Magain, B. M. Morris, K. Heng, and D. Queloz
2017. A seven-planet resonant chain in TRAPPIST-1. *Nature Astronomy*, 1:0129. → page 86
- Lunine, J. I., D. Fischer, H. B. Hammel, T. Henning, L. Hillenbrand, J. Kasting, G. Laughlin, B. Macintosh, M. Marley, G. Melnick, D. Monet, C. Noecker,

S. Peale, A. Quirrenbach, S. Seager, and J. N. Winn
2008. Worlds Beyond: A Strategy for the Detection and Characterization of Exoplanets Executive Summary of a Report of the ExoPlanet Task Force Astronomy and Astrophysics Advisory Committee Washington, DC June 23, 2008. *Astrobiology*, 8(5):875–881. → page 94

Lynch, C., T. Murphy, V. Ravi, G. Hobbs, K. Lo, and C. Ward
2016. Radio detections of southern ultracool dwarfs. *Astrophysics and Space Science*, 457(2):1224–1232. → pages 1, 19, 58

MacGregor, A. M., R. A. Osten, and A. M. Hughes
2020. Properties of M Dwarf Flares at Millimeter Wavelengths. *Astrophysical Journal*, 891(1):80. → page 38

MacGregor, M. A., A. J. Weinberger, D. J. Wilner, A. F. Kowalski, and S. R. Cranmer
2018. Detection of a Millimeter Flare from Proxima Centauri. *Astrophysical Journal, Letters*, 855(1):L2. → page 85

MacPherson, H.
1920. Recent Theories of Stellar Evolution. *Popular Astronomy*, 28:225–231. → page 2

McLean, M., E. Berger, J. Irwin, J. Forbrich, and A. Reiners
2011. Periodic Radio Emission from the M7 Dwarf 2MASS J13142039+1320011: Implications for the Magnetic Field Topology. *Astrophysical Journal*, 741(1):27. → pages ix, 60, 63, 64, 66, 68

McLean, M., E. Berger, and A. Reiners
2012. The Radio Activity-Rotation Relation of Ultracool Dwarfs. *Astrophysical Journal*, 746:23. → pages 19, 58, 61, 83, 112

McMullin, J., B. Waters, D. Schiebel, W. Young, and K. Golap
2007. Casa architecture and applications. In *Astronomical data analysis software and systems XVI*, volume 376, P. 127. → pages 61, 77, 86

Melrose, D. B.
1991. Collective plasma radiation processes. *Annual Review of Astron and Astrophys*, 29:31–57. → pages xii, 28

Melrose, D. B., G. A. Dulk, and D. E. Gary
1980. Corrected formula for the polarization of second harmonic plasma emission. *Proceedings of the Astronomical Society of Australia*, 4(1):50–53. → page 33

- Melrose, D. B. and M. S. Wheatland
2016. Is Cyclotron Maser Emission in Solar Flares Driven by a Horseshoe Distribution? *Solar Physics*, 291(12):3637–3658. → page 35
- Miesch, M. S., M. K. Browning, A. S. Brun, J. Toomre, and B. P. Brown
2009. Three-Dimensional Simulations of Solar and Stellar Dynamos: The Influence of a Tachocline. In *Solar-Stellar Dynamos as Revealed by Helio- and Asteroseismology: GONG 2008/SOHO 21*, M. Dikpati, T. Arentoft, I. González Hernández, C. Lindsey, and F. Hill, eds., volume 416 of *Astronomical Society of the Pacific Conference Series*, P. 443. → page 12
- Miguel, Y., A. Cridland, C. W. Ormel, J. J. Fortney, and S. Ida
2020. Diverse outcomes of planet formation and composition around low-mass stars and brown dwarfs. *Astrophysics and Space Science*, 491(2):1998–2009. → page 5
- Miroshnichenko, L. I. and R. A. Nymmik
2014. Extreme fluxes in solar energetic particle events: Methodological and physical limitations. *Radiation Measurements*, 61:6–15. → page 100
- Morin, J., J.-F. Donati, P. Petit, X. Delfosse, T. Forveille, and M. M. Jardine
2010. Large-scale magnetic topologies of late M dwarfs*. *Astrophysics and Space Science*, 407:2269–2286. → page 83
- Morris, B. M., E. Agol, J. R. A. Davenport, and S. L. Hawley
2018. Possible Bright Starspots on TRAPPIST-1. *Astrophysical Journal*, 857(1):39. → pages 86, 106
- Neal, J. J., C. J. Rodger, and J. C. Green
2013. Empirical determination of solar proton access to the atmosphere: Impact on polar flight paths. *Space Weather*, 11(7):420–433. → pages x, 102
- Neupert, W. M.
1968. Comparison of Solar X-Ray Line Emission with Microwave Emission during Flares. *Astrophysical Journal, Letters*, 153:L59. → page 115
- Newton, E., J. Irwin, D. Charbonneau, P. Berlind, C. Michael, J. Mink, Z. Berta-Thompson, J. Dittmann, and A. West
2017. Age, rotation, and activity in M dwarfs and the implications for planet-hosting stars. In *Radio Exploration of Planetary Habitability (AASTCS5)*, volume 49, P. 101.02. → page 5

- Newton, E. R., J. Irwin, D. Charbonneau, Z. K. Berta-Thompson, J. A. Dittmann, and A. A. West
2016. The Rotation and Galactic Kinematics of Mid M Dwarfs in the Solar Neighborhood. *Astrophysical Journal*, 821(2):93. → page 4
- Nichols, J. D., M. R. Burleigh, S. L. Casewell, S. W. H. Cowley, G. A. Wynn, J. T. Clarke, and A. A. West
2012. Origin of Electron Cyclotron Maser Induced Radio Emissions at Ultracool Dwarfs: Magnetosphere-Ionosphere Coupling Currents. *Astrophysical Journal*, 760(1):59. → page 35
- Nindos, A.
2020. Incoherent Solar Radio Emission. *Frontiers in Astronomy and Space Sciences*, 7:57. → page 38
- O’Neal, D., J. E. Neff, S. H. Saar, and M. Cuntz
2004. Further Results of TiO-Band Observations of Starspots. *Astronomical Journal*, 128(4):1802–1811. → page 5
- Osten, R. A., S. L. Hawley, J. Allred, C. M. Johns-Krull, C. Roark, C. Ambruster, A. Brown, T. R. Ayres, and J. L. Linsky
2004. Multi-Wavelength Observations of EV Lacertae. In *Stars as Suns : Activity, Evolution and Planets*, A. K. Dupree and A. O. Benz, eds., volume 219 of *IAU Symposium*, P. 249. → pages 114, 116
- Osten, R. A., A. Kowalski, S. A. Drake, H. Krimm, K. Page, K. Gazeas, J. Kennea, S. Oates, M. Page, E. de Miguel, R. Novák, T. Apeltauer, and N. Gehrels
2016. A Very Bright, Very Hot, and Very Long Flaring Event from the M Dwarf Binary System DG CVn. *Astrophysical Journal*, 832(2):174. → page 40
- Osten, R. A., C. Melis, B. Stelzer, K. W. Bannister, J. Radigan, A. J. Burgasser, A. Wolszczan, and K. L. Luhman
2015. The Deepest Constraints on Radio and X-Ray Magnetic Activity in Ultracool Dwarfs from WISE J104915.57-531906.1. *Astrophysical Journal, Letters*, 805(1):L3. → page 40
- Osten, R. A., N. Phan-Bao, S. L. Hawley, I. N. Reid, and R. Ojha
2009. Steady and Transient Radio Emission from Ultracool Dwarfs. *Astrophysical Journal*, 700:1750–1758. → pages 38, 61, 83
- Paasilta, M., O. Raukunen, R. Vainio, E. Valtonen, A. Papaioannou, R. Siipola, E. Riihonen, M. Dierckxsens, N. Crosby, O. Malandraki, B. Heber, and K.-L.

Klein

2017. Catalogue of 55-80 MeV solar proton events extending through solar cycles 23 and 24. *Journal of Space Weather and Space Climate*, 7:A14. → pages x, 102

Parker, E. N.

1955. Hydromagnetic Dynamo Models. *Astrophysical Journal*, 122:293. → page 14

Parker, E. N.

1993. A Solar Dynamo Surface Wave at the Interface between Convection and Nonuniform Rotation. *Astrophysical Journal*, 408:707. → page 12

Penzias, A. A. and R. W. Wilson

1965. A Measurement of Excess Antenna Temperature at 4080 Mc/s. *Astrophysical Journal*, 142:419–421. → page 44

Perryman, M. A. C., L. Lindegren, J. Kovalevsky, E. Hog, U. Bastian, P. L.

Bernacca, M. Creze, F. Donati, M. Grenon, M. Grewing, F. van Leeuwen, H. van der Marel, F. Mignard, C. A. Murray, R. S. Le Poole, H. Schrijver, C. Turon, F. Arenou, M. Froeschle, and C. S. Petersen

1997. The Hipparcos Catalogue. *Astronomy and Astrophysics*, 500:501–504. → page 9

Phan-Bao, N., R. A. Osten, J. Lim, E. L. Martín, and P. T. P. Ho

2007. Discovery of Radio Emission from the Tight M8 Binary LP 349-25. *Astrophysical Journal*, 658:553–556. → page 60

Pineda, J. S.

2017. *Multiwavelength Characterization of the Brown Dwarf Auroral Phenomenon - Establishing the Nature of the Electrodynamical Engine*. PhD thesis, California Institute of Technology. → pages 58, 68, 72, 81, 112

Pineda, J. S. and G. Hallinan

2018. A Deep Radio Limit for the TRAPPIST-1 System. *Astrophysical Journal*, 866:155. → pages ix, xvii, xviii, 78, 80, 82, 83, 84

Pineda, J. S., G. Hallinan, and M. M. Kao

2017. A Panchromatic View of Brown Dwarf Aurorae. *Astrophysical Journal*, 846(1):75. → page 35

Priest, E. R. and T. G. Forbes

2002. The magnetic nature of solar flares. *Astronomy and Astrophysics*, 10(4):313–377. → page 115

- Priest, E. R., V. S. Titov, G. E. Vekestein, and G. J. Rikard
1994. Steady linear X-point magnetic reconnection. *Journal of Geophysics Research*, 99(A11):21,467–21,480. → page 115
- Pritchett, P. L.
1986. Electron-cyclotron maser instability in relativistic plasmas. *Physics of Fluids*, 29(9):2919–2930. → page 34
- Ramaty, R.
1969. Gyrosynchrotron Emission and Absorption in a Magnetoactive Plasma. *Astrophysical Journal*, 158:753. → pages 38, 39
- Ranjan, S. and D. D. Sasselov
2016. Influence of the UV Environment on the Synthesis of Prebiotic Molecules. *Astrobiology*, 16(1):68–88. → pages 41, 76
- Rayleigh, L.
1880. Investigations in optics, with special reference to the spectroscope. *Astrophysics and Space Science*, 40:254. → page 44
- Rebolo, R., E. L. Martin, G. Basri, G. W. Marcy, and M. R. Zapatero-Osorio
1996. Brown Dwarfs in the Pleiades Cluster Confirmed by the Lithium Test. *Astrophysical Journal, Letters*, 469:L53. → page 8
- Rebolo, R., M. R. Zapatero Osorio, and E. L. Martín
1995. Discovery of a brown dwarf in the Pleiades star cluster. *Nature*, 377(6545):129–131. → page 7
- Rees, M. H.
1989. *Physics and chemistry of the upper atmosphere*. → page 43
- Reid, H. A. S. and H. Ratcliffe
2014. A review of solar type III radio bursts. *Research in Astronomy and Astrophysics*, 14(7):773–804. → page 30
- Reid, I. N., K. L. Cruz, S. P. Laurie, J. Liebert, C. C. Dahn, H. C. Harris, H. H. Guetter, R. C. Stone, B. Canzian, C. B. Luginbuhl, S. E. Levine, A. K. B. Monet, and D. G. Monet
2003. Meeting the Cool Neighbors. IV. 2MASS 1835+32, a Newly Discovered M8.5 Dwarf within 6 Parsecs of the Sun. *Astronomical Journal*, 125:354–358. → pages ix, 60, 62

- Reid, I. N., J. D. Kirkpatrick, J. E. Gizis, and J. Liebert
1999. BRI 0021-0214: Another Surprise at the Bottom of the Main Sequence. *Astrophysical Journal, Letters*, 527(2):L105–L107. → pages 18, 81
- Reid, N., S. L. Hawley, and M. Mateo
1995. Chromospheric and coronal activity in low-mass Hyades dwarfs. *Astrophysics and Space Science*, 272(4):828–842. → page 5
- Reiners, A.
2009. Magnetic field observations of low-mass stars. In *Cosmic Magnetic Fields: From Planets, to Stars and Galaxies*, K. G. Strassmeier, A. G. Kosovichev, and J. E. Beckman, eds., volume 259, Pp. 339–344. → page 58
- Reiners, A. and G. Basri
2006. Measuring Magnetic Fields in Ultracool Stars and Brown Dwarfs. *Astrophysical Journal*, 644(1):497–509. → page 58
- Reiners, A. and G. Basri
2010. A Volume-Limited Sample of 63 M7-M9.5 Dwarfs. II. Activity, Magnetism, and the Fade of the Rotation-Dominated Dynamo. *Astrophysical Journal*, 710:924–935. → pages ix, xviii, 58, 60, 66, 74, 75, 81, 84
- Reiners, A., M. Zechmeister, J. A. Caballero, I. Ribas, J. C. Morales, S. V. Jeffers, P. Schofer, L. Tal-Or, A. Quirrenbach, P. J. Amado, A. Kaminski, W. Seifert, M. Abril, J. Aceituno, F. J. Alonso-Floriano, M. Ammler-von Eiff, R. Antona, G. Anglada-Escude, H. Anwand-Heerwart, B. Arroyo-Torres, M. Azzaro, D. Baroch, D. Barrado, F. F. Bauer, S. Becerril, V. J. S. Bejar, D. Benitez, Z. M. Berdinas, G. Bergond, M. Blumcke, M. Brinkmoller, C. Del Burgo, J. Cano, M. C. Cardenas Vazquez, E. Casal, C. Cifuentes, A. Claret, J. Colome, M. Cortes-Contreras, S. Czesla, E. Diez-Alonso, S. Dreizler, C. Feiz, M. Fernandez, I. M. Ferro, B. Fuhrmeister, D. Galadi-Enriquez, A. Garcia-Piquer, M. L. Garcia Vargas, L. Gesa, V. Gomez Galera, J. I. Gonzalez Hernandez, R. Gonzalez-Peinado, U. Grozinger, S. Grohnert, J. Guardia, E. W. Guenther, A. Guijarro, E. de Guindos, J. Gutierrez-Soto, H.-J. Hagen, A. P. Hatzes, P. H. Hauschildt, R. P. Hedrosa, J. Helmling, T. Henning, I. Hermelo, R. Hernandez Arabi, L. Hernandez Castano, F. Hernandez Hernando, E. Herrero, A. Huber, P. Huke, E. N. Johnson, E. de Juan, M. Kim, R. Klein, J. Kluter, A. Klutsch, M. Kurster, M. Lafarga, A. Lamert, M. Lampon, L. M. Lara, W. Laun, U. Lemke, R. Lenzen, R. Launhardt, M. Lopez Del Fresno, J. Lopez-Gonzalez, M. Lopez-Puertas, J. F. Lopez Salas, J. Lopez-Santiago, R. Luque, H. Magan Madinabeitia, U. Mall, L. Mancini, H. Mandel, E. Marfil, J. A. Marin Molina, D. Maroto Fernandez, E. L. Martin,

S. Martin-Ruiz, C. J. Marvin, R. J. Mathar, E. Mirabet, D. Montes, M. E. Moreno-Raya, A. Moya, R. Mundt, E. Nagel, V. Naranjo, L. Nortmann, G. Nowak, A. Ofir, R. Oreiro, E. Palle, J. Panduro, J. Pascual, V. M. Passegger, A. Pavlov, S. Pedraz, A. Perez-Calpena, D. Perez Medialdea, M. Perger, M. A. C. Perryman, M. Pluto, O. Rabaza, A. Ramon, R. Rebolo, P. Redondo, S. Reffert, S. Reinhard, P. Rhode, H.-W. Rix, F. Rodler, E. Rodriguez, C. Rodriguez-Lopez, A. Rodriguez Trinidad, R.-R. Rohloff, A. Rosich, S. Sadegi, E. Sanchez-Blanco, M. A. Sanchez Carrasco, A. Sanchez-Lopez, J. Sanz-Forcada, P. Sarkis, L. F. Sarmiento, S. Schafer, J. H. M. M. Schmitt, J. Schiller, A. Schweitzer, E. Solano, O. Stahl, J. B. P. Strachan, J. Sturmer, J. C. Suarez, H. M. Tabernero, M. Tala, T. Trifonov, S. M. Tulloch, R. G. Ulbrich, G. Veredas, J. I. Vico Linares, F. Vilardell, K. Wagner, J. Winkler, V. Wolthoff, W. Xu, F. Yan, and M. R. Zapatero Osorio
 2018. VizieR Online Data Catalog: 324 CARMENES M dwarfs velocities (Reiners+, 2018). *VizieR Online Data Catalog*, 361. → page 75

Route, M. and A. Wolszczan
 2016. The Second Arecibo Search for 5 GHz Radio Flares from Ultracool Dwarfs. *Astrophysical Journal*, 830(2):85. → pages 1, 19, 58

Ruediger, G.
 1978. On the alpha-effect for slow and fast rotation. *Astronomische Nachrichten*, 299(4):217–222. → page 16

Rutledge, R. E., G. Basri, E. L. Martín, and L. Bildsten
 2000. Chandra Detection of an X-Ray Flare from the Brown Dwarf LP 944-20. *Astrophysical Journal, Letters*, 538(2):L141–L144. → page 19

Rycroft, M. J., R. G. Harrison, K. A. Nicoll, and E. A. Mareev
 2008. An Overview of Earth’s Global Electric Circuit and Atmospheric Conductivity. *Space Science Reviews*, 137(1-4):83–105. → page 35

Sagan, C. and B. N. Khare
 1971. Long-Wavelength Ultraviolet Photoproduction of Amino Acids on the Primitive Earth. *Science*, 173(3995):417–420. → page 76

Sarker, P. K., J.-i. Takahashi, Y. Obayashi, T. Kaneko, and K. Kobayashi
 2013. Photo-alteration of hydantoins against UV light and its relevance to prebiotic chemistry. *Advances in Space Research*, 51(12):2235–2240. → page 76

Schlieder, J. E., M. Bonnefoy, T. M. Herbst, S. Lépine, E. Berger, T. Henning, A. Skemer, G. Chauvin, E. Rice, B. Biller, J. H. V. Girard, A.-M. Lagrange,

P. Hinz, D. Defrère, C. Bergfors, W. Brandner, S. Lacour, M. Skrutskie, and J. Leisenring
2014. Characterization of the Benchmark Binary NLTT 33370. *Astrophysical Journal*, 783(1):27. → pages ix, 60

Schmidt, S. J., K. L. Cruz, B. J. Bongiorno, J. Liebert, and I. N. Reid
2007. Activity and kinematics of ultracool dwarfs, including an amazing flare observation. *The Astronomical Journal*, 133(5):2258–2273. → pages ix, 60, 62

Schneider, J.
1959. Stimulated Emission of Radiation by Relativistic Electrons in a Magnetic Field. *Physical Review Letters*, 2(12):504–505. → page 30

Schott
1912. Electromagnetic Radiation and the Mechanical Reactions arising from it. *Astrophysical Journal*. → page 39

Segura, A., L. M. Walkowicz, V. Meadows, J. Kasting, and S. Hawley
2010. The Effect of a Strong Stellar Flare on the Atmospheric Chemistry of an Earth-like Planet Orbiting an M Dwarf. *Astrobiology*, 10:751–771. → pages 41, 59, 96, 101, 106, 108

Shajn, G. and O. Struve
1929. On the rotation of the stars. *Astrophysics and Space Science*, 89:222–239. → page 19

Siegler, N., L. M. Close, E. E. Mamajek, and M. Freed
2003. An Adaptive Optics Survey of M6.0–M7.5 Stars: Discovery of Three Very Low Mass Binary Systems Including Two Probable Hyades Members. *Astrophysical Journal*, 598(2):1265–1276. → pages ix, 60

Skumanich, A.
1972. Time Scales for Ca II Emission Decay, Rotational Braking, and Lithium Depletion. *Astrophysical Journal*, 171:565. → page 4

Sorahana, S., I. Yamamura, and H. Murakami
2013. On the Radii of Brown Dwarfs Measured with AKARI Near-infrared Spectroscopy. *Astrophysical Journal*, 767(1):77. → page 70

Southworth, G. C.
1982. 1945, *Microwave Radiation from the Sun (with Erratum)*, volume 10, P. 168. → page 22

- Spiegel, E. A. and J. P. Zahn
1992. The solar tachocline. *Astronomy and Astrophysics*, 265:106–114. → pages 11, 81
- Steenbeck, M. and F. Krause
1969. On the Dynamo Theory of Stellar and Planetary Magnetic Fields. I. AC Dynamos of Solar Type. *Astronomische Nachrichten*, 291:49–84. → page 13
- Stelzer, B., J. Alcalá, K. Biazzo, B. Ercolano, I. Crespo-Chacón, J. López-Santiago, R. Martínez-Arnáiz, J. H. M. M. Schmitt, E. Rigliaco, F. Leone, and G. Cupani
2012. The ultracool dwarf DENIS-P J104814.7-395606. Chromospheres and coronae at the low-mass end of the main-sequence. *Astronomy and Astrophysics*, 537:A94. → pages 83, 112
- Stelzer, B., A. Marino, G. Micela, J. López-Santiago, and C. Liefke
2013. The UV and X-ray activity of the M dwarfs within 10 pc of the Sun. *Astrophysics and Space Science*, 431(3):2063–2079. → page 5
- Stevenson, D. J.
2018. Commentary: The habitability mantra: Hunting the Snark. *Physics Today*, 71(11):10–12. → page 92
- Storini, M. and A. Damiani
2008. Effects of the January 2005 GLE/SEP events on minor atmospheric components. In *International Cosmic Ray Conference*, volume 1 of *International Cosmic Ray Conference*, Pp. 277–280. → page 96
- Sukhodolov, T., I. Usoskin, E. Rozanov, E. Asvestari, W. T. Ball, M. A. J. Curran, H. Fischer, G. Kovaltsov, F. Miyake, T. Peter, C. Plummer, W. Schmutz, M. Severi, and R. Traversi
2017. Atmospheric impacts of the strongest known solar particle storm of 775 AD. *Scientific Reports*, 7:45257. → page 96
- Takakura, T. and E. Scalise
1970. Gyro-Synchrotron Emission in a Magnetic Dipole Field for the Application to the Center-to-Limb Variation of Microwave Impulsive Bursts. *Solar Physics*, 11(3):434–455. → page 39
- Tarter, J.
2014. *Brown Is Not a Color: Introduction of the Term ‘Brown Dwarf’*, volume 401 of *Astrophysics and Space Science Library*, P. 19. → page 7

- Tasker, E., J. Tan, K. Heng, S. Kane, D. Spiegel, R. Brasser, A. Casey, S. Desch, C. Dorn, J. Hernlund, C. Houser, M. Laneuville, M. Lasbleis, A.-S. Libert, L. Noack, C. Unterborn, and J. Wicks
2017. The language of exoplanet ranking metrics needs to change. *Nature Astronomy*, 1:0042. → page 92
- Thejappa, G. and R. J. MacDowall
2015. Solar Type III Radio Bursts: Directivity Characteristics. In *Journal of Physics Conference Series*, volume 642 of *Journal of Physics Conference Series*, P. 012028. → page 30
- Tilley, M. A., A. Segura, V. S. Meadows, S. Hawley, and J. Davenport
2017. Modeling Repeated M-dwarf Flaring at an Earth-like Planet in the Habitable Zone: I. Atmospheric Effects for an Unmagnetized Planet. *arXiv e-prints*. → pages xix, 41, 59, 95, 96, 97, 101, 105, 106, 108
- Treumann, R. A.
2006. The electron-cyclotron maser for astrophysical application. *Astronomy and Astrophysics*, 13(4):229–315. → pages xiii, 31, 32, 34, 35
- Turnbull, M. C., T. Glassman, A. Roberge, W. Cash, C. Noecker, A. Lo, B. Mason, P. Oakley, and J. Bally
2012. The Search for Habitable Worlds. 1. The Viability of a Starshade Mission. *Publications of the ASP*, 124(915):418. → page 94
- Turnpenney, S., J. D. Nichols, G. A. Wynn, and M. R. Burleigh
2018. Exoplanet-induced Radio Emission from M Dwarfs. *Astrophysical Journal*, 854(1):72. → page 58
- Twiss, R. Q.
1958. Radiation Transfer and the Possibility of Negative Absorption in Radio Astronomy. *Australian Journal of Physics*, 11:564. → page 30
- Usoskin, I. G., B. Kromer, F. Ludlow, J. Beer, M. Friedrich, G. A. Kovaltsov, S. K. Solanki, and L. Wacker
2013. The AD775 cosmic event revisited: the Sun is to blame. *Astronomy and Astrophysics*, 552:L3. → page 96
- Van Grootel, V., C. S. Fernandes, M. Gillon, E. Jehin, J. Manfroid, R. Scudlaire, A. J. Burgasser, K. Barkaoui, Z. Benkhaldoun, A. Burdanov, L. Delrez, B.-O. Demory, J. de Wit, D. Queloz, and A. H. M. J. Triaud
2018. Stellar Parameters for Trappist-1. *Astrophysical Journal*, 853:30. → pages 74, 75

- Verkhoglyadova, O. P., G. Li, X. Ao, and G. P. Zank
 2012. Radial Dependence of Peak Proton and Iron Ion Fluxes in Solar Energetic Particle Events: Application of the PATH Code. *Astrophysical Journal*, 757(1):75. → page 98
- Vida, K., Z. Kóvári, A. Pál, K. Oláh, and L. Kriskovics
 2017. Frequent Flaring in the TRAPPIST-1 System Unsuitable for Life? *Astrophysical Journal*, 841:124. → pages 75, 76, 85, 106
- Švestka, Z. and P. Simon
 1969. Proton Flare Project, 1966. Summary of the August/September Particle Events in the McMath Region 8461. (Invited Review Paper). *Solar Physics*, 10(1):3–59. → page 103
- West, A. A., J. J. Bochanski, S. L. Hawley, K. L. Cruz, K. R. Covey, N. M. Silvestri, I. N. Reid, and J. Liebert
 2006. Using the Galactic Dynamics of M7 Dwarfs to Infer the Evolution of Their Magnetic Activity. *Astronomical Journal*, 132(6):2507–2512. → page 4
- Wheatley, P. J., T. Louden, V. Bourrier, D. Ehrenreich, and M. Gillon
 2017. Strong XUV irradiation of the Earth-sized exoplanets orbiting the ultracool dwarf TRAPPIST-1. *Astrophysics and Space Science*, 465:L74–L78. → pages xvii, 75, 76, 80, 82
- Whipple, F. L.
 1966. *Smithsonian Astrophysical Observatory Star Catalog*. → page 9
- White, R. L.
 1985. Synchrotron emission from chaotic stellar winds. *Astrophysical Journal*, 289:698–708. → page 38
- White, S. M. and M. R. Kundu
 1992. Solar Observations with a Millimeter Wavelength Array. *Solar Physics*, 141(2):347–369. → page 38
- White, S. M., M. R. Kundu, and P. D. Jackson
 1989. Simple non-thermal models for the quiescent radio emission of dMe flare stars. *Astronomy and Astrophysics*, 225:112–124. → page 83
- Wild, J. P. and E. R. Hill
 1971. Approximation of the general formulae for gyro and synchrotron radiation in a vacuum and isotropic plasma. *Australian Journal of Physics*, 24:43. → page 39

- Williams, P. K. G., E. Berger, J. Irwin, Z. K. Berta-Thompson, and D. Charbonneau
2015. Simultaneous multiwavelength observations of magnetic activity in ultracool dwarfs. iv. the active, young binary nltt 33370 ab (= 2mass j13142039+1320011). *The Astrophysical Journal*, 799(2):192. → pages xvii, 63, 64, 82
- Williams, P. K. G., S. L. Casewell, C. R. Stark, S. P. Littlefair, C. Helling, and E. Berger
2015. The First Millimeter Detection of a Non-Accreting Ultracool Dwarf. *Astrophysical Journal*, 815:64. → pages 21, 38, 58, 59, 77, 81, 97
- Williams, P. K. G., B. A. Cook, and E. Berger
2014. Trends in Ultracool Dwarf Magnetism. I. X-Ray Suppression and Radio Enhancement. *Astrophysical Journal*, 785(1):9. → pages xii, 18, 20, 40, 58, 71, 76, 81, 83, 112
- Wills, B. J., D. Wills, M. Breger, R. R. J. Antonucci, and R. Barvainis
1992. A Survey for High Optical Polarization in Quasars with Core-dominant Radio Structure: Is There a Beamed Optical Continuum? *Astrophysical Journal*, 398:454. → page 36
- Wu, C. S. and L. C. Lee
1979. A theory of the terrestrial kilometric radiation. *Astrophysical Journal*, 230:621–626. → page 34
- Yang, J., N. B. Cowan, and D. S. Abbot
2013. Stabilizing Cloud Feedback Dramatically Expands the Habitable Zone of Tidally Locked Planets. *Astrophysical Journal, Letters*, 771(2):L45. → page 6
- Zarka, P.
1998. Auroral radio emissions at the outer planets: Observations and theories. *Journal of Geophysics Research*, 103(E9):20159–20194. → pages xvi, 69
- Zarka, P.
2004. Fast radio imaging of Jupiter’s magnetosphere at low-frequencies with LOFAR. *Planetary Space Science*, 52(15):1455–1467. → page 35
- Zheleznyakov, V. V.
1970. *Radio emission of the sun and planets*. → page 70
- Zlotnik, E. Y., A. Klassen, K. L. Klein, H. Aurass, and G. Mann
1998. Third harmonic plasma emission in solar type II radio bursts. *Astronomy and Astrophysics*, 331:1087–1098. → page 30

- Zsom, A., S. Seager, J. de Wit, and V. Stamenković
2013. Toward the Minimum Inner Edge Distance of the Habitable Zone.
Astrophysical Journal, 778(2):109. → page 5
- Zucca, P., M. Núñez, and K. Klein
2017. Exploring the potential of microwave diagnostics in SEP forecasting:
The occurrence of SEP events. *Journal of Space Weather and Space Climate*,
7:A13. → page 102